

Citation for published version:

Luke Hindson, et al, 'A Radio Continuum Study of Dwarf Galaxies: 6 cm Imaging of LITTLE THINGS', *The Astrophysical Journal Supplement Series*, vol. 234 (69), February 2018.

DOI:

<https://doi.org/10.3847/1538-4365/aaa42c>

Document Version:

This is the Published Version.

Copyright and Reuse:

© 2018 The American Astronomical Society.

Original content from this work may be used under the terms of the [Creative Commons Attribution 3.0 licence](#). Any further distribution of this work must maintain attribution to the author(s) and the title of the work, journal citation and DOI.

Enquiries

If you believe this document infringes copyright, please contact Research & Scholarly Communications at rsc@herts.ac.uk



A Radio Continuum Study of Dwarf Galaxies: 6 cm Imaging of LITTLE THINGS

Luke Hindson¹ , Ged Kitchener¹ , Elias Brinks¹ , Volker Heesen^{2,6}, Jonathan Westcott¹, Deidre Hunter³ , Hong-Xin Zhang⁴,
Michael Rupen^{5,7}, and Urvashi Rau⁵

¹ Centre for Astrophysics Research, University of Hertfordshire, Hatfield, AL10 9AB, UK; l.hindson3@herts.ac.uk

² School of Physics and Astronomy, University of Southampton, Southampton, SO17 1BJ, UK

³ Lowell Observatory, 1400 West Mars Hill Road, Flagstaff, AZ 86001, USA

⁴ Institute of Astrophysics, Pontificia Universidad Católica de Chile, Av. Vicuña Mackenna 4860, 7820436 Macul, Santiago, Chile

⁵ National Radio Astronomy Observatory, 1003 Lopezville Road, Socorro, NM 87801, USA

Received 2017 February 12; revised 2017 December 22; accepted 2017 December 25; published 2018 February 1

Abstract

In this paper, we examine to what extent the radio continuum can be used as an extinction-free probe of star formation in dwarf galaxies. To that aim, we observe 40 nearby dwarf galaxies with the Very Large Array at 6 cm (4–8 GHz) in C-configuration. We obtained images with 3''–8'' resolution and noise levels of 3–15 $\mu\text{Jy beam}^{-1}$. We detected emission associated with 22 of the 40 dwarf galaxies, eight of which are new detections. The general picture is that of an interstellar medium largely devoid of radio continuum emission, interspersed by isolated pockets of emission associated with star formation. We find an average thermal fraction of $\sim 50\%$ – 70% and an average magnetic field strength of ~ 5 – $8 \mu\text{G}$, only slightly lower than that found in larger, spiral galaxies. At 100 pc scales, we find surprisingly high values for the average magnetic field strength of up to $50 \mu\text{G}$. We find that dwarf galaxies follow the theoretical predictions of the radio continuum–star formation rate relation within regions of significant radio continuum emission but that the nonthermal radio continuum is suppressed relative to the star formation rate when considering the entire optical disk. We examine the far-infrared–star formation rate relation for our sample and find that the far-infrared is suppressed compared to the expected star formation rate. We discuss explanations for these observed relations and the impact of our findings on the radio continuum–far-infrared relation. We conclude that radio continuum emission at centimeter wavelengths has the promise of being a largely extinction-free star formation rate indicator. We find that star formation rates of gas-rich, low-mass galaxies can be estimated with an uncertainty of ± 0.2 dex between the values of 2×10^{-4} and $0.1 M_{\odot} \text{yr}^{-1}$.

Key words: galaxies: dwarf – galaxies: magnetic fields – galaxies: star formation – radio continuum: galaxies – radio continuum: ISM

1. Introduction

The radio continuum–far-infrared (RC–FIR) relation of galaxies holds over four orders of magnitude in luminosity, irrespective of galaxy type (de Jong et al. 1985; Helou et al. 1985; Yun et al. 2001). It displays a mere 0.26 dex scatter (Yun et al. 2001) and has been observed to hold at least out to a redshift of 3 (Appleton et al. 2004). The radio continuum (RC; see Condon 1992 for a review) and the far-infrared (FIR) have long been attributed to the input of energy following a star formation (SF) event. At 6 cm, the RC is comprised of two main contributions: a thermal component (RC_{Th}) from thermal electrons in H II regions and a nonthermal component (RC_{Nth}) generated by cosmic-ray electrons (CRE) accelerated in supernova shocks. The RC_{Th} and RC_{Nth} emission both have an unambiguous link to recent SF, while the FIR originates from the modified blackbody radiation of interstellar dust that is heated by the interstellar radiation field (Li et al. 2010).

The classical scenario leading to the RC–FIR relation assumes that a galaxy behaves as a calorimeter (Völk 1989). This model assumes that galaxies are optically thick to dust-heating UV photons which are absorbed by dust within the galaxy that goes on to reradiate the energy gained in the FIR. It also requires that magnetic fields retain all CRE, which eventually produce synchrotron radiation. Since all the energy contained within CRE is radiated, the strength of the magnetic field is irrelevant, i.e., whether the energy contained in the CRE is radiated over 1 Myr in a relatively strong magnetic field or over 1 Gyr in a weaker magnetic field, the total energy emitted is the same. The calorimeter assumption implies that the mean free path of dust-heating photons is less than the galaxy disk scale height, and that the typical energy loss timescale of CRE is less than the diffusion timescale to traverse the scale height.

Clearly, the calorimeter model is not perfect. Dust-heating photons *are* observed to be coming from galaxies, and RC_{Nth} emission *is* observed in the halos of larger spiral galaxies (Heesen et al. 2009). Therefore, for galaxies to follow the RC–FIR relation, the escape of CRE from galactic magnetic fields must be in proportion to the escape of dust-heating photons from the disk (Helou & Bicay 1985). Some of the earliest evidence of this comes from Klein et al. (1991), who stated that the deficiency of RC_{Nth} “happens to be balanced” by a lack of dust in a study of Blue Compact Dwarfs (BCDs). This is known as the “conspiracy” between the emission at RC and FIR wavelengths (e.g., Bell 2003; Dale et al. 2009; Lacki et al. 2010). The first paper with a quantitative model of the

⁶ Current address: Hamburger Sternwarte, Gojenbergsweg 112, 21029 Hamburg, Germany.

⁷ Current address: National Research Council of Canada, Herzberg Astronomy and Astrophysics Programs, Dominion Radio Astrophysical Observatory, PO Box 248, Penticton, BC V2A 6J9, Canada.



RC–FIR correlation for noncalorimeter galaxies and the “conspiracy” between the processes involved was that by Niklas & Beck (1997), who predicted a slightly nonlinear correlation for the synchrotron emission. To complicate the picture further, heating of the diffuse cold dust by photons may not be sufficient to make the RC–FIR relation as tight as observed; Xu (1990) found that a significant fraction of the heating of diffuse cool dust could not be accounted for by UV radiation in their sample of 40 spiral galaxies. An alternative source to compensate for this insufficient UV heating could be heating by CRe (as, for example, in ultraluminous infrared galaxies; Papadopoulos 2010).

It is difficult to disentangle the many factors that lead to the RC–FIR relation. This is especially true in large spiral galaxies where within any kiloparsec-size area the CRe population stemming from recent SF can be contaminated by older CRe from neighboring areas. The interstellar medium (ISM) in spirals likewise is in a constant state of flux with differential rotation and spiral arms transporting material in and out of such a kiloparsec-size region. We argue therefore that dwarf galaxies create a more accessible route to understanding the relationship between the RC and FIR emission and the SF. The low mass of dwarf galaxies leads to SF, which simulations suggest is episodic (e.g., Stinson et al. 2007 liken the SF history of isolated dwarf galaxies to “breathing”). If this is the case, then within a set region, one is only ever receiving emission from one generation of CRe . However, observational evidence suggests that the duration of bursts of SF in dwarf galaxies may actually be quite long in some cases (0.5–1.3 Gyr; McQuinn et al. 2010), which may complicate this interpretation. Dwarf galaxies also contain proportionally less dust than spirals, as confirmed by several authors (e.g., Lisenfeld & Ferrara 1998; Bigiel et al. 2008), and should therefore be fainter in the FIR for a given level of radio emission. Understanding the origin of RC_{Nth} emission generated should also be more straightforward in dwarf galaxies. They lack differential rotation (Gallagher & Hunter 1984) and thus lack the associated dynamo action present in larger, grand-design spirals that leads to the amplification of the magnetic field and ordered fields of $\sim 5 \mu\text{G}$ between spiral arms (Beck 2009). Observations suggest that dwarf galaxies differ markedly from spirals in terms of their magnetic field strength (e.g., Chyży et al. 2011; Roychowdhury & Chengalur 2012). These features make dwarf galaxies ideal laboratories in which to study the RC–FIR relationship.

Historically, spatially resolved studies of the RC in dwarf galaxies have been limited by their intrinsically low surface brightness. To date, resolved observations of dwarf galaxies have been restricted to the few brightest: the near and bright IC 10 (Heesen et al. 2011), IC 1613 (Chyży et al. 2011), NGC 4214 (Kepley et al. 2011), NGC 1569 (Lisenfeld et al. 2004; Kepley et al. 2010; Westcott et al. 2017), and the Magellanic Clouds (e.g., Filipovic et al. 1995; Filipović et al. 1998; Leverenz & Filipović 2013). The NRAO⁸ Karl G. Jansky Very Large Array (VLA), after recently benefiting from a major upgrade, provided the prospect of routinely delivering quality, good signal-to-noise (S/N) observations of nearby dwarf galaxies. This opportunity is exploited here to revisit the

relationship among the RC, FIR, and SF rate (SFR) in the dwarf galaxy regime.

The study presented here is based on VLA C-band (4–8 GHz) images of the 40 dwarf galaxies corresponding to the LITTLE THINGS sample (Hunter et al. 2012), mainly focusing on the relation of RC emission with SFR indicators. The ultimate aim is to increase our understanding of the RC–SFR relation of low-mass, low-metallicity systems. With the development of the Square Kilometer Array (SKA; Dewdney et al. 2015), calibrating the RC–SFR relation in quiescent/low-SFR galaxies will become more important than ever. The benefit of the RC is that observations can be carried out with ground-based instruments rather than expensive (cryogenically cooled) IR satellites. Our calibration of the RC–SFR relation may provide a better understanding of how this indicator may work at higher redshift, in the domain that will be accessible to the SKA.

This paper is organized as follows: in Section 2, we describe the observations, calibration, and imaging of our sample. We present our results (images and integrated emission) in Section 3. We then discuss our results, including the RC–SFR, FIR–SFR, and RC–FIR relations in Sections 4.2–4.4, respectively. We summarize our results in Section 5.

2. Observations and Data Reduction

2.1. Observations

The LITTLE THINGS sample consists of 40 gas-rich dwarf galaxies within 11 Mpc (see Hunter et al. 2012 for sample details) and is listed in Table 1. The sample spans 4 dex in both SFR and gas mass, and a factor of 50 in metallicity.

Observations of the LITTLE THINGS sample were obtained (project ID: 12A-234) with the VLA at C-band (6 cm: 4–8 GHz) and in its C-configuration in nine observing runs between March and May of 2012. All observing runs included one of four NRAO primary calibrators to calibrate the flux scale and a calibrator within 10° of each dwarf galaxy to correct the complex gain on timescales of around 10 minutes. For the details of the various calibrators used, see Table 2. One of the primary goals of these observations is to resolve the faint low surface brightness emission associated with dwarf galaxies. The C-configuration provided the best compromise between resolution and surface brightness sensitivity. We note that IC 1613 is 0.7 Mpc away and so has a large angular size. We utilized archival observations taken in D-configuration (project ID: AH1006) to minimize the effect of missing large-scale emission for this galaxy. At the C-band, we expect a roughly equal mix of RC_{Th} and RC_{Nth} emission and sensitivity to spatial scales up to $\sim 4'$. Given that most galaxies have angular sizes smaller than this, we do not expect significant loss of large-scale flux.

2.2. Radio Continuum Calibration and Imaging

We calibrated the data using the Common Astronomy Software Applications (CASA⁹; McMullin et al. 2007) package following standard procedures that we present in the following subsections.

2.2.1. Flagging

Before calibration, we used the TFLAGDATA task to apply two automatic flagging algorithms: TFCROP (Rau & Pramesh 2003) and RFLAG (based on AIPS; Greisen 2011). The TFCROP

⁸ The National Radio Astronomy Observatory is a facility of the National Science Foundation operated under cooperative agreement by Associated Universities, Inc.

⁹ <http://casa.nrao.edu/>

Table 1
The Galaxy Sample

Galaxy	Other Names ^a	D (Mpc)	M_V (mag)	R_H^b (arcmin)	R_D^b (kpc)	$E(B - V)^c$	$\log_{10} \Sigma_{\text{SFR}}(\text{H}\alpha)$ ($M_{\odot}\text{yr}^{-1} \text{kpc}^{-2}$) ^d	$\log_{10} \Sigma_{\text{SFR}}(\text{FUV})$ ($M_{\odot}\text{yr}^{-1} \text{kpc}^{-2}$) ^d	$12 + \log_{10} \text{O}/\text{H}^e$
Im Galaxies									
CVnIdwA	UGCA 292	3.6	-12.4	0.87	0.57 ± 0.12	0.01	-2.58 ± 0.01	-2.48 ± 0.01	7.3 ± 0.06
DDO 43	PGC 21073, UGC 3860	7.8	-15.1	0.89	0.41 ± 0.03	0.05	-1.78 ± 0.01	-1.55 ± 0.01	8.3 ± 0.09
DDO 46	PGC 21585, UGC 3966	6.1	-14.7	...	1.14 ± 0.06	0.05	-2.89 ± 0.01	-2.46 ± 0.01	8.1 ± 0.1
DDO 47	PGC 21600, UGC 3974	5.2	-15.5	2.24	1.37 ± 0.06	0.02	-2.70 ± 0.01	-2.40 ± 0.01	7.8 ± 0.2
DDO 50	PGC 23324, UGC 4305, Holmberg II, VIIZw 223	3.4	-16.6	3.97	1.10 ± 0.05	0.02	-1.67 ± 0.01	-1.55 ± 0.01	7.7 ± 0.14
DDO 52	PGC 23769, UGC 4426	10.3	-15.4	1.08	1.30 ± 0.13	0.03	-3.20 ± 0.01	-2.43 ± 0.01	(7.7)
DDO 53	PGC 24050, UGC 4459, VIIZw 238	3.6	-13.8	1.37	0.72 ± 0.06	0.03	-2.42 ± 0.01	-2.41 ± 0.01	7.6 ± 0.11
DDO 63	PGC 27605, Holmberg I, UGC 5139, Mailyan 044	3.9	-14.8	2.17	0.68 ± 0.01	0.01	-2.32 ± 0.01	-1.95 ± 0.01	7.6 ± 0.11
DDO 69	PGC 28868, UGC 5364, Leo A	0.8	-11.7	2.40	0.19 ± 0.01	0.00	-2.83 ± 0.01	-2.22 ± 0.01	7.4 ± 0.10
DDO 70	PGC 28913, UGC 5373, Sextans B	1.3	-14.1	3.71	0.48 ± 0.01	0.01	-2.85 ± 0.01	-2.16 ± 0.01	7.5 ± 0.06
DDO 75	PGC 29653, UGCA 205, Sextans A	1.3	-13.9	3.09	0.22 ± 0.01	0.02	-1.28 ± 0.01	-1.07 ± 0.01	7.5 ± 0.06
DDO 87	PGC 32405, UGC 5918, VIIZw 347	7.7	-15.0	1.15	1.31 ± 0.12	0.00	-1.36 ± 0.01	-1.00 ± 0.01	7.8 ± 0.04
DDO 101	PGC 37449, UGC 6900	6.4	-15.0	1.05	0.94 ± 0.03	0.01	-2.85 ± 0.01	-2.81 ± 0.01	8.7 ± 0.03
DDO 126	PGC 40791, UGC 7559	4.9	-14.9	1.76	0.87 ± 0.03	0.00	-2.37 ± 0.01	-2.10 ± 0.01	(7.8)
DDO 133	PGC 41636, UGC 7698	3.5	-14.8	2.33	1.24 ± 0.09	0.00	-2.88 ± 0.01	-2.62 ± 0.01	8.2 ± 0.09
DDO 154	PGC 43869, UGC 8024, NGC 4789A	3.7	-14.2	1.55	0.59 ± 0.03	0.01	-2.50 ± 0.01	-1.93 ± 0.01	7.5 ± 0.09
DDO 155	PGC 44491, UGC 8091, GR 8, LSBC D646-07	2.2	-12.5	0.95	0.15 ± 0.01	0.01	-1.44 ± 0.01	...	7.7 ± 0.06
DDO 165	PGC 45372, UGC 8201, IIZw 499, Mailyan 82	4.6	-15.6	2.14	2.26 ± 0.08	0.01	-3.67 ± 0.01	...	7.6 ± 0.08
DDO 167	PGC 45939, UGC 8308	4.2	-13.0	0.75	0.33 ± 0.05	0.00	-2.36 ± 0.01	-1.83 ± 0.01	7.7 ± 0.2
DDO 168	PGC 46039, UGC 8320	4.3	-15.7	2.32	0.82 ± 0.01	0.00	-2.27 ± 0.01	-2.04 ± 0.01	8.3 ± 0.07
DDO 187	PGC 50961, UGC 9128	2.2	-12.7	1.06	0.18 ± 0.01	0.00	-2.52 ± 0.01	-1.98 ± 0.01	7.7 ± 0.09
DDO 210	PGC 65367, Aquarius Dwarf	0.9	-10.9	1.31	0.17 ± 0.01	0.03	...	-2.71 ± 0.06	(7.2)
DDO 216	PGC 71538, UGC 12613, Peg DIG, Pegasus Dwarf	1.1	-13.7	4.00	0.54 ± 0.01	0.02	-4.10 ± 0.07	-3.21 ± 0.01	7.9 ± 0.15
F564-V3	LSBC D564-08	8.7	-14.0	...	0.53 ± 0.03	0.02	...	-2.79 ± 0.02	(7.6)
IC 10	PGC 1305, UGC 192	0.7	-16.3	...	0.40 ± 0.01	0.75	-1.11 ± 0.01	...	8.2 ± 0.12
IC 1613	PGC 3844, UGC 668, DDO 8	0.7	-14.6	9.10	0.58 ± 0.02	0.00	-2.56 ± 0.01	-1.99 ± 0.01	7.6 ± 0.05
LGS 3	PGC 3792, Pisces dwarf	0.7	-9.7	0.96	0.23 ± 0.02	0.04	...	-3.88 ± 0.06	(7.0)
M81 dwA	PGC 23521	3.5	-11.7	...	0.26 ± 0.01	0.02	...	-2.26 ± 0.01	(7.3)
NGC 1569	PGC 15345, UGC 3056, Arp 210, VIIZw 16	3.4	-18.2	...	0.38 ± 0.02	0.51	0.19 ± 0.01	-0.01 ± 0.01	8.2 ± 0.05
NGC 2366	PGC 21102, UGC 3851, DDO 42	3.4	-16.8	4.72	1.36 ± 0.04	0.04	-1.67 ± 0.01	-1.66 ± 0.01	7.9 ± 0.01
NGC 3738	PGC 35856, UGC 6565, Arp 234	4.9	-17.1	2.40	0.78 ± 0.01	0.00	-1.66 ± 0.01	-1.53 ± 0.01	8.4 ± 0.01
NGC 4163	PGC 38881, NGC 4167, UGC 7199	2.9	-14.4	1.47	0.27 ± 0.03	0.00	-2.28 ± 0.13	-1.74 ± 0.01	7.9 ± 0.2
NGC 4214	PGC 39225, UGC 7278	3.0	-17.6	4.67	0.75 ± 0.01	0.00	-1.03 ± 0.01	-1.08 ± 0.01	8.2 ± 0.06
Sag DIG	PGC 63287, Lowal's Object	1.1	-12.5	...	0.23 ± 0.03	0.14	-2.97 ± 0.04	-2.11 ± 0.01	7.3 ± 0.1
UGC 8508	PGC 47495, I Zw 60	2.6	-13.6	1.28	0.27 ± 0.01	0.00	-2.03 ± 0.01	...	7.9 ± 0.2
WLM	PGC 143, UGCA 444, DDO 221, Wolf-Lundmark-Melott	1.0	-14.4	5.81	0.57 ± 0.03	0.02	-2.77 ± 0.01	-2.05 ± 0.01	7.8 ± 0.06
BCD Galaxies									
Haro 29	PGC 40665, UGCA 281, Mrk 209, I Zw 36	5.8	-14.6	0.84	0.29 ± 0.01	0.00	-0.77 ± 0.01	-1.07 ± 0.01	7.9 ± 0.07

Table 1
(Continued)

Galaxy	Other Names ^a	D (Mpc)	M_V (mag)	R_H^b (arcmin)	R_D^b (kpc)	$E(B - V)^c$	$\log_{10} \Sigma_{\text{SFR}}(\text{H}\alpha)$ ($M_{\odot}\text{yr}^{-1} \text{kpc}^{-2}$) ^d	$\log_{10} \Sigma_{\text{SFR}}(\text{FUV})$ ($M_{\odot}\text{yr}^{-1} \text{kpc}^{-2}$) ^d	$12 + \log_{10} \text{O}/\text{H}^e$
Haro 36	PGC 43124, UGC 7950	9.3	-15.9	...	0.69 ± 0.01	0.00	-1.86 ± 0.01	-1.55 ± 0.01	8.4 ± 0.08
Mrk 178	PGC 35684, UGC 6541	3.9	-14.1	1.01	0.33 ± 0.01	0.00	-1.60 ± 0.01	-1.66 ± 0.01	7.7 ± 0.02
VII Zw 403	PGC 35286, UGC 6456	4.4	-14.3	1.11	0.52 ± 0.02	0.02	-1.71 ± 0.01	-1.67 ± 0.01	7.7 ± 0.01

Notes. See Hunter et al. 2012 for references to galaxy distances and oxygen abundances.

^a Selected alternate identifications obtained from NED.

^b R_H is the Holmberg radius, the radius of the galaxy at a B -band isophote, corrected for reddening of 26.7 mag arcsec⁻². R_D is the disk scale length measured from V -band images (table from Hunter & Elmegreen 2006).

^c Foreground reddening from Burstein & Heiles (1984).

^d $\Sigma_{\text{SFR}}(\text{H}\alpha)$ is the star formation rate density (SFRD) measured from $\text{H}\alpha$, calculated over the area πR_D^2 , where R_D is the disk scale length (Hunter & Elmegreen 2004). $\Sigma_{\text{SFR}}(\text{FUV})$ is the SFRD determined from *GALEX* FUV fluxes.

^e Values in parentheses were determined from the empirical relationship between oxygen abundance and M_B and are particularly uncertain.

Table 2
C-band Observations and Imaging Properties of LITTLE THINGS

Galaxy Name (1)	Observation			Imaging					
	Date (2)	Flux Cal. Name (3)	Gain Cal. Name (4)	Phase Center		Scale pc arcsec ⁻¹ (7)	Res. arcsec (8)	Noise μ Jy beam ⁻¹ (9)	Notes (10)
				R.A. (5)	Decl. (6)				
CVn I dwA	2012 Mar 17	3C 286	J1310+3220	12 38 40.2	+32 45 40	6.3	3.0 × 3.0	4.3	N
DDO 43	2012 Mar 22	3C 286	J0818+4222	07 28 17.8	+40 46 13	8.5	2.5 × 2.3	6.9	R, S
DDO 46	2012 Mar 22	3C 286	J0818+4222	07 41 26.6	+40 06 39	8.5	3.0 × 2.8	5.1	N
DDO 47	2012 Mar 20	3C 286	J0738+1742	07 41 55.3	+16 48 08	8.0	3.2 × 3.0	5.0	N
DDO 50	2012 Mar 17	3C 147	J0841+7053	08 19 08.7	+70 43 25	5.2	4.4 × 3.5	5.5	N, S
DDO 52	2012 Mar 22	3C 286	J0818+4222	08 28 28.5	+41 51 21	9.3	2.2 × 2.0	8.3	R, S
DDO 53	2012 Mar 16	3C 147	J0841+7053	08 34 08.0	+66 10 37	5.6	4.9 × 4.0	5.4	N
DDO 63	2012 Mar 25	3C 286	J0841+7053	09 40 30.4	+71 11 02	5.9	6.1 × 3.4	4.6	N
DDO 69	2012 Mar 20	3C 286	J0956+2515	09 59 25.0	+30 44 42	1.2	4.1 × 3.6	4.0	N
DDO 70	2012 Mar 20	3C 286	J0925+0019	10 00 00.9	+05 19 50	2.0	4.5 × 3.4	5.8	N
DDO 75	2012 Mar 20	3C 286	J1024-0052	10 10 59.2	-04 41 56	2.0	3.3 × 2.4	9.7	N, S
DDO 87	2012 Mar 25	3C 286	J1048+7143	10 49 34.7	+65 31 46	10.3	3.8 × 2.2	6.2	R
DDO 101	2012 Mar 17	3C 286	J1221+2813	11 55 39.4	+31 31 08	13.9	3.1 × 3.0	15.1	R, S, P
DDO 126	2012 Apr 05	3C 286	J1215+3448	12 27 06.5	+37 08 23	7.6	4.6 × 4.0	5.4	N, S
DDO 133	2012 Mar 17	3C 286	J1310+3220	12 32 55.4	+31 32 14	9.4	3.8 × 3.7	4.4	N, S
DDO 154	2012 Mar 17	3C 286	J1310+3220	12 54 06.2	+27 09 02	6.6	2.2 × 2.2	7.3	R,
DDO 155	2012 Mar 17	3C 286	J1309+1154	12 58 39.8	+14 13 10	3.4	3.8 × 3.5	4.7	N
DDO 165	2012 Mar 25	3C 286	J1313+6735	13 06 25.3	+67 42 25	7.4	3.7 × 2.8	4.5	R
DDO 167	2012 Apr 20	3C 286	J1327+4326	13 13 22.9	+46 19 11	6.5	3.3 × 3.0	5.1	N
DDO 168	2012 Apr 20	3C 286	J1327+4326	13 14 27.2	+45 55 46	5.4	3.9 × 3.5	4.4	N
DDO 187	2012 Mar 17	3C 286	J1407+2827	14 15 56.7	+23 03 19	3.9	2.7 × 2.5	6.9	R, S
DDO 210	2012 May 19	3C 48	J2047-1639	20 46 52.0	-12 50 51	1.4	3.1 × 1.7	4.6	R
DDO 216	2012 Mar 31	3C 48	J2253+1608	23 28 35.0	+14 44 30	1.4	3.1 × 2.9	5.1	R
F564-V03	2012 Mar 20	3C 286	J0854+2006	09 02 53.9	+20 04 29	9.6	3.3 × 3.0	5.4	N
Haro 29	2012 Apr 20	3C 286	1219+484	12 26 16.7	+48 29 38	8.3	3.9 × 3.6	5.1	N
Haro 36	2012 Apr 20	3C 286	1219+484	12 46 56.3	+51 36 48	13.9	3.9 × 3.6	5.2	N
IC 1613	2010 Aug 19	3C 48	J0108+0135	01 04 49.2	+02 07 48	1.1	9.3 × 7.8	5.1	R
IC 10	2012 Apr 28	3C 84	J0102+5824	00 20 17.3	+59 18 14	1.5	2.6 × 2.3	7.8	R
LGS 3	2012 Mar 31	3C 48	J0112+2244	01 03 55.2	+21 52 39	0.9	3.0 × 2.8	5.5	R
M81 dwA	2012 Mar 17	3C 147	J0841+7053	08 23 57.2	+71 01 51	5.6	2.7 × 1.9	10.8	R, S, P
Mrk 178	2012 Apr 20	3C 286	1219+484	11 33 29.0	+49 14 24	6.0	4.4 × 4.0	9.3	N
NGC 1569	2012 Mar 16	3C 147	J0449+6332	04 30 49.8	+64 50 51	3.9	2.7 × 2.3	6.8	R
NGC 2366	2012 Mar 16	3C 147	J0841+7053	07 28 48.8	+69 12 22	4.9	4.2 × 3.4	5.1	N
NGC 3738	2012 Apr 20	3C 286	J1146+5356	11 35 49.0	+54 31 23	7.6	2.5 × 2.5	7.6	N, S
NGC 4163	2012 Apr 05	3C 286	J1215+3448	12 12 09.2	+36 10 13	4.3	3.3 × 2.9	4.5	N
NGC 4214	2012 Apr 05	3C 286	J1215+3448	12 15 39.2	+36 19 38	4.5	4.5 × 4.0	6.3	N, S
Sag DIG	2012 May 19	3C 48	J1911-2006	19 30 00.6	-17 40 56	1.7	3.5 × 1.4	8.2	R
UGC 8508	2012 Apr 20	3C 286	J1349+5341	13 30 44.9	+54 54 29	4.0	2.6 × 2.5	6.0	N
VII Zw 403	2012 Mar 25	3C 286	J1153+8058	11 27 58.2	+78 59 39	6.8	5.8 × 3.7	5.8	N
WLM	2012 May 19	3C 48	J2348-1631	00 01 59.2	-15 27 41	1.5	5.0 × 1.5	5.3	R

Note. (Column 1) Name of dwarf galaxy observed; (Column 2) Date of observation; (Column 3) Name of primary calibrator; (Column 4) Name of secondary calibrator; (Columns 5 and 6) J2000 equatorial coordinate of observation (dwarf galaxy) phase center; (Column 7) Physical scale at distance of galaxy; (Column 8) Resolution of image. Note that some images were made using ROBUST = 0.0 and others using ROBUST = +2.0, where CASA robust values range between -2.0 (uniform weighting) and +2.0 (natural weighting); (Column 9) rms noise; (Column 10) Comments regarding deviations from the typical imaging process: *R* signifies that the CLEAN algorithm was performed using ROBUST = 0.0 weighting, whereas *N* signifies an approach closer to natural weighting; *S* means that the generated image benefited from self-calibration; *P* refers to those images that were strongly affected by a bright, nearby background source of ~ 0.1 Jy, which was located such that it entered the sidelobes of the primary beam. Because of the Alt-Az mounting of the VLA antennas, the primary beam rotates on the sky, making the detected signal time varying; self-calibration failed as a result. To minimize the effect of the offending source, only about a quarter of the bandwidth was used, using those spectral windows in which the first null of the primary beam coincides as closely as possible to the offending source.

algorithm identifies outliers by splitting each baseline into “chunks” along the frequency domain (each channel) and time domain (every 50 s). The amplitude of all visibilities within a given chunk was averaged, and then chunks with an amplitude greater than $4\sigma_{\text{pre}}$ from the mean were flagged. Here, σ_{pre} refers to the pre-calibration dispersion of amplitudes around the mean. We opted for a conservative threshold value as, at this point, we were only concerned with removing extremely

high-amplitude data such that subsequent steps in the calibration would not be affected. The RFLAG algorithm detects outliers by using a sliding window in the time and then spectral window domain to determine local statistics and identify data that exceed $4\sigma_{\text{pre}}$. The algorithm first calculates the local rms within each sliding window. It then calculates the median rms across the time windows, deviations of the local rms from this median, and the median deviation. Data are flagged if the local

rms is larger than $4 \times (\text{medianRMS} + \text{medianDev})$. For a more in-depth description of these algorithms, see Rau & Pramesh (2003) and Greisen (2011). Bad baselines, scans, and channels, as well as wide-band radio frequency interference (RFI) were generally caught by the algorithms, although the measurement sets were manually checked to identify any discrepant visibilities that were missed. This approach typically resulted in the removal of 15%–20% of the observed visibilities.

2.2.2. Calibration

The flux scale in our images was set using one of the recommended VLA primary flux calibrators given in column 3 of Table 2 using the task SETJY. This flux calibrator was also bright enough to be used to correct for the bandpass shape using the task BANDPASS. Calibration of the time-dependent complex gain was achieved by regular observations of a nearby gain calibrator (Table 2, column 4) using GAINCAL.

Once calibration was completed, each measurement set was inspected a final time for low-level RFI. First, a manual check was performed to flag baselines, scans, or channels that exhibited deviant amplitudes or phases. In addition to this, a second round of automated flagging was performed (this time designed to catch outliers greater than $3.5\sigma_{\text{post}}$ from the mean). Here, σ_{post} refers to the post-calibration dispersion of amplitudes around the mean. This flagging on the calibrated data often reduced the rms noise in subsequent imaging by a further $\sim 10\%$ (compared to when this second round of flagging was omitted).

2.2.3. Imaging

We generated images of our targets using the CASA CLEAN task, using the Multi-Scale, Multi-Frequency Synthesis (MS-MFS) algorithm developed by Rau & Cornwell (2011). Due to the various angular scales of emission observed in the galaxies, the cleaning scales chosen were unique to each observation to give the optimum CLEAN map. At least two scales of 1 and 3 times the synthesized beam width were used. In a few cases, larger angular scales were added to deal with large-scale emission in the brighter, more extended galaxies such as DDO 50 and NGC 1569.

Due to the faint nature of the dwarfs, observations were generally Fourier-transformed using natural weighting (ROBUST = +2.0). This ensured that we optimized our images for S/N. Some observations were mapped using Brigg’s robust imaging method (ROBUST = 0.0) because either (1) the galaxy was sufficiently bright that a high enough S/N was reached using ROBUST = 0.0 weighting, or (2) the natural weighting CLEAN left significant image artifacts throughout the image due to the rather sparse sampling of the (u, v) plane. Using Brigg’s ROBUST = 0.0 method ensures that the image is not dominated by visibilities representing the more numerous short baselines. This method increases the resolution, results in a synthesized beam that more closely resembles a Gaussian shape, and improves the image quality but at the expense of a slight ($\sim 20\%$) increase in the rms noise. Typical rms noise values in these cleaned images fell between 4 and $8 \mu\text{Jy beam}^{-1}$, in close agreement with the expected values. Table 2 states whether the image of the galaxy was generated using ROBUST = 0.0 weighting (*R*) or an approach closer to natural weighting (*N*).

Self-calibration (phase only) was performed on 11 of our 40 observations to improve the dynamic range across the image;

these are marked in Table 2 (S symbol in column 10). In only one case (NGC 4214) did the emission originating from the galaxy itself produce strong enough artifacts to warrant self-calibration; in all other cases, the offending source was an unresolved background object.

Observations of DDO 101 and M81 DWA (marked in Table 2) harbored the strongest background sources in our survey. These sources have a flux density of $>0.1 \text{ Jy}$ and are located approximately $9'$ and $6'$ from the observation’s phase center, respectively. Self-calibration was not successful in sufficiently improving the dynamic range for these images. This is due to a combination of both offending sources residing near the edge of the primary beam combined with the VLA antennas operating on an Alt-Az mount. This causes the offending sources to have a time-varying signal due to the source passing through the sidelobes of the primary beam. The result is that the MS-MFS CLEAN algorithm cannot successfully remove the sidelobes of the confusing source. Since these sources are not of interest to our project—they lie beyond the FWHM of the primary beam anyway—we decided to select solely the spectral windows least affected by the offending background source, i.e., by choosing two or three spectral windows for which the first null of the primary beam fell close to the offending source. In doing this, the rms noise was approximately doubled to $15 \mu\text{Jy beam}^{-1}$ while the sidelobes of the confusing source were considerably suppressed. We note that in an earlier study, Stil & Israel (2002) do not list a flux density for DDO 101 for the same technical reason.

We maintained as much consistency as possible by using the same calibration and imaging pipeline for all observations. Our images prior to primary beam correction had a flat noise background lacking in significant structure. Very few images had artifacts from nearby strong ($>0.5 \text{ mJy}$) sources. Those that did had the offending regions masked manually. Our residual maps comprise a Gaussian intensity distribution consistent with pure noise, having an average of 0 and variance of σ , suggesting that the MS-MFS algorithm successfully modeled all genuine emission present in the (u, v) data. Only NGC 1569 and NGC 4214 showed any indication of sitting in a negative bowl, suggesting that they suffer from missing flux on the largest scales (see Section 3.2 for further discussion). The observations and imaging properties of all LITTLE THINGS targets are summarized in Table 2. Notes on the data reduction of individual galaxies can be found in Appendix A.

2.3. Ancillary Data

The LITTLE THINGS project has acquired a large collection of multiwavelength and spatially resolved data on each of the 40 dwarf galaxies (see Hunter et al. 2012; Zhang et al. 2012 for details). We make use of the following ancillary data in this study:

1. $\text{H}\alpha$ line emission: the FWHM of the filter used for the $\text{H}\alpha$ observations was 30 \AA , centered on 6562.8 \AA (Hunter & Elmegreen 2004), while the FWHM of the point-spread function (PSF) was $\sim 2''$. The maps were continuum subtracted and the fluxes corrected for [N II] contribution. Hunter et al. (2012) used Burstein & Heiles (1982) values to correct the $\text{H}\alpha$ and FUV maps for foreground reddening. Internal extinction in dwarf galaxies can generally be ignored because they have low metallicity and consequently a low dust-to-gas ratio with respect to spirals (Ficut-Vicas 2016). However, internal extinction

may be important in some of the more actively star-forming dwarfs. We discuss this further in Section 4.1.2.

2. Far-ultraviolet broadband emission: the FUV data were taken with *GALEX* in the 1350–1750 Å band (effective wavelength of 1516 Å) with a resolution of 4'' at the FWHM. The data were calibrated with the GR4/5 pipeline except for DDO 165 and NGC 4214, which were processed with the GR6 pipeline (Zhang et al. 2012). The resulting images were sky subtracted and geometrically transformed to match the optical *V*-band orientation. UGC 8508 was not observed due to bright foreground stars, and IC 10 was not observed due to its low Galactic latitude, placing it in a region of high extinction. For surface brightness measurements, and hence for extended emission, the estimated uncertainty for the *GALEX* FUV maps is 0.15 mag (Gil de Paz et al. 2007).
3. Infrared (IR) broadband emission: the IR data were taken with the *Spitzer Space Telescope* using the Multiband Imaging Photometer for *Spitzer* (MIPS). The two bands used were mid-infrared (MIR), with an effective wavelength of 24 μm with a resolution of 6'' at FWHM, and FIR, with an effective wavelength of 70 μm and a resolution of 17''.5 at FWHM. The *Spitzer* 24 and 70 μm maps were taken from either the Local Volume Legacy (LVL) survey (see Dale et al. 2009, for details) or the *Spitzer* Infrared Nearby Galaxies Survey (SINGS). A pixel-dependent background subtraction was performed, and images were convolved with a custom kernel to make a near-Gaussian PSF. For the *Spitzer* 24 μm maps, the photometric uncertainty is 2% for both unresolved sources and extended emission (Engelbracht et al. 2007).

3. Results

We present an example of our multiwavelength data set in Figure 1, which shows our data for DDO 50. This includes the results of our RC observations and contours overlaid onto the H α , FUV, and 24 μm images. Multiwavelength images for our entire sample can be found in Appendix B.

3.1. Identifying Emission Unrelated to the Target Object

Contamination by background sources in the RC is an issue since their emission is often brighter than, or similar to, the emission originating from the dwarf galaxy (Padovani 2011). Low-resolution observations reported in the literature are predominantly from single-dish observations and will have suffered from contamination to varying degrees. Our resolved maps make it possible to remove the effects of contamination by identifying emission unrelated to our galaxies.

We inspected each of our RC images and classified features in a manner similar to Chomiuk & Wilcots (2009). Flux was attributed as originating from one of the following:

1. the dwarf galaxy (exactly coincident with an SF tracer), or
2. a background galaxy, or
3. ambiguous emission of unknown origin (i.e., unable to discern between (a) background origin or (b) nonthermal emission from unresolved supernova remnants (SNRs) or diffuse nonthermal emission).

We applied a two-step process to classify the RC emission in our images into these three categories. First, we cross-matched

our RC sources with the literature. Following this, we applied a procedure designed to isolate RC emission features from background galaxies based on their proximity to H α emission. We describe these two steps in more detail below.

3.1.1. Cross-matching with Line-of-sight Optical Counterparts

We manually cross-matched unresolved sources of RC emission with the NASA/IPAC Extragalactic Database¹⁰ (NED). If an archived galaxy was found within 2'' (approximately half the FWHM of the synthesized beam at the native resolution) of the unresolved RC source, we characterized that source as a background galaxy.

3.1.2. Isolating Obvious Background Galaxies

RC emission coming from the same line of sight as the H α emission from H II regions was assumed to originate from the dwarf galaxy. All galaxies in our sample have heliocentric velocities and rotational speeds (Hunter et al. 2012) that ensure all H α emission falls within the FWHM of the filter used, which is 30 Å wide and centered on 6562.8 Å (Hunter & Elmegreen 2004). Unresolved background galaxies and SNRs look similar and share broadly similar values for their nonthermal spectral index, with values of -0.85 ± 0.13 (Niklas et al. 1996) and -0.5 ± 0.2 (Green 2014) for background galaxies and SNRs, respectively. SNRs from core-collapse supernovae are expected to be associated with SF regions in our dwarf galaxies. This is because the stellar velocity dispersion in dwarf galaxies is low (Walker et al. 2007), which implies that over the lifetime of an SNR, it will not have strayed very far from its host massive star cluster. Studies of dwarf galaxies have measured velocity dispersions of $\lesssim 10$ km s⁻¹ (Mateo 1998; Martin et al. 2007; Walker et al. 2007), but the stellar velocity dispersion would still be lower for the subpopulation of high-mass stars (i.e., the core-collapse supernova progenitors) since these would generally sink to the bottom of the parent cluster's gravitational potential. Based on the above, we assume a stellar velocity dispersion of 5 km s⁻¹ for the stars that eventually lead to the injection of CR e (and the associated RC_{Nth} emission). Given that an SN progenitor may live up to 55 Myr and assuming a typical distance of 5 Mpc, an SNR can travel a projected distance of <250 pc or $<10''$ (for a face-on galaxy). Any significant RC source, unresolved or extended, that had little to no H α emission within this projected radius was marked as a background source and was removed by placing a mask over the source. For a Gaussian-like synthesized beam, 99% of the power of an unresolved source is contained within $3 \times \text{FWHM}_{\text{native}}$, and so this was the diameter of the mask placed over the background source. Even for a strong background source (e.g., 1 mJy), this removal technique leaves at most 10 μJy unmasked in the image while not masking out too much of the dwarf galaxy.

3.1.3. Ambiguous Sources

After cross-matching with NED and isolating ambiguous sources by comparing to H α , there remained sources that we could not attribute as coming from a background galaxy, but at the same time were not close enough to an SF site to be confidently classified as originating from the target galaxy; we

¹⁰ <http://ned.ipac.caltech.edu/forms/nearposn.html>

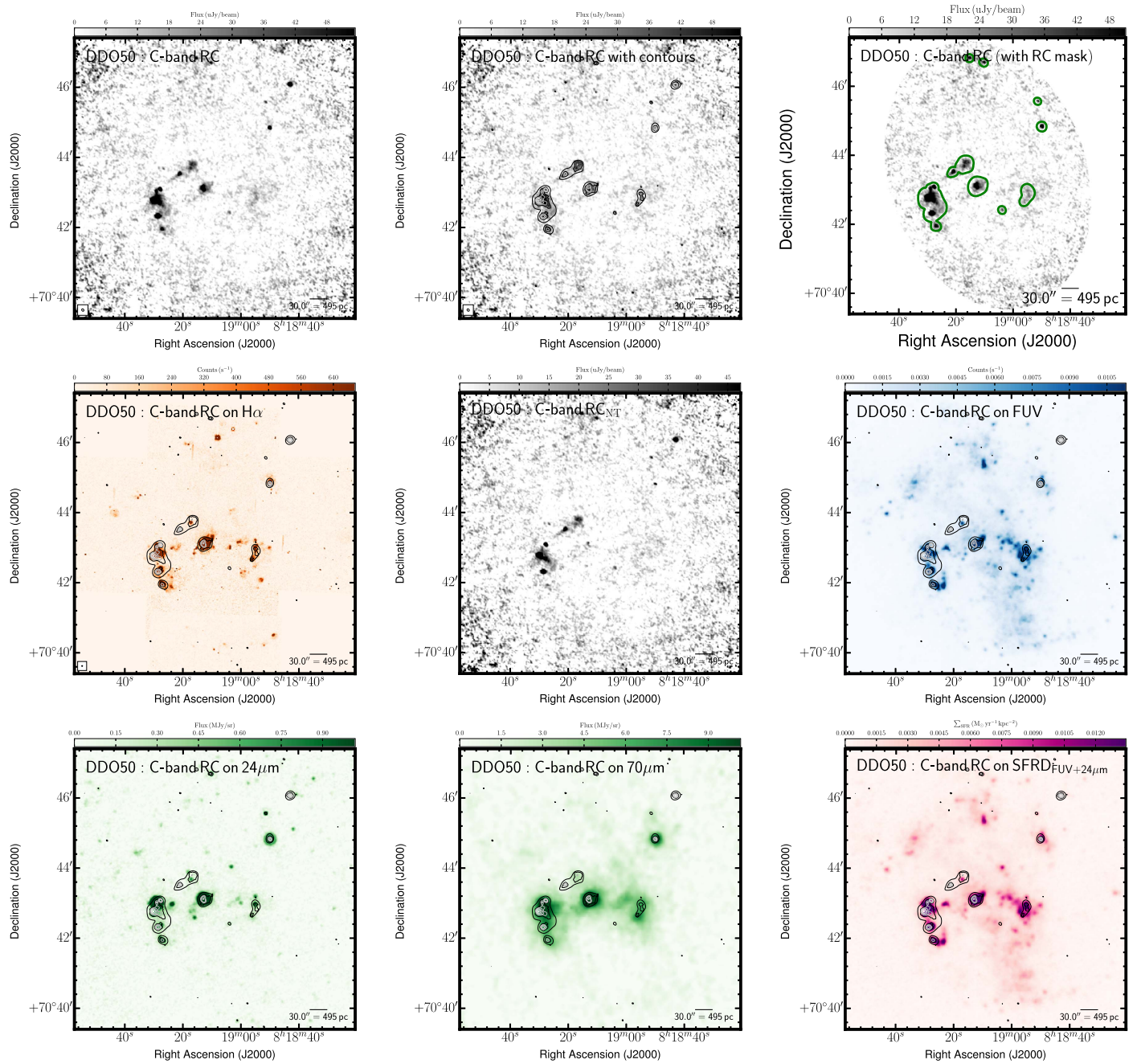


Figure 1. Multiwavelength coverage of DDO 50 displaying an $8'0 \times 8'0$ area. We show the total RC flux density at the native resolution (top left) and again with contours (top center). The lowest contour highlights low surface brightness emission at a S/N level of 3 in the image smoothed to $10''$. The remaining contours are at S/N levels of 3, 6, 9, and then multiples of twice the previous contour level from our native resolution images. These contours are also superposed on ancillary LITTLE THINGS images where possible: $H\alpha$ (middle left), RC_{Nth} (middle center), *GALEX* FUV (middle right), *Spitzer* $24\ \mu\text{m}$ (bottom left), *Spitzer* $70\ \mu\text{m}$ (bottom center), and FUV+ $24\ \mu\text{m}$ inferred SFRD (bottom right). We also show the RC that is isolated by the RC-based and disk masking technique (top right). In this panel, the green contours outline the RC mask and includes background and ambiguous sources. The elliptical outline corresponds to the area henceforth referred to as the disk mask.

refer to these sources of RC emission as ambiguous. To illustrate our definition of ambiguous RC emission, we present four of our observations that contained such a source in Figure 2. A strong unresolved source can be seen in DDO 46 and DDO 63, while DDO 69 and IC 1613 demonstrate galaxies with significantly extended sources.

Most of our observations contained at least one ambiguous source; none of these had a nonthermal luminosity that exceeded a reference threshold—that of a known bright SNR ($1 \times 10^{19}\ \text{W Hz}^{-1}$ or $3.3\ \text{mJy}$ at 5 Mpc at 6 GHz). This

reference luminosity was based on observations of SNR N4449–12, which resides in the dwarf galaxy NGC 4449 at a distance of 4.2 Mpc. In 2002, this SNR had a luminosity of $S_{6\text{cm}} = 4.84\ \text{mJy}$ with a spectral index of $\alpha = -0.7$ between 20 cm and 6 cm (Chomiuk & Wilcots 2009). For comparison, this is 10 times the luminosity of Cassiopeia A. Since the luminosity terminally declines for the majority of the SNR’s lifetime, we treat the observed luminosity of SNR N4449–12 in 2002 as an approximate empirical upper limit to the luminosity of an SNR. We justify our use of SNR N4449–12

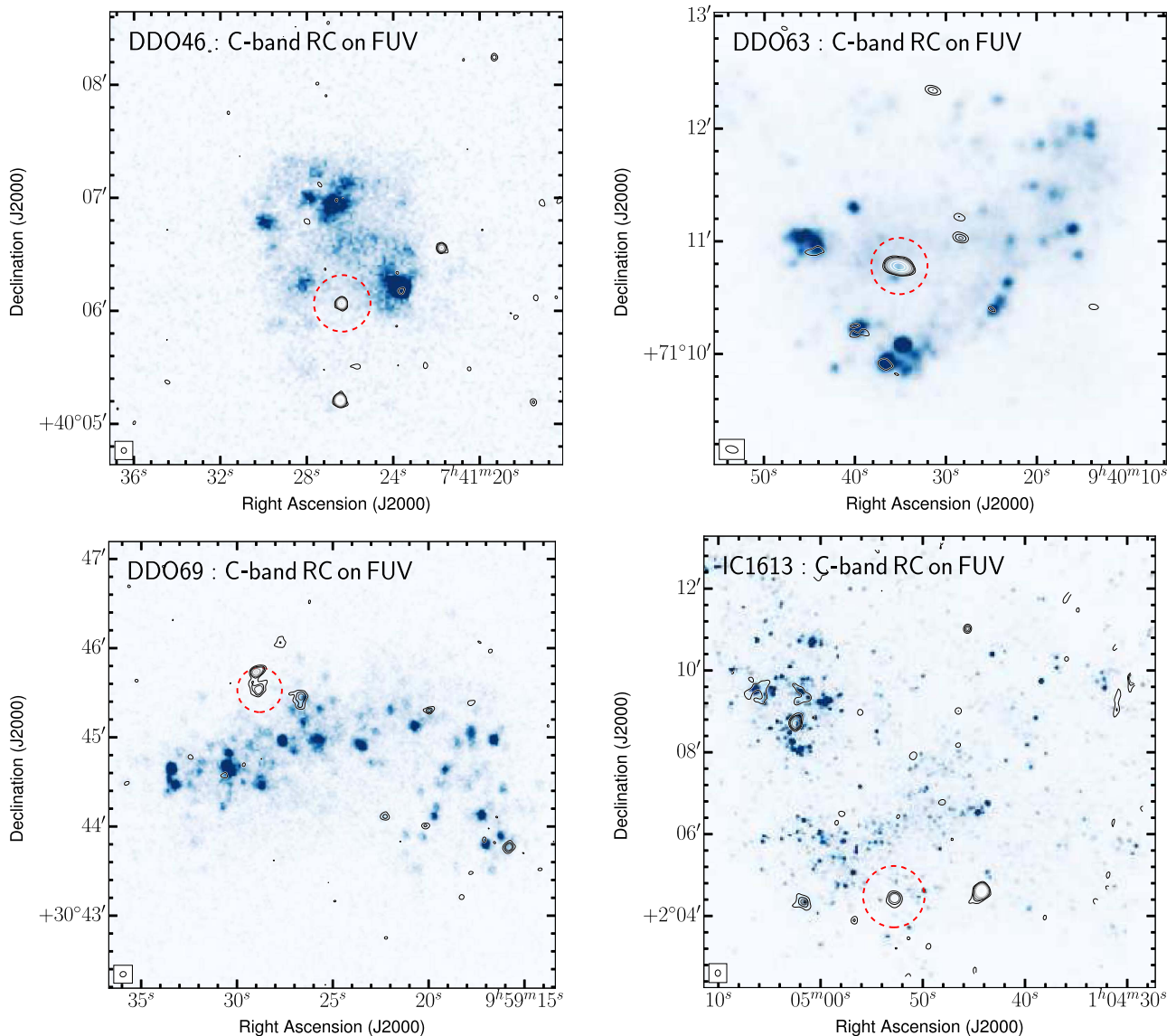


Figure 2. Examples of our definition of ambiguous emission (red dashed circles). We show DDO 46 and DDO 63, each of which contains an unresolved source of 1 mJy (top left) and 1.4 mJy (top right), respectively. We also show DDO 69 and IC 1613, both of which contain an extended source (bottom panels). The RC emission could not be attributed as definitely coming from a background galaxy, but at the same time was not close enough to an SF site to be confidently classified as originating from the target galaxy either; accordingly, these sources were designated ambiguous.

as it was the most luminous from a sample of 43 SNRs from four irregular galaxies (35 of which are in galaxies that overlap with our sample, namely: NGC 1569, NGC 2366, and NGC 4214).

Using the method above, we are able to classify all of the observed RC emission in our images. As an example, we show DDO 133 in Figure 3 along with the classification attributed to each source of RC emission.

3.2. Missing Large-scale Structures

Owing to the way that interferometers function, large angular structures in the sky can be completely missed if their corresponding visibilities are not recorded by the interferometer. The largest angular scale (θ_{LAS}) that the VLA is sensitive to in C-configuration (shortest baseline of 35 m) at 6 cm is ~ 4 arcminutes. This assumes an observation of 12 hr that is uniformly weighted and untapered. Observations of a shorter

duration will have a slightly lower θ_{LAS} value, and for weighting schemes closer to natural weighting, the θ_{LAS} will be larger. In our observations, angular scales of ~ 4 arcminutes and above may not be adequately sampled, leading to a lower than expected flux density; there are only seven galaxies with an angular size greater than $4'$ (see column 4 of Table 3). Under the assumption that RC emission coincides with optical emission, it is only these galaxies that are vulnerable to having large angular structures absent in the (u, v) data. Even so, the SF in dwarf galaxies is intermittent on scales of one to a few Gyr, whereas CRe age over much shorter timescales of tens of Myr; therefore, in the majority of our sample, no significant emission is expected from, for example, a CRe halo. We note that NGC 1569 was found to have an extended radio halo extending beyond the optical emission when observed between 0.6 and 1.4 GHz (Israel & de Bruyn 1988). This is attributed to the post-starburst nature of the galaxy, which is not reflected in

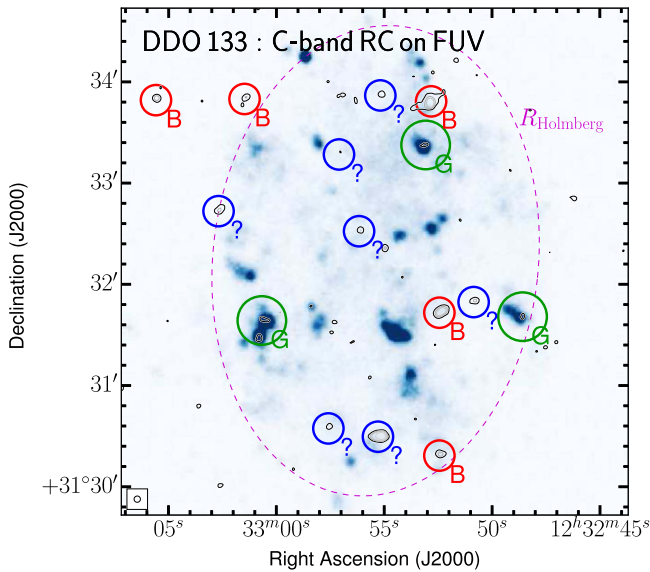


Figure 3. *GALEX* FUV emission of DDO 133 overlaid with our RC contours. Following the procedure outlined in the text we attribute RC emission as being from either the galaxy itself (G, green), a background galaxy (B, red), or an unknown or ambiguous source (? , blue). We also overlay the optical disk size (defined by the Holmberg radius; purple dashed ellipse).

the majority of targets in our sample. We do not see any evidence of such a halo in our 6 GHz image. This may be due to spatial filtering or spectral aging, which has shifted the halo emission below our detection threshold.

3.3. Disk-integrated Quantities

With background and ambiguous sources removed (see Section 3.1), emission from our RC and ancillary images was integrated within each of the dwarf galaxy’s optical disks (hereafter the disk mask; see Table 3 for the disk parameters). We also extract the integrated properties including the ambiguous sources; these can be found in Appendix C in Table 7. The semimajor axis of the disk was based on optical isophotes: using either the Holmberg radius (defined as the isophote where the *B*-band surface brightness drops to a magnitude of 26.66; Hunter & Elmegreen 2006) or three times the *V*-band disk scale length (Hunter & Elmegreen 2006) if the *B*-band radius was not defined. All emission outside this radius was masked.

3.4. Isolating Target RC Emission

The majority of our dwarf galaxy sample only exhibits significant RC emission in isolated regions, which is attributed to both the episodic nature of SF in dwarf galaxies (e.g., Stinson et al. 2007) and the surface brightness sensitivity of our RC observations, which limits our RC maps to detecting SFRDs greater than $\sim 5 \times 10^{-3} M_{\odot} \text{ yr}^{-1} \text{ kpc}^{-2}$. When integrated over the disk, the signal from most galaxies is dominated by the contribution of noise from the individual beams within the integration area. The uncertainty, δN , is given by $\sigma_{\text{rms}} \sqrt{N}$, where σ_{rms} is the rms noise level and N is the number of individual beams. This motivates the use of masks to isolate genuine emission from background noise (i.e., reduce the integration area, which is proportional to N) in order to improve the RC S/N.

3.4.1. Radio Continuum-based Mask

To characterize the RC emission within our images, we first estimate the spatially varying background noise across each image using the BANE algorithm (Hancock et al. 2012). BANE works by selecting each pixel in the image on a specified grid and then defines a boxed region. This region is first clipped at 3σ to remove the contribution of source pixels. The median of the remaining pixels in the box is calculated and used as the background estimate. Linear interpolation is then used to smooth the background across the image. We found that the default options for BANE, which uses a grid size of four times the beam area and a box size of five times the grid size, produced good estimates of the background noise for the majority of our images. In cases where there is large-scale extended emission such as NGC 1569 and IC 10, the grid size was increased to the approximate size of the most extended feature in the image, six and nine, respectively, and the default box size was applied. Estimating the background noise allows us to create S/N images that account for local variations in the image background caused by the primary beam sensitivity pattern and any residual low-level artifacts. This results in a robust threshold for our source detection. The average noise toward our galaxies is presented in Table 2, column 9.

We apply an automated approach to source identification using the FELLWALKER source finding algorithm (Berry 2015) available in the STARLINK distribution CUPID. FELLWALKER is a thresholding approach to source detection that identifies contiguous features in an image by finding the steepest gradient for each pixel. Starting with the first pixel in an image, above a user-defined threshold, each of the surrounding pixels is inspected to locate the pixel with the highest ascending gradient; this process continues until a peak is located (i.e., a pixel surrounded by flat or descending gradients). The pixels along this path are assigned an arbitrary integer to represent their connection along a path. All pixels in the image are inspected in a similar process, and the image is segmented into clumps by grouping together all paths that lead to the same peak value. The pixels belonging to paths that lead to the same peak are then defined as belonging to that particular clump. For a full description of this process, see Berry et al. (2007).

Using FELLWALKER, we create two masks for each S/N image: the first is at full resolution while the second is smoothed to an angular resolution of $10''$. The former image is used to characterize unresolved point sources while the latter is used to define regions of extended emission. We assign a threshold level corresponding to an S/N level of 3 in both cases where the noise levels are derived independently for each image. Fluctuations that are smaller than the beam are excluded; they are identified as noise spikes. We verify the robustness of this approach by comparing our mask to those produced by the CLUMPFIND algorithm, which is also available in CUPID, and by checking each mask by eye to ensure that no spurious emission is included in the maps. An example of the results of this approach can be seen in the top-right panel of Figure 3 and Appendix B.

Using our RC-based mask, we extract the integrated properties toward our sample of dwarf galaxies excluding background and ambiguous sources and present the results in Table 4. A table containing the integrated properties including ambiguous sources can be found in Appendix C in Table 8.

In order to compare the RC emission to our ancillary data, we first investigate which masks best represent the global

Table 3
Integrated Emission Over the Disk of the LITTLE THINGS Galaxies, Excluding Ambiguous Sources

Galaxy	Size	P.A.	6 cm RC	H α (10^{-13} erg s $^{-1}$ cm $^{-2}$)	FUV	24 μ m MIR	70 μ m FIR	6 cm RC $_{\text{Nth}}$	B_{eq}
(1)	($'$) (2)	($^{\circ}$) (3)	(mJy) (4)	(5)	(mJy) (6)	(10^{-2} Jy) (7)	(10^{-2} Jy) (8)	(mJy) (9)	(μ G) (10)
CVn I dwA	1.7 \times 1.4	80	>0.29	1.95 \pm 0.03	1.04 \pm 0.11	0.15 \pm 0.06	2.46 \pm 0.04	>0.29	<2
DDO 43	1.8 \times 1.2	6	>0.99	1.28 \pm 0.03	1.07 \pm 0.11	>0.99	<2
DDO 46 ^V	3.8 \times 3.4	84	>1.16	1.08 \pm 0.02	1.75 \pm 0.17	>1.16	<2
DDO 47	4.5 \times 2.3	-79	>0.61	3.00 \pm 0.03	3.00 \pm 0.30	>0.61	<2
DDO 50	7.9 \times 5.7	18	6.70 \pm 0.60	60.10 \pm 0.49	41.95 \pm 4.20	17.27 \pm 0.01	319.90 \pm 0.28	0.99 \pm 0.60	<2
DDO 52	2.2 \times 1.4	4	>1.28	0.29 \pm 0.01	0.61 \pm 0.06	-0.04 \pm 0.02	1.81 \pm 0.05	>1.28	<1
DDO 53	2.7 \times 1.4	81	0.65 \pm 0.13	4.32 \pm 0.04	2.55 \pm 0.26	2.32 \pm 0.02	24.05 \pm 0.03	0.24 \pm 0.13	<1
DDO 63	4.3 \times 4.3	0	>0.71	4.39 \pm 0.04	5.03 \pm 0.50	1.77 \pm 0.01	3.74 \pm 0.13	>0.71	<1
DDO 69	4.8 \times 2.7	-64	>0.89	1.66 \pm 0.01	4.67 \pm 0.47	-0.65 \pm 0.01	11.08 \pm 0.07	>0.89	<1
DDO 70	7.4 \times 4.4	88	>1.48	6.27 \pm 0.04	11.53 \pm 1.15	0.59 \pm 0.01	63.09 \pm 0.13	>1.48	<1
DDO 75	6.2 \times 5.2	42	>2.04	40.44 \pm 0.10	29.46 \pm 2.95	0.20 \pm 0.01	77.89 \pm 0.20	>2.04	<1
DDO 87	2.3 \times 1.3	76	>0.70	0.68 \pm 0.01	0.65 \pm 0.06	0.07 \pm 0.02	7.03 \pm 0.03	>0.70	<2
DDO 101	2.1 \times 1.5	-69	>1.79	0.82 \pm 0.01	0.39 \pm 0.04	0.24 \pm 0.02	-0.54 \pm 0.04	>1.79	<2
DDO 126	3.5 \times 1.7	-41	>0.57	3.66 \pm 0.08	2.91 \pm 0.29	0.32 \pm 0.03	14.92 \pm 0.10	>0.57	<2
DDO 133	4.7 \times 3.2	-6	>1.17	4.55 \pm 0.03	4.09 \pm 0.41	0.53 \pm 0.01	33.04 \pm 0.13	>1.17	<2
DDO 154	3.1 \times 1.6	46	>1.73	2.21 \pm 0.02	3.77 \pm 0.38	0.28 \pm 0.03	3.66 \pm 0.04	>1.73	<1
DDO 155	1.9 \times 1.3	51	>0.47	4.85 \pm 0.05	...	0.22 \pm 0.03	16.15 \pm 0.05	>0.47	<2
DDO 165	4.3 \times 2.3	89	>1.19	1.53 \pm 0.01	...	0.04 \pm 0.01	10.64 \pm 0.06	>1.19	<2
DDO 167	1.5 \times 1.0	-24	>0.51	0.80 \pm 0.01	1.05 \pm 0.11	>0.51	<3
DDO 168	4.6 \times 2.9	-25	>0.94	5.91 \pm 0.03	5.55 \pm 0.56	0.67 \pm 0.01	41.94 \pm 0.10	>0.94	<1
DDO 187	2.1 \times 1.7	37	>1.17	0.57 \pm 0.01	1.15 \pm 0.12	-0.02 \pm 0.03	-1.94 \pm 0.09	>1.17	<1
DDO 210	2.6 \times 1.3	-85	>0.87	...	0.80 \pm 0.08	-0.16 \pm 0.02	5.26 \pm 0.04	>0.87	<2
DDO 216	8.0 \times 3.6	-58	>1.28	0.09 \pm 0.01	2.00 \pm 0.20	-0.12 \pm 0.01	9.87 \pm 0.08	>1.28	<1
F564-V03 ^V	1.3 \times 1.0	7	>0.35	...	0.10 \pm 0.01	>0.35	<3
Haro 29	1.7 \times 1.0	85	2.14 \pm 0.11	13.02 \pm 0.45	3.02 \pm 0.32	5.83 \pm 0.05	39.00 \pm 0.05	0.91 \pm 0.12	6
Haro 36 ^V	1.5 \times 1.2	90	0.94 \pm 0.09	2.41 \pm 0.03	2.84 \pm 0.29	0.94 \pm 0.04	23.66 \pm 0.06	0.71 \pm 0.09	5
IC 1613	18.2 \times 14.7	71	4.49 \pm 0.55	55.81 \pm 0.87	91.86 \pm 9.24	6.85 \pm 0.02	408.70 \pm 1.73	-0.77 \pm 0.55	<1
IC 10 ^V	11.6 \times 9.1	-38	96.38 \pm 0.81	1191.00 \pm 5.73	...	3741.00 \pm 4.83	9547.00 \pm 12.08	-16.78 \pm 0.97	<1
LGS 3	1.9 \times 1.0	-3	>0.57	...	0.08 \pm 0.01	>0.57	<2
M81 dwA ^V	1.5 \times 1.1	86	>1.28	...	0.38 \pm 0.04	>1.28	<2
Mrk 178	2.0 \times 0.9	-51	1.01 \pm 0.14	5.38 \pm 0.09	2.56 \pm 0.27	0.45 \pm 0.03	0.45 \pm 0.01	0.50 \pm 0.14	5
NGC 1569 ^V	2.3 \times 1.3	-59	149.60 \pm 0.31	486.70 \pm 3.02	746.50 \pm 75.63	705.50 \pm 13.61	3543.00 \pm 2.66	71.38 \pm 0.57	17
NGC 2366	9.4 \times 4.0	33	9.66 \pm 0.59	96.38 \pm 1.11	37.26 \pm 3.73	65.47 \pm 0.01	506.20 \pm 0.30	0.51 \pm 0.60	17
NGC 3738	4.8 \times 4.8	0	2.62 \pm 0.48	16.26 \pm 0.17	11.22 \pm 1.13	11.65 \pm 0.03	248.10 \pm 0.41	1.07 \pm 0.48	17
NGC 4163	2.9 \times 1.9	18	>0.69	1.48 \pm 0.02	2.68 \pm 0.27	0.43 \pm 0.03	10.20 \pm 0.11	>0.69	<2
NGC 4214	9.3 \times 8.5	16	27.78 \pm 0.57	178.60 \pm 0.92	80.72 \pm 8.08	199.60 \pm 0.01	2393.00 \pm 1.13	10.81 \pm 0.57	6
Sag DIG ^V	4.3 \times 2.3	88	>2.47	1.28 \pm 0.01	4.52 \pm 0.45	>2.47	<1
UGC 8508	2.5 \times 1.4	-60	0.38 \pm 0.13	2.75 \pm 0.04	...	0.37 \pm 0.03	12.52 \pm 0.04	0.12 \pm 0.13	<1
VIIZw 403	2.2 \times 1.1	-11	1.37 \pm 0.10	7.48 \pm 0.15	3.67 \pm 0.38	1.87 \pm 15.06	57.05 \pm 1.36	0.66 \pm 0.10	5
WLM	11.6 \times 5.1	-2	>2.51	16.81 \pm 0.06	29.53 \pm 2.96	4.61 \pm 0.01	117.70 \pm 0.18	>2.51	<1

Note. (Column 1) Name of dwarf galaxy. The superscript “V” means that disk properties (columns 2–5) are taken from V-band data; for all others, properties are taken from the B-band; (Columns 2 and 3) Size (major and minor axes) and position angle (P.A.) of the optical disk (Hunter & Elmegreen 2006); (Column 4) 6 cm (\sim 6 GHz) radio continuum flux density. This value and those following have ambiguous sources removed. For values where we retain ambiguous sources, see Appendix C; (Column 5) H α flux; (Column 6) GALEX FUV flux density; (Column 7) *Spitzer* 24 μ m MIR flux density; (Column 8) *Spitzer* 70 μ m FIR flux density; (Column 9) 6 cm (\sim 6 GHz) radio continuum nonthermal (synchrotron) flux density. All RC $_{\text{Nth}}$ emission is assumed to be synchrotron and is inferred by subtracting the RC $_{\text{Th}}$ component from the total RC following Deeg et al. (1997). The quantity in parentheses is the amount that was regarded as ambiguous. (Column 10) Equipartition magnetic field strength in the plane of the sky (see Equation (3) in Beck & Krause 2005).

emission in our dwarf galaxies. Ideally, we would like to compare the various quantities over the same optically derived disk mask since our ancillary data is general present emission over a large fraction of the disk. However, if we integrate the RC emission over the disk, we find that only 11 of our 40 observations have significant integrated RC flux density measurements. Using instead our RC mask, we identify RC emission associated with 22 of the 40 LITTLE THINGS galaxies (excluding ambiguous sources); eight are new RC detections. It is for this reason that in the course of the analysis

of our data we will present results integrated over both the RC- and disk-based masks.

3.5. Radio Continuum Source Counts

To test the robustness of our source identification and extraction approach, we determine the radio continuum source counts from our images. We compare these to Huynh et al. (2012), who performed 5.5 GHz observations with the Australia Telescope Compact Array of a 900 arcmin 2 region with a restoring beam of 4 $'$ 9 \times 2 $'$ 0 and an rms noise of

Table 4
Integrated Emission Over the RC Mask of the LITTLE THINGS Galaxies, Excluding Ambiguous Sources

Galaxy	R.A	Decl.	f_{disk}	6 cm RC	H α	FUV	24 μm MIR	70 μm FIR	6 cm RC _{Nth}	B_{eq}
(1)	hh mm ss.s	dd mm ss.s	(%)	(mJy)	(10^{-13} erg s $^{-1}$ cm $^{-2}$)	(mJy)	(10^{-2} Jy)	(10^{-2} Jy)	(mJy)	(μG)
	(2)	(3)	(4)	(5)	(6)	(7)	(8)	(9)	(10)	(11)
DDO 46	07 41 26.6	+40 06 39	0.1	0.02 \pm 0.01	0.16 \pm 0.01	0.02 \pm 0.01	0.01 \pm 0.01	<1
DDO 47	07 41 55.3	+16 48 08	0.1	0.03 \pm 0.01	0.15 \pm 0.01	0.05 \pm 0.01	0.02 \pm 0.01	<1
DDO 50	08 19 08.7	+70 43 25	2.2	6.27 \pm 0.09	25.28 \pm 0.42	7.45 \pm 0.76	7.69 \pm 0.06	53.17 \pm 0.04	3.95 \pm 0.10	4
DDO 53	08 34 08.0	+66 10 37	3.2	0.33 \pm 0.02	1.90 \pm 0.04	0.71 \pm 0.07	1.32 \pm 0.09	5.30 \pm 0.01	0.16 \pm 0.02	4
DDO 63	09 40 30.4	+71 11 02	0.1	0.06 \pm 0.01	0.24 \pm 0.01	0.14 \pm 0.02	0.04 \pm 0.34	0.33 \pm 0.01	0.04 \pm 0.01	2
DDO 70	10 00 00.9	+05 19 50	0.1	0.07 \pm 0.02	0.29 \pm 0.02	0.21 \pm 0.03	0.03 \pm 0.34	0.34 \pm 0.01	0.04 \pm 0.02	<1
DDO 75	10 10 59.2	-04 41 56	0.3	0.24 \pm 0.03	2.87 \pm 0.06	0.85 \pm 0.09	0.07 \pm 0.23	1.61 \pm 0.01	0.01 \pm 0.01	<1
DDO 126	12 27 06.5	+37 08 23	2.3	0.35 \pm 0.03	1.46 \pm 0.07	0.54 \pm 0.06	0.15 \pm 0.20	2.11 \pm 0.02	0.23 \pm 0.03	3
DDO 155	12 58 39.8	+14 13 10	5.2	0.28 \pm 0.04	2.23 \pm 0.04	...	0.15 \pm 0.12	2.42 \pm 0.01	0.08 \pm 0.04	<1
DDO 168	13 14 27.2	+45 55 46	0.2	0.11 \pm 0.01	0.24 \pm 0.01	0.12 \pm 0.01	0.04 \pm 0.18	0.67 \pm 0.01	0.09 \pm 0.01	2
Haro 29	12 26 16.7	+48 29 38	13.4	2.01 \pm 0.04	12.54 \pm 0.45	2.65 \pm 0.29	4.96 \pm 0.14	21.21 \pm 0.02	0.82 \pm 0.06	6
Haro 36	12 46 56.3	+51 36 48	9.3	0.37 \pm 0.03	1.17 \pm 0.03	1.94 \pm 0.21	0.41 \pm 0.13	6.88 \pm 0.02	0.26 \pm 0.03	4
IC 1613	01 04 49.2	+02 07 48	0.7	2.51 \pm 0.05	10.26 \pm 0.43	5.08 \pm 0.71	1.69 \pm 0.23	23.10 \pm 0.12	1.63 \pm 0.06	3
IC 10	00 20 17.5	+59 18 14	22.9	99.33 \pm 0.39	887.90 \pm 5.68	...	1369.00 \pm 10.10	5482.00 \pm 6.68	14.96 \pm 0.66	8
Mrk 178	11 33 29.0	+49 14 24	3.8	0.46 \pm 0.03	2.33 \pm 0.08	0.97 \pm 0.12	0.16 \pm 0.17	0.16 \pm 0.01	0.25 \pm 0.03	4
NGC 1569	04 30 49.8	+64 50 51	126.3	155.40 \pm 0.34	503.90 \pm 3.03	755.60 \pm 76.53	716.20 \pm 12.11	3758.00 \pm 2.99	74.41 \pm 0.60	17
NGC 2366	07 28 48.8	+69 12 22	2.2	11.98 \pm 0.09	66.97 \pm 1.10	12.64 \pm 1.28	52.01 \pm 0.04	179.50 \pm 0.05	5.65 \pm 0.14	5
NGC 3738	11 35 49.0	+54 31 23	6.2	2.98 \pm 0.12	11.83 \pm 0.17	7.29 \pm 0.75	7.58 \pm 0.13	91.12 \pm 0.10	1.85 \pm 0.12	7
NGC 4214	12 15 39.2	+36 19 38	2.2	22.58 \pm 0.08	117.20 \pm 0.91	32.63 \pm 3.29	140.40 \pm 0.09	941.10 \pm 0.17	11.55 \pm 0.12	6
UGC 8508	13 30 44.9	+54 54 29	3.2	0.16 \pm 0.02	0.65 \pm 0.02	...	0.06 \pm 0.15	1.18 \pm 0.01	0.10 \pm 0.02	2
VII Zw 403	11 27 58.2	+78 59 39	15.8	1.29 \pm 0.04	6.49 \pm 0.15	3.21 \pm 0.33	2.10 \pm 37.85	33.77 \pm 0.54	0.68 \pm 0.04	5
WLM	00 01 59.2	-15 27 41	0.1	0.16 \pm 0.02	0.79 \pm 0.05	0.10 \pm 0.01	0.27 \pm 0.30	0.31 \pm 0.01	0.01 \pm 0.01	<1

Note. (Column 1) Name of dwarf galaxy; (Columns 2 and 3) Equatorial coordinates (J2000) of center of the galaxy defined by the optical disk; (Column 4) Fraction of the disk (see Table 3) that has significant RC emission; (Column 5) 6 cm (\sim 6 GHz) radio continuum flux density. This value and those following have ambiguous sources removed. For values where we retain ambiguous sources, see Appendix C; (Column 6) H α flux; (Column 7) *GALEX* FUV flux density; (Column 8) *Spitzer* 24 μm MIR flux density; (Column 9) *Spitzer* 70 μm FIR flux density; (Column 10) 6 cm (\sim 6 GHz) radio continuum nonthermal (synchrotron) flux density. All RC_{Nth} emission is assumed to be synchrotron and is inferred by subtracting the RC_{Th} component from the total RC following Deeg et al. (1997). The quantity in parentheses is the amount that was regarded as ambiguous. (Column 11) Equipartition magnetic field strength in the plane of the sky (see Equation (3) in Beck & Krause 2005).

Table 5
6 cm Source Counts

ΔS (μJy)	N			N_c			dN_c/dS			N_c/N_{exp}		
	all	bg	amb	all	bg	amb	all	bg	amb	all	bg	amb
46–73	60	50	52	180.18	150.15	156.15	1983.58	1652.99	1719.11	0.44 ± 0.03	0.37 ± 0.03	0.38 ± 0.03
73–116	52	40	42	125.43	96.48	101.31	785.19	603.99	634.19	0.60 ± 0.05	0.46 ± 0.05	0.49 ± 0.05
116–183	55	37	43	124.68	83.87	97.47	485.42	326.55	379.51	1.23 ± 0.11	0.83 ± 0.09	0.96 ± 0.10
183–290	25	15	18	55.52	33.31	39.98	132.29	79.37	95.25	1.08 ± 0.15	0.65 ± 0.11	0.78 ± 0.12
290–460	24	15	16	52.78	32.99	35.19	78.56	49.10	52.37	2.04 ± 0.28	1.27 ± 0.22	1.36 ± 0.23
460–728	26	17	17	56.74	37.10	37.10	55.06	36.00	36.00	4.39 ± 0.58	2.87 ± 0.47	2.87 ± 0.47
728–1155	10	3	5	21.65	6.50	10.83	12.93	3.88	6.47	3.34 ± 0.72	1.00 ± 0.39	1.67 ± 0.51
1155–1831	13	3	5	27.96	6.45	10.75	10.68	2.47	4.11	8.61 ± 1.63	1.99 ± 0.78	3.31 ± 1.01
1831–2901	6	1	1	12.86	2.14	2.14	3.74	0.62	0.62	7.91 ± 2.20	1.32 ± 0.90	1.32 ± 0.90
2901–4598	7	0	1	14.90	0.00	2.13	2.53	0.00	0.36	18.27 ± 4.73	0.00 ± 0.00	2.61 ± 1.79
4598–11478	9	1	1	18.98	2.11	2.11	1.29	0.14	0.14	31.03 ± 7.12	3.45 ± 2.37	3.45 ± 2.37
11478–28653	11	0	0	23.03	0.00	0.00	0.63	0.00	0.00	148.48 ± 30.94	0.00 ± 0.00	0.00 ± 0.00

Note. 6 cm (6.2 GHz) source counts. (Column 1) flux density bins taken from Huynh et al. (2012) converted to 6.2 GHz assuming a spectral index of -0.7 ; (Column 2) number of $>5\sigma_{\text{rms}}$ RC source counts. We count all sources in the images (all), sources identified as background (bg), and sources identified as background or ambiguous (amb). (Column 3) the completeness and resolution-corrected RC source counts. (Column 4) the corrected RC source count rate—the number of sources found per steradian normalized to the midpoint of the flux density bin. (Column 5) corrected source counts normalized by the expected number from a non-evolving Euclidean model.

$12 \mu\text{Jy beam}^{-1}$. After correcting for incompleteness and resolution bias, they present normalized source counts in 10 flux density bins ranging between 50 and 5000 μJy (see their Table 2).

Our images were generated using a restoring beam of approximately $3''$ and attained an rms noise of $\sim 6 \mu\text{Jy beam}^{-1}$. Therefore, the sensitivity per beam in our data is comparable to that from Huynh et al. (2012). We scale the Huynh et al. (2012) bins to 6.2 GHz, the effective frequency for most of our images, assuming a spectral index of -0.7 ± 0.2 . This assumption is supported by various studies that show that the average spectral index of star-forming galaxies is narrowly concentrated around ~ -0.7 with a small dispersion of $\lesssim 0.2$ (Condon 1992; Niklas et al. 1997; Lisenfeld & Volk 2000). For each bin, we cycled through our images, counting all sources with flux densities in the range ΔS . We count sources only from within a $4'$ circular aperture centered on the image pointing reference to avoid regions where the primary beam response leads to higher noise levels. Sources are assigned to three different groups following our source classification approach described in Section 3.1. The first group includes all sources in the field including the galaxy emission, the second counts only sources we are confident are background sources, and the final group consists of both background and ambiguous sources. Sources were not counted if, in the given bin, the low end of the bin was less than five times the rms noise from the image (this only affected the two lowest bins because of a few high rms images). No attempt was made to count resolved sources originating from the same source (e.g., radio lobes, multiple SF regions from a dwarf, etc.).

To estimate the completeness of our source catalog, we follow a similar approach to Huynh et al. (2012) and perform a Monte Carlo simulation. We inject a synthetic Gaussian source with a randomly generated position and brightness from 30 to 3000 μJy into our image and then apply the FELLWALKER source detection algorithm following the same approach as described in Section 3.4 to see if the source is recovered. We do

this 8000 times and find that sources with flux densities of $5\sigma_{\text{rms}}$ ($\sim 50 \mu\text{Jy}$) have a detection rate of 50%, where σ_{rms} is the rms noise in the image. The detection rate rises steeply to 90% at 120 μJy . We also correct for the resolution bias following the same approach as Huynh et al. (2012). This correction accounts for sources with weak extended emission and large total integrated flux densities that have peaks that fall below the detection threshold. Given our slightly higher sensitivity and resolution, we find lower resolution correction factors than Huynh et al. (2012), with values of 1.24 in our lowest bin and 1.03 in our highest bin.

We present the results of our source counts in Table 5. For each bin, we present the raw source counts (N) and the counts corrected for completeness and resolution bias (N_c). We determine the RC source count rate (dN_c/dS), which corresponds to the number of sources found per steradian normalized to the midpoint of the flux bin. Finally, we normalize our corrected source counts by dividing by the expected number of sources (N_{exp}) derived from a non-evolving Euclidean model using the relation $N(>S_{6\text{cm}}) = 60 * S_{6\text{cm}}^{-1.5}$. The Poissonian errors are presented for the normalized and corrected counts with the resolution and completeness correction uncertainties (10% and 2%–5%, respectively) added in quadrature.

In Figure 4, we present a comparison of our source counts using all sources (black squares), only background sources (blue triangles), and both background and ambiguous sources (green pentagons). We compare our results to the corrected and normalized source counts of Huynh et al. (2012; red circles). This plot clearly shows that our counts are consistent with those of Huynh et al. (2012) until $\sim 10^3 \mu\text{Jy}$. Beyond this flux, we see that including galaxy emission in our source counts leads to higher counts than those found in Huynh et al. (2012), particularly at flux densities above 8.6 mJy. Ideally, we would like to use the source counts to test the reliability of our source identification approach. In particular, we would like to test whether sources we define as ambiguous are background

Table 6

The Best-fit Parameters for the RC–SFR, FIR–SFR, and RC–FUV Relation for the Total RC, RC_{Th}, and RC_{Nth} Components Integrated Over the Entire Disk and Only Over the RC Masks

Mask	RC Luminosity–SFR Relation			<i>N</i>	<i>P</i>	<i>S</i>
	<i>A</i>	<i>n</i>	σ			
RC _{Disk} –SFR	20.05 ± 0.22	0.93 ± 0.14	0.23	11	0.87	0.93
RC _{Mask} –SFR	20.16 ± 0.12	0.86 ± 0.04	0.17	19	0.92	0.96
RC _{Th,Disk} –SFR	20.21 ± 0.19	1.20 ± 0.09	0.23	32	0.95	0.88
RC _{Th,Mask} –SFR	19.75 ± 0.16	0.82 ± 0.05	0.22	19	0.92	0.90
RC _{Nth,Disk} –SFR	19.72 ± 0.08	0.82 ± 0.06	0.08	6	0.99	1.00
RC _{Nth,Mask} –SFR	19.78 ± 0.14	0.79 ± 0.06	0.17	14	0.89	0.91
FIR _{Disk} –SFR	22.74 ± 0.20	1.07 ± 0.09	0.26	24	0.80	0.88
FIR _{Mask} –SFR	22.68 ± 0.16	1.05 ± 0.06	0.20	15	0.77	0.93
RC _{Disk} –FIR	17.31 ± 0.16	1.02 ± 0.10	0.18	12	0.93	0.80
RC _{Mask} –FIR	17.94 ± 0.04	0.81 ± 0.03	0.14	18	0.89	0.94

Note. (1) RC component and mask type; (2) and (3) fit parameters; (4) scatter of the data; (5) number of galaxies used in the fit; (6) and (7) The Pearson (*P*) and Spearman (*S*) coefficients.

sources or associated with the galaxy emission. If we assume that our source identification approach has reliably identified the galaxy emission and background sources and that the bulk of our ambiguous sources are associated with one of these groups, then we should see a signature of this in our source counts. If the ambiguous sources belong to the background sources group, we would expect that including them in the source counts while excluding the galaxy emission would lead to source counts that are similar to those of Huynh et al. (2012). Conversely, if the ambiguous sources are background sources and we do not count them while also excluding the galaxy emission, we would expect to see lower source counts than expected. In Figure 4, we do see some tentative evidence that suggests the ambiguous sources are background sources with the background-only source counts (blue triangles) tending to be lower than the source counts including both the background and ambiguous sources (green pentagons). However, due to the small number of sources in each bin and the associated errors, we are prevented from stating that, statistically, the ambiguous sources belong to the population of background sources.

4. Discussion

4.1. The Radio Continuum

4.1.1. Comparison with Literature Flux Densities

There are few significant RC detections of dwarf galaxies in the literature. Of the galaxies that overlap with our sample, the literature is dominated by nondetections (e.g., Altschuler et al. 1984; Wynn-Williams & Becklin 1986; Klein et al. 1992; Hoeppe et al. 1994). On closer inspection, the seemingly high detection rate of 40% in Klein (1986) is actually dominated by 1σ – 3σ detections, which are likely influenced by the inclusion of background galaxies in the large Effelsberg 100 m single-dish beam. We are therefore limited by the number of dwarf galaxies with flux densities in the literature that we can confidently compare our results against.¹¹

¹¹ We note that the flux densities for sources found in the literature may be derived from a range of absolute flux density scales. Commonly used absolute flux scales include Baars et al. (1977), Perley & Butler (2013), and Scaife & Heald (2012). Variations of the absolute flux scale among these different standards are on the order of 5% (Perley & Butler 2017).

Reliable RC detections in the literature mostly come from deeper case studies of individual dwarf galaxies. Below we compare our RC flux density integrated over the RC mask that includes ambiguous sources (see Appendix C) to the few studies available in the literature.

NGC 1569: Lisenfeld et al. (2004) find a VLA 8.415 GHz flux density of 125 ± 12 mJy and spectral index of -0.47 . The same spectral index was found by Kepley et al. (2010; see their Figure 3). Scaling the 8.415 GHz flux density we find an equivalent 6.2 GHz flux density of 144 ± 14 mJy, which agrees with our measurement of 157.30 ± 0.35 mJy. Single-dish observations performed by the Green Bank telescope at 4.85 GHz (Gregory & Condon 1991) found a flux density of 202 mJy. If we scale this to 6.2 GHz, assuming a spectral index of -0.47 , we find a flux density of 180.0 mJy. This suggests that we may be missing approximately 12.8 mJy ($\sim 9\%$) of the flux in our image.

NGC 4214: Kepley et al. (2011) find a VLA 4.86 GHz flux density of 34.0 ± 6.8 mJy (D-array) and spectral index of -0.43 . The equivalent 6.2 GHz flux density is 30 ± 6 mJy while we find 23.16 ± 0.09 mJy. We compare our flux density to that of Gregory & Condon (1991) and find that our measured flux density is 3.8 mJy ($\sim 14\%$) lower. We note that this suggests that we have missed large-scale emission.

DDO 50: Tongue & Westpfahl (1995) find a VLA 6 cm flux density of 11.7 ± 0.1 mJy (D-array), which is higher than the 6.81 ± 0.09 mJy at 6.2 GHz that we measured. Again, we note that there is the possibility that we have missed large-scale emission.

NGC 2366: In the absence of a literature flux density at 6 cm, we resort to a comparison with an *L*-band value. Condon et al. (2002) find a 1.4 GHz flux density of 19.9 mJy while we report a 6.2 GHz flux density of 12.05 ± 0.09 mJy. This implies a spectral index of -0.34 ± 0.10 , which is plausible. In light of this, it is unlikely that we have missed large-scale emission, which would flatten the spectral index and would imply emission even more dominated by RC_{Th} emission than derived here.

NGC 3738: Stil & Israel (2002) find a 1.4 GHz flux density of 13 ± 2 mJy and we find a 6.2 GHz flux density of 2.62 ± 0.048 mJy. This implies a spectral index of

-1.08 ± 0.04 , which is quite steep. Our image is affected by artifacts from a nearby bright source which may be influencing our flux density measurement.

Haro 29: Condon et al. (1998) find a 1.4 GHz flux density of 4.5 ± 0.5 mJy, whereas we find a 6.2 GHz flux density of 2.18 ± 0.11 mJy. This implies a spectral index of -0.49 ± 0.08 , which is plausible.

Others: Klein (1986) find a number of $\sim 4\sigma$ detections at 4.75 GHz: 3.5 ± 1.0 mJy for DDO 126, 4 ± 1 mJy for DDO 133, and 9 ± 2 mJy for DDO 52. However, we observe less than a mJy for each of these. In all cases, we find nearby background galaxies that will have entered their $2'30''$ single-dish beam and contributed to their flux density to some degree.

4.1.2. Composition of the Radio Continuum: Thermal and Nonthermal Contributions

The total RC emission comprises two contributions: RC_{Th} and RC_{Nth} . Since the $\text{H}\alpha$ and RC_{Th} both have their origins in hot ($\sim 10^4$ K) plasma associated with H II regions, a tight spatial and temporal correlation between the two is expected (e.g., Deeg et al. 1997; Murphy et al. 2011). The $\text{H}\alpha$ – RC_{Th} relation taken from Deeg et al. (1997) assumes the form

$$\frac{\text{RC}_{\text{Th}}}{\text{W m}^{-2}} = 1.14 \times 10^{-25} \left(\frac{\nu}{\text{GHz}} \right)^{-0.1} \times \left(\frac{T_e}{10^4 \text{ K}} \right)^{0.34} \frac{F_{\text{H}\alpha}}{\text{erg s}^{-1} \text{ cm}^{-2}}, \quad (1)$$

where ν is the observed frequency in GHz, T_e is the electron temperature, which is assumed to be 10^4 K, and $F_{\text{H}\alpha}$ is the $\text{H}\alpha$ luminosity. On a spatially resolved basis, the RC_{Th} flux density can be subtracted from the total RC, yielding the RC_{Nth} flux density distribution.

We do not correct our $\text{H}\alpha$ estimates for internal extinction, following the same approach as Heesen et al. (2014). As our later analysis utilizes the SFR derived by combining the $24 \mu\text{m}$ and FUV emission, we wish to avoid using the $24 \mu\text{m}$ to correct for internal extinction so as not to introduce a spurious correlation. Dwarf galaxies are expected to have low internal extinction due to their low metallicity, and therefore, this is thought to generally not have a significant impact on our results. To verify this assertion, we estimate the internal extinction in our $\text{H}\alpha$ maps following the method of Kennicutt et al. (2009):

$$I_{\text{H}\alpha, \text{corr}} = I_{\text{H}\alpha, \text{obs}} + 0.02\nu_{24\mu\text{m}} I_{24\mu\text{m}}, \quad (2)$$

where $I_{\text{H}\alpha, \text{obs}}$ is the observed $\text{H}\alpha$ intensity, which has been corrected for foreground reddening, $I_{\text{H}\alpha, \text{corr}}$ is the $\text{H}\alpha$ intensity corrected for internal extinction, and $I_{24\mu\text{m}}$ is the $24 \mu\text{m}$ intensity. Our most intensely star-forming galaxies are IC 10 and NGC 1569. We calculate the average internal extinction toward these galaxies and find values of 38% and 35%, respectively. We have explored the extinction toward NGC 1569 in Westcott et al. (2017) using a Bayesian approach to separate the RC emission. We were able to estimate an average internal extinction of $\sim 20\%$, slightly lower than our estimate above. Galaxies with lower SFR, $< 0.1 M_{\odot} \text{ yr}^{-1}$, that make up the bulk of our sample have much lower internal extinctions of $< 10\%$ as derived from the $24 \mu\text{m}$ intensity. For example, VII Zw 403 and DDO 50 both have an internal

extinction of $\sim 8\%$. In light of these results, we caution that in our subsequent analysis the RC_{Th} flux estimates in galaxies with higher SFRs may be underestimated.

The uncertainty in our estimate of the RC_{Th} emission is dominated by the foreground Galactic extinction correction and T_e . The uncertainty in the Galactic extinction correction for our sample is ± 0.015 mag for values of $E(B - V) \leq 0.015$ and $\sim 10\%$ for $E(B - V) > 0.015$ (Burstein & Heiles 1982). We assume a single value for the foreground extinction across each galaxy. The foreground extinction may vary considerably across each galaxy, particularly for those galaxies in close proximity to the Milky Way, such as IC 10, where the foreground extinction has been shown to vary across the face of the galaxy from -60% to $+25\%$ of our assumed value (Basu et al. 2017).

The value of T_e is assumed to be the standard value of 10^4 K but the electron temperature in H II regions has been shown to vary considerably. For example, a sample of 61 Galactic H II regions were found to have values of T_e ranging from 0.25×10^4 K to 1.16×10^4 K (Hindson et al. 2016). In a study by Nicholls et al. (2014) the mean electron temperature of 17 H II regions in 14 dwarf irregular galaxies was $T_e = 1.4 \times 10^4$ K. Variations in the electron temperature from our assumed value could give rise to up to $\sim 20\%$ error in the estimated thermal emission.

After the removal of known background galaxies and ambiguous sources, we apply our RC and disk masks to isolate the RC_{Th} (scaled $\text{H}\alpha$) emission. When integrating over the RC mask, we find that the average thermal fraction for our sample is $\sim 50\% \pm 10\%$ (upper limit). When integrating over the entire disk, we find a higher thermal fraction of $70\% \pm 10\%$. For comparison, we scale thermal fractions reported for dwarf galaxies in the literature to 6.2 GHz assuming a spectral index of -0.1 and -0.7 for thermal and nonthermal components, respectively. The scaled thermal fractions in dwarf galaxies have been quoted as 51% for a sample of stacked faint dwarfs (Roychowdhury & Chengalur 2012), 53% in IC 10 (Heesen et al. 2011), 41% in NGC 1569 (Lisenfeld et al. 2004), and 41% in NGC 4449 (Niklas et al. 1997). Our estimate of the thermal fraction integrated over the RC mask is consistent with these literature values. The thermal fraction integrated over the disk mask is significantly greater. We ignore internal extinction in our estimate of the RC_{Th} , which may lead to slightly lower values of the thermal fraction in the high-SFR galaxies such as NGC 1569 and IC 10. It is also possible that on the scale of the disk, we are missing some flux associated with large-scale RC emission, which would lead to higher thermal fractions in the most extended galaxies. A more robust measure of the RC_{Th} emission may be obtained using a Bayesian approach (Tabatabaei et al. 2017; Westcott et al. 2017); however, this requires a large number of observations across the radio SED.

To estimate the RC_{Nth} emission, we subtract the RC_{Th} emission from the total RC. We caution that the RC_{Nth} emission may in some cases turn out to be rather an upper limit because of the previous points.

4.2. The RC–SFR Relation

We estimate the SFR following the approach of Leroy et al. (2012). This corrects the FUV-inferred SFR for internal extinction, which is only relevant for our more actively star-forming dwarfs. The FUV has been proven to be a reliable SF

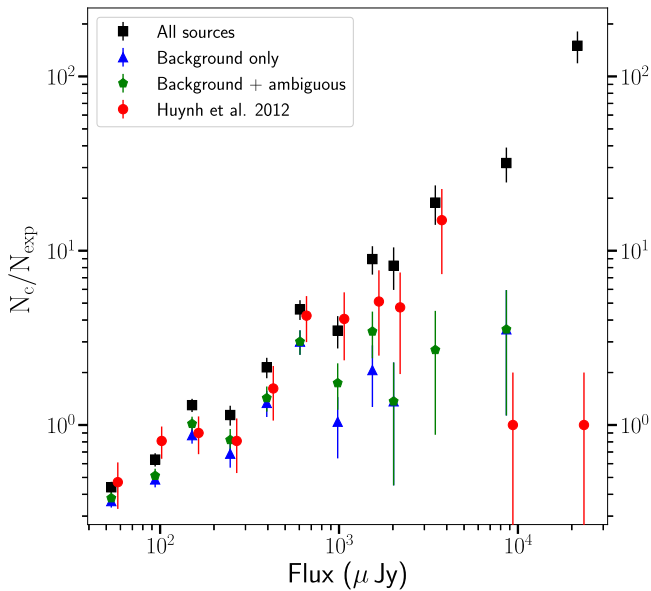


Figure 4. Corrected and normalized source counts recovered from our images. Sources are separated based on our source identification approach into all sources (black squares), background sources (blue triangles), and background and ambiguous sources (green pentagon). We compare these results to those of Huynh et al. (2012; red circles).

indicator at low SFR in comparison to $H\alpha$ -inferred SFRs (e.g., Lee et al. 2009; Ficut-Vicas 2016), and the timescale of RC_{Nth} emission is closer to the FUV-inferred SF timescales than to, e.g., the $H\alpha$ -inferred SF timescales. Galactic foreground extinction is taken into account separately (see Hunter et al. 2012 for details). To correct for internal extinction, Bigiel et al. (2008) and Leroy et al. (2012) use *Spitzer* 24 μm dust emission to empirically correct *GALEX* FUV fluxes for the fraction of dust-obscured SF on the assumption that a proportion of energy absorbed by internal dust is re-radiated at 24 μm (this is based on the original idea by Calzetti et al. 2007, who use $H\alpha$ instead of FUV). We use

$$\frac{\Sigma_{SFR}}{M_{\odot} \text{ yr}^{-1} \text{ kpc}^{-2}} = 0.081 \frac{I_{FUV}}{\text{MJy sr}^{-1}} + 0.0032 \frac{I_{24\mu m}}{\text{MJy sr}^{-1}}, \quad (3)$$

where the FUV and 24 μm intensity are in units of MJy sr^{-1} , and Σ_{SFR} represents the star formation rate density (SFRD). We show a map of the SFRD for DDO 50 in Figure 1. For those galaxies where *Spitzer* 24 μm data were not available (see Tables 3 and 4, column 7), we used the FUV-inferred SFR without any correction. Due to the low dust content of the majority of our sample, the FUV dominates the SFR estimates. The error associated with our SFR estimates is $\sim 20\%$. When compared to other methods of deriving the SFR, this approach was found to have a scatter of $\sim 50\%$ down to a Σ_{SFR} of $10^{-4} M_{\odot} \text{ yr}^{-1}$ (Leroy et al. 2012).

In Figure 5, we present the RC–SFR relation of our sample when considering the optical disk mask (top) and RC-based mask (bottom). We are able to determine the RC and SFR for 11 and 19 galaxies in the disk- and RC-based masks,

respectively. The left panels of Figure 5 show the relation when we include the ambiguous RC sources, whereas the right panels show the relation with ambiguous sources removed. If we do not remove the ambiguous sources, we find a significant flattening and increase in the scatter of the fit to the data particularly in the case of the RC-based mask results. The most likely cause for this is that these ambiguous sources are background radio galaxies. We therefore continue our analysis focusing only on the results where ambiguous sources are removed. In doing so, we may remove at most 10% of genuine RC emission in the form of SNRs as according to Chomiuk & Wilcots (2009), RC emission from SNRs contribute $< 10\%$ of the total RC in dwarf galaxies

The data points of our sample of galaxies in Figures 5–11 are color-coded based on the galaxy’s metallicity. This was done to investigate if there are any trends with metallicity. We find that in general the lowest metallicity objects congregate toward the low-radio continuum, low-SFR end of the plot whereas the high end is populated by the higher metallicity galaxies. This is a direct consequence of the metallicity–luminosity relation (Skillman et al. 1989) and the fact that more luminous, hence more massive, galaxies tend to have a higher SFR.

We compare our data points with the RC–SFR relation presented by Murphy et al. (2011). They derive an expression for the RC_{Th} and RC_{Nth} emission and combine these to determine the total RC in a galaxy. The thermal component is derived from the ionizing photon rate, which is directly proportional to the thermal spectral luminosity assuming an optically thin plasma, giving

$$\left(\frac{SFR_{\nu}^{Th}}{M_{\odot} \text{ yr}^{-1}} \right) = 4.6 \times 10^{-21} \left(\frac{T_e}{10^4 \text{ K}} \right)^{-0.45} \cdot \left(\frac{\nu}{\text{GHz}} \right)^{0.1} \left(\frac{L_{\nu}^{Th}}{\text{W Hz}^{-1}} \right), \quad (4)$$

where T_e is the electron temperature and L_{ν}^{Th} is the thermal radio luminosity. This equation assumes solar metallicity, continuous SF, and a Kroupa IMF. Using a Kroupa IMF results in SFR estimates that are ~ 2.5 times larger than those found by Condon (1992). We assume an electron temperature of 10^4 K . As mentioned previously, this value may vary considerably. A value of $T_e = 1.4 \times 10^4 \text{ K}$ (Nicholls et al. 2014) would lead to a 14% decrease in the SFR. The expected RC_{Nth} is derived using

$$\left(\frac{SFR_{\nu}^{Nth}}{M_{\odot} \text{ yr}^{-1}} \right) = 6.64 \times 10^{-22} \left(\frac{\nu}{\text{GHz}} \right)^{\alpha_{Nth}} \cdot \left(\frac{L_{\nu}^{Nth}}{\text{W Hz}^{-1}} \right). \quad (5)$$

This relationship is derived using the STARBURST99 population synthesis code (Leitherer et al. 1999) and the empirical relationship between the supernova rate and nonthermal spectral luminosity of the Milky Way. We assume a value for the nonthermal spectral index of $\alpha_{Nth} = -0.7 \pm 0.2$. Finally, the total RC is the combination of RC_{Th} and RC_{Nth} ,

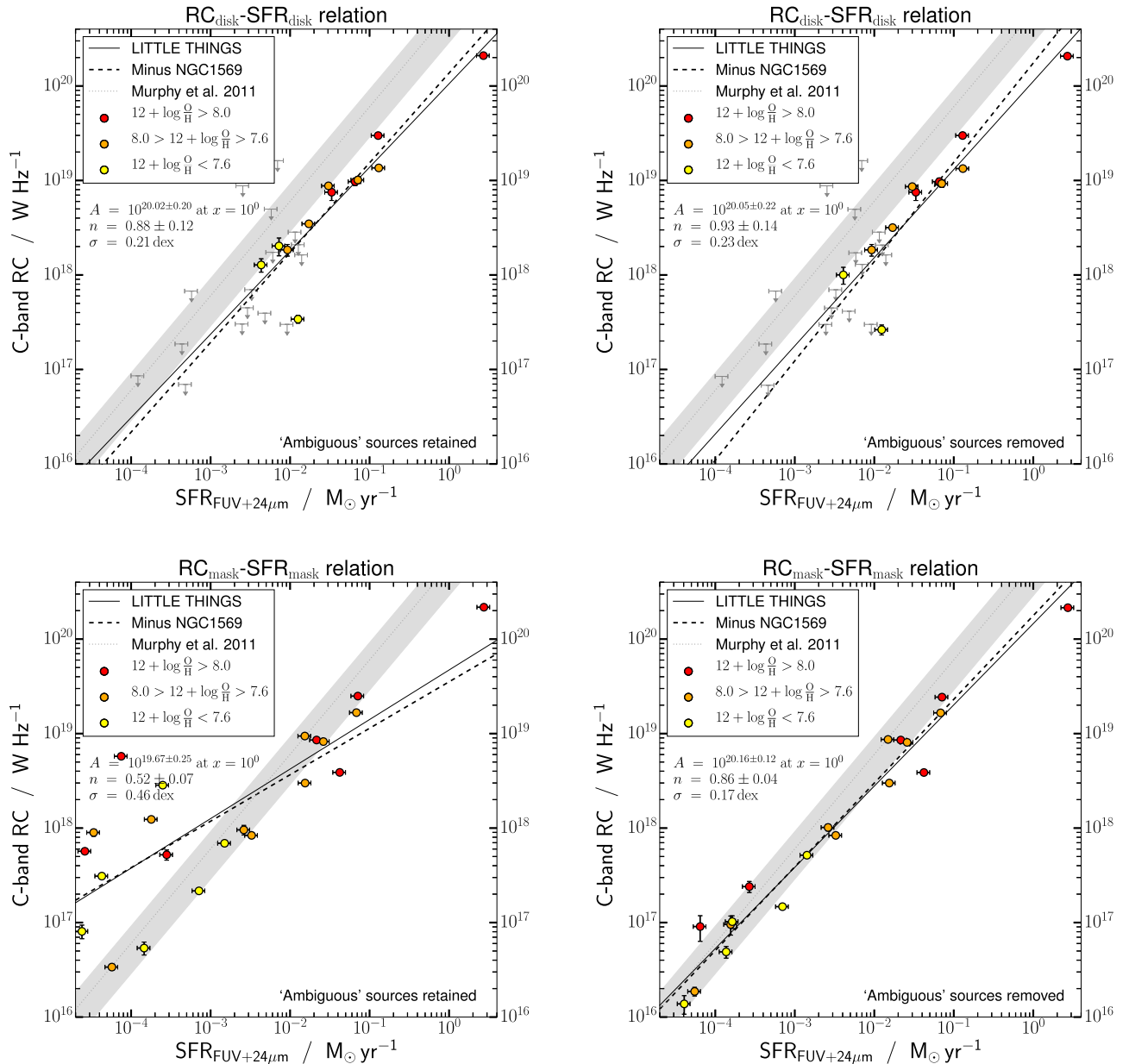


Figure 5. Total 6 cm luminosity as a function of SFR over our disk (top panels) and RC (bottom panels) masks. Definite background sources have been removed, while the ambiguous sources have been retained (left) and removed (right). The solid line is the best-fit power law to our sample. For reference, we show the Murphy et al. (2011) RC–SFR relation as a shaded gray band. The errors introduced by our conversion are reflected by the gray shaded band, and the 3σ upper limits of RC emission are shown by gray arrows.

leading to

$$\left(\frac{\text{SFR}_\nu}{M_\odot \text{ yr}^{-1}}\right) = 10^{-20} \left[2.18 \left(\frac{T_e}{10^4 \text{ K}}\right)^{-0.45} \times \left(\frac{\nu}{\text{GHz}}\right)^{0.1} + 15.1 \left(\frac{\nu}{\text{GHz}}\right)^{\alpha_{\text{NH}}} \right] \left(\frac{L_\nu}{\text{W Hz}^{-1}}\right), \quad (6)$$

where we use a frequency ν of 6.2 GHz. These expected relations are plotted as the gray shaded area in Figure 5. The width of the band reflects the overall uncertainty based on a typical error in the spectral index of 0.2 and a canonical factor of 2 uncertainty in the SFR.

We performed a bivariate linear regression to quantify the relation between the RC luminosity and SFR, assuming the data follow a power-law function of the form $y = Ax^n$ or $\log(y) = n \log(x) + c$, where $c = \log(A)$. We used the ODR¹² module from SCIPY, which accepts four arrays of data points ($\log x$ and $\log y$, and the 1σ errors in log-space: $\frac{\delta x}{x}$ and $\frac{\delta y}{y}$) and the model function, and works to minimize the squares of the orthogonal distance between the data points and the model, ultimately returning best-fit values and their standard deviations.

We find that the disk mask RC–SFR relation (Figure 5 top-right panel) results are consistent with a linear relationship with

¹² http://www.scipy.org/doc/api_docs/SciPy.odr.odrpack.html

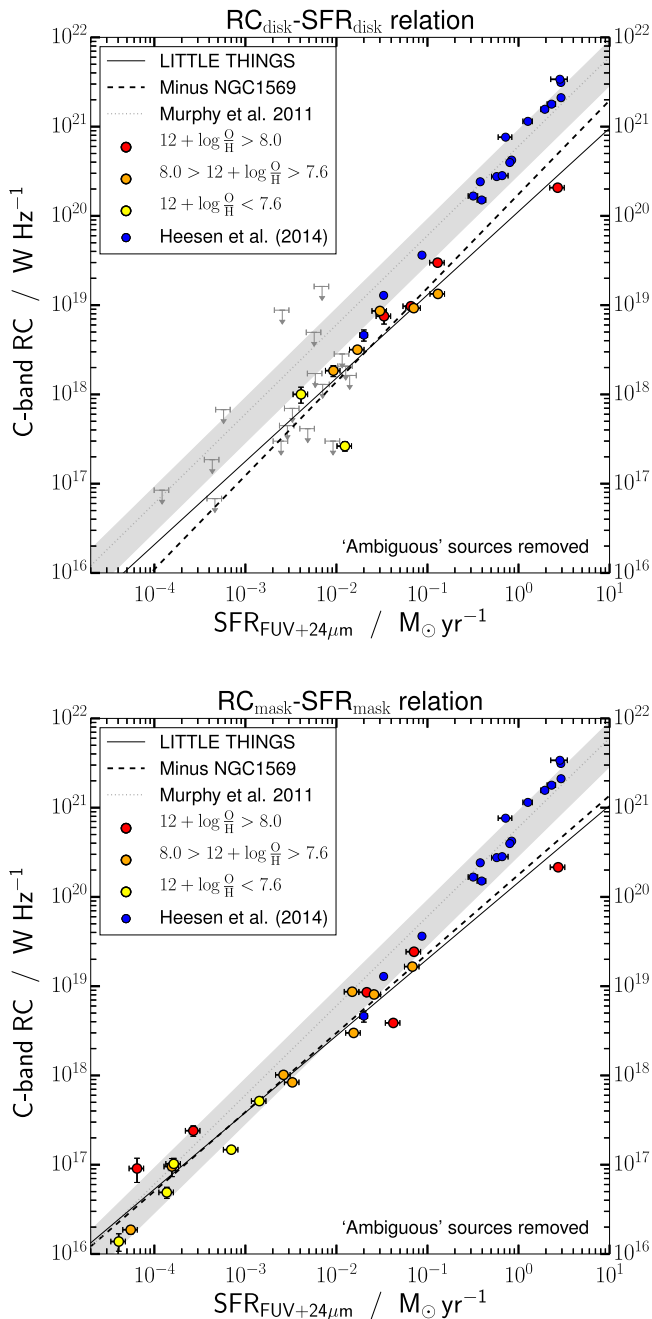


Figure 6. Comparison of our disk-integrated (top) and mask-integrated (bottom) RC and SFR properties with those of Heesen et al. (2014; blue points). Obvious background and ambiguous sources were removed. The WSRT 22 cm data were corrected to 6 GHz assuming a spectral index of -0.7 . The LITTLE THINGS galaxies have been colored according to their metallicity. The solid black line is the best-fit power law to the LITTLE THINGS sample, while the shaded band shows the Murphy et al. (2011) relation. The dashed black line shows the fit excluding NGC 1569.

$n = 0.93 \pm 0.14$, but the RC luminosity is lower than expected based on the observed SFR by approximately a factor of ~ 5 . We note that IC 1613 falls below the relation we find. If we exclude this galaxy, we find that the average offset is a factor of ~ 3 . We find that the RC mask-integrated RC–SFR relation in Figure 5 (bottom-right panel), where the RC mask is applied to both the RC and the SFR map, is marginally shallower than the

Murphy et al. (2011) relation with a gradient of $n = 0.86 \pm 0.04$ with a scatter of 0.17 dex. If we perform the fit excluding NGC 1569 (Figure 5, dashed black line), we find a value of $n = 0.91 \pm 0.04$. In Figure 6, we compare the results of our disk-integrated and mask-integrated RC–SFR relation to the study of 18 spiral galaxies at 20 cm by Heesen et al. (2014). We extend their parameter space by 2 dex, down to SFRs of $10^{-4} M_{\odot} \text{yr}^{-1}$. At 20 cm, the Heesen et al. (2014) study found a slope of the RC–SFR relation of $n = 1.24 \pm 0.04$, which is significantly steeper than our results.

The relationship between the RC_{Th} and RC_{Nth} emission and SFR integrated over the disk and RC mask is shown in Figure 7. When integrating the two components over the optical disk mask, we find slopes of $n = 1.20 \pm 0.09$ and $n = 0.82 \pm 0.06$ for RC_{Th} and RC_{Nth} , respectively. We find a slope of $n = 0.82 \pm 0.05$ and $n = 0.79 \pm 0.06$ for RC_{Th} and RC_{Nth} emission integrated over the RC mask, respectively. If we exclude NGC 1569 from the fit, we find marginally steeper slopes. Our results for RC_{Th} agree with those of Murphy et al. (2011) when integrating over the RC mask but appear to diverge at the low-SFR levels ($< 10^{-2} M_{\odot} \text{yr}^{-1}$) in the disk mask. This may be due to the stochastic nature of SF particularly in the faintest galaxies. It is important to note that the RC_{Th} plot is essentially an $\text{H}\alpha$ –FUV plot. The RC_{Th} values are based on the $\text{H}\alpha$ emission and are thus not independently determined; in turn, the SFR relies heavily on the FUV. The scatter, especially for the least active dwarf galaxies ($\text{SFR} \lesssim 10^{-2} M_{\odot} \text{yr}^{-1}$), is likely due to the $\text{H}\alpha$ emission underestimating the SFR in comparison to that from the FUV by a factor of up to 10 (Lee et al. 2009). These authors argue that as only the highest mass stars ($M \gtrsim 18 M_{\odot}$) produce a significant number of photons to ionize the surrounding H I, having a deficit of these stars significantly reduces the amount of $\text{H}\alpha$ emission, while the FUV emission is not affected as much since a larger fraction of the stellar population contributes to the FUV. On the other hand, Koda et al. (2012) find O stars in stellar clusters as small as 100–1000 M_{\odot} , coming to the conclusion that the stellar IMF is not necessarily truncated; it could be stochastically populated at the high-mass end, accounting for the observed variations in Figure 7. We discuss this further in Section 4.6.

The RC_{Nth} results are shallower than expected based on the predictions of Murphy et al. (2011) in both masking cases. Not only is the slope shallower, we also see that when using the disk mask the RC_{Nth} emission falls below the expected SFR by a factor of 2–4. This agrees with Bell (2003), who found that the radio emission of low-luminosity galaxies must be suppressed by at least a factor of two to account for the RC–FIR relation at low luminosity. Our results also agree with the findings of Price & Duric (1992), who found that the power-law dependence of the synchrotron luminosities and SFR has a slope of $n = 0.8$. Using the same method applied here but observing at 20 cm, Heesen et al. (2014) found a slope of the RC_{Nth} component for spiral galaxies to be $n = 1.16 \pm 0.08$, significantly steeper than our results (Figure 6). We note that the RC_{Nth} may be underestimated particularly for large-scale galaxies that have high SFRs such as NGC 1569. This would lead to the RC_{Nth} –SFR relation being steeper than what we see in Figure 7. However, when we remove NGC 1569 from our

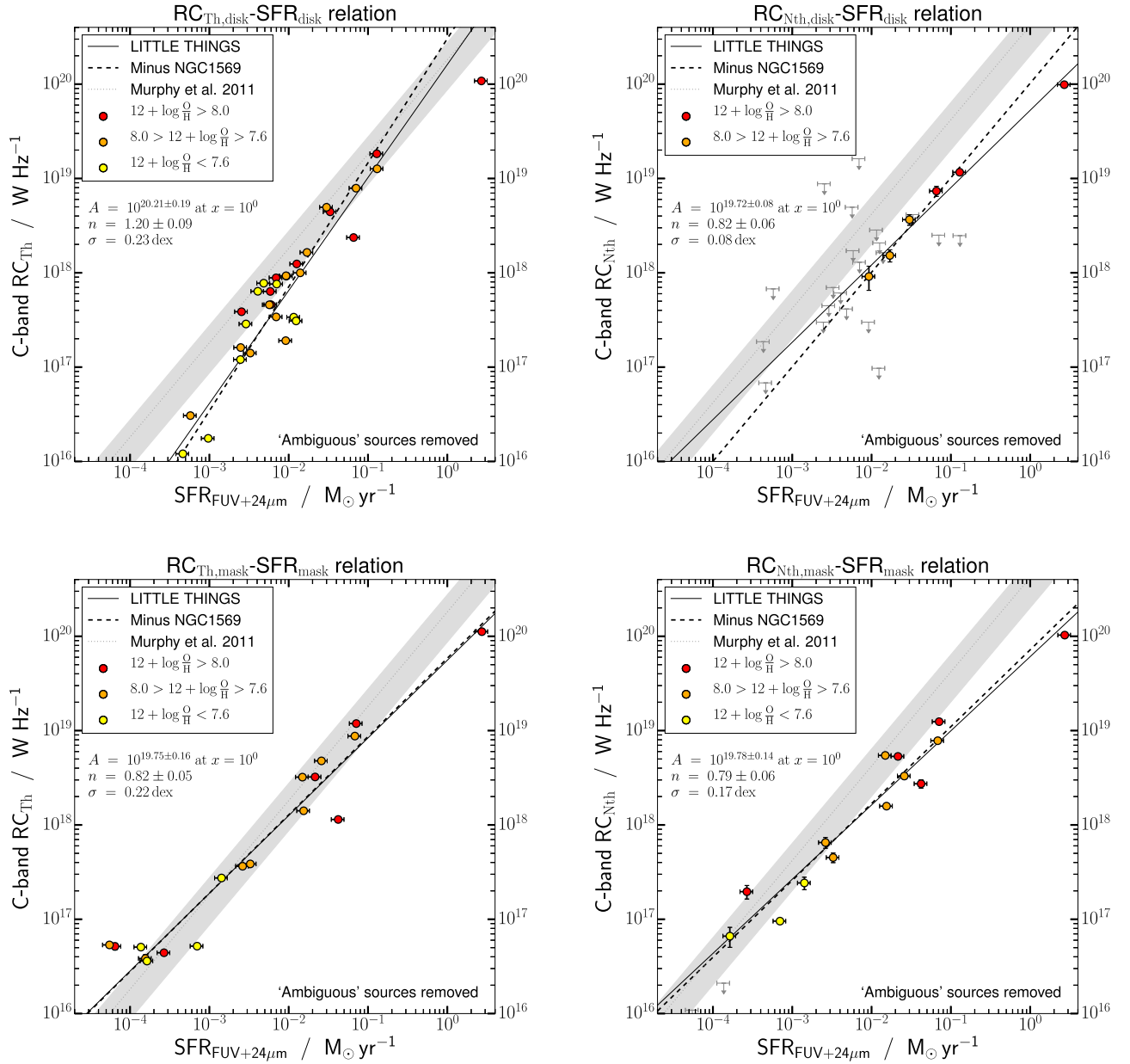


Figure 7. Total 6 cm RC_{Th} (left) and RC_{Nth} (right) luminosity as a function of SFR integrated over our disk (top) and RC mask (bottom). Both definite background sources and ambiguous sources have been removed. The solid line is the best-fit power law to our sample. We show the Murphy et al. (2011) RC_{Th}-SFR and RC_{Nth}-SFR relations for reference as a shaded gray band; the 3σ upper limits of the RC emission are shown by the gray symbols with downward arrows.

fitting, our results remain consistent with those with NGC 1569 included.

The RC surface-brightness–SFRD relation is presented in Figure 8, where the SFRD is derived over the extent of the galaxy. We find a tight, linear RC–SFRD relation with a slope of $n = 0.99 \pm 0.11$ and $n = 0.88 \pm 0.02$ for the disk- and RC-based masks, respectively. Within the errors, these slopes are the same as those found for the relations plotted in Figure 5. Unlike the luminosity plots in Figure 5 though, this is independent of the distance and so errors introduced by distance uncertainties forcing a linear relation due to flux-to-luminosity scaling are avoided. Figure 8 could thus be used as a baseline for future studies of normal star-forming galaxies—especially those studies that do not have reliable distance

measurements (e.g., only photometric redshifts of optical counterparts).

4.3. The FIR–SFR Relation

The FIR is often used as a proxy for SFR in studies of unresolved galaxies. It is therefore instructive to examine the relationship between the FIR and SFR integrated within the disk and RC masks in Figure 9 of our sample. We compare our estimate to the monochromatic $70 \mu\text{m}$ calibration of Calzetti et al. (2010) using

$$\left(\frac{\text{SFR}_{70\mu\text{m}}}{M_{\odot} \text{yr}^{-1}} \right) = \left(\frac{L_{70\mu\text{m}}}{\text{W Hz}^{-1}} \right) \cdot 2.52 \times 10^{-24}, \quad (7)$$

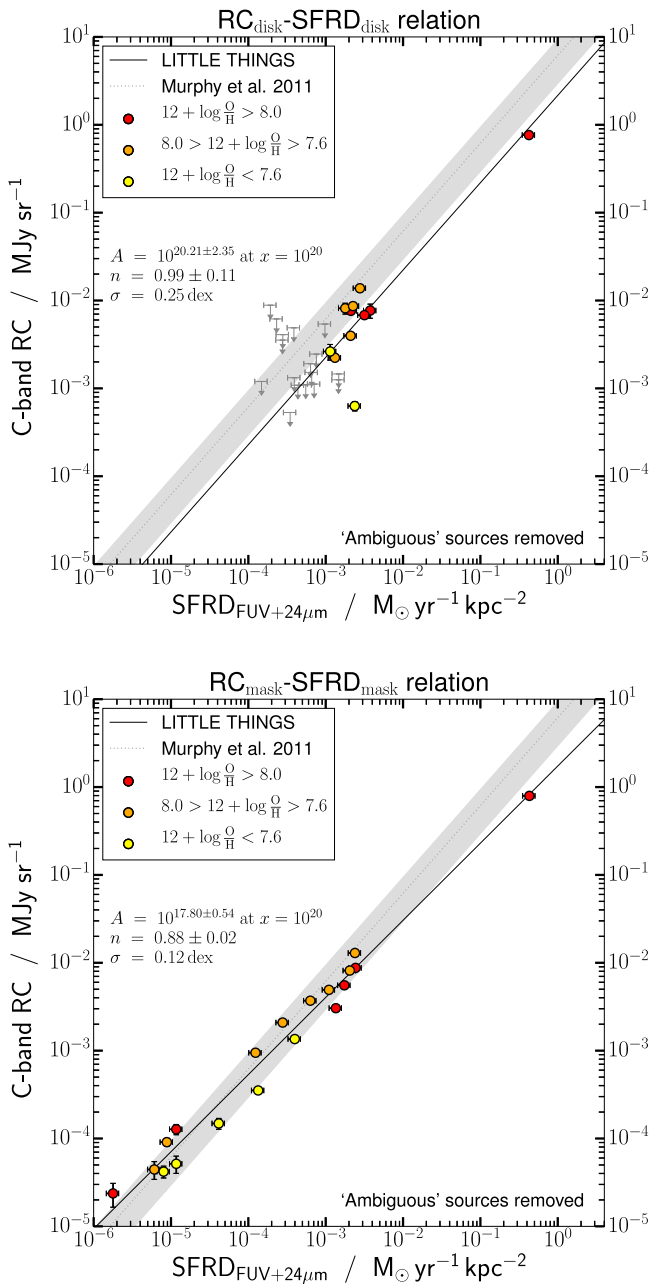


Figure 8. Galaxy-wide total 6 cm surface brightness as a function of the FUV-inferred SFRD corrected for internal extinction from dust based on their 24 μm emission. Background and ambiguous sources have been removed. The solid line is the best-fit power law to our sample. We show the predicted Murphy et al. (2011) RC–SFR relation for reference as a shaded gray band; the 3σ upper limits of the RC emission are shown by the gray symbols with downward arrows.

where $L_{70\mu\text{m}}$ is the 70 μm luminosity in W Hz^{-1} . We find that our best-fit line is the same within the errors for both the disk- and RC-based masks ($n = 1.07 \pm 0.09$ and 1.05 ± 0.06 , respectively) and runs parallel to the Calzetti et al. (2010) relationship. However, for any given SFR, we find that our measurement of the integrated 70 μm emissions is underestimated compared to the expected 70 μm luminosity by a factor of ~ 10 . Given the fact that dwarf galaxies have low metallicity, this is not surprising. The metallicity of all our galaxies falls below a value of $12 + \log(\text{O}/\text{H}) \sim 8.1$, below

which Calzetti et al. (2010) found the FIR to be an unreliable tracer of the SFR. At these low metallicities, the galaxies become basically optically thin, and FUV photons can escape before being reprocessed by dust and re-emitted in the FIR. This was also suggested as the cause of the ratio between the total IR and FUV being < 1 in low-luminosity galaxies in a study by Bell (2003).

4.4. The RC–FIR Relation

The RC–FIR relation based on 1809 galaxies culled from the NRAO VLA Sky Survey (NVSS; Condon et al. 1998) catalog and the 1.2 Jy IRAS Redshift Survey catalog (Strauss et al. 1992) was investigated by Yun et al. (2001). They related the integrated 1.4 GHz RC of an unresolved galaxy to the IRAS 60 μm luminosity and found

$$\frac{L_{6\text{GHz}}}{\text{W Hz}^{-1}} = (2.24 \pm 0.67) \times 10^{-3} \left(\frac{L_{70\mu\text{m}}}{\text{W Hz}^{-1}} \right)^{0.99}, \quad (8)$$

where we converted the IRAS 60 μm luminosity to a “luminosity density” (i.e., from W to W Hz^{-1}) by noting that the response from the IRAS 60 μm filter is equivalent to a perfectly transmitting filter with a bandwidth of 2.6×10^{12} Hz. The IRAS 60 μm “luminosity density” was further converted to the equivalent *Spitzer* 70 μm luminosity by scaling it up by a factor of 1.27. This value is based on a graybody model for dust emission with $\beta = 1.82$ and $T_{\text{dust}} = 35$ K; this assumes that the Yun et al. (2001) galaxies are in a quiescent mode of star formation, and that there is no significant emission from warm dust. The Yun et al. (2001) VLA 1.4 GHz RC data were reduced by a factor of 2.83 to derive predicted equivalent VLA 6 GHz flux densities assuming a constant spectral index of -0.7 ± 0.2 between 20 and 6 cm for the galaxies in their sample.

In Figure 10, we show the RC–FIR relation for our dwarf galaxies and compare this to the results of Yun et al. (2001). The RC–FIR relation traditionally samples the parameter space above FIR luminosities of $\sim 10^{22}$ W Hz^{-1} ; we extend this to lower luminosities by 3 dex. The uncertainty presented in Figure 10 takes into account an uncertainty in the spectral index of 0.2 and 15 K in dust temperature. We show the RC–FIR relation for our dwarf sample where emission is integrated over the entire disk (Figure 10, left) and from regions of significant RC emission only (i.e., the RC-based mask; Figure 10, right). In Figure 11, we show the RC–FIR relation for just our dwarf galaxy sample integrated over the disk mask (left) and RC mask (right). The top panels of this figure show the luminosity and the bottom panels the flux density to illustrate any dependence on distance. We find that when integrated over the disk, our results for the luminosity match those found by Yun et al. (2001) with a slope of 1.02 ± 0.10 . The flux density derived slope is slightly shallower at 0.87 ± 0.07 . However, when we integrate the RC and 70 μm emission using our RC mask, we find that our results diverge from the Yun et al. (2001) relation in both the luminosity and flux density plots with a flatter slope of 0.81 ± 0.03 and 0.80 ± 0.03 for the luminosity and flux density, respectively. We discuss the possible reasons behind this in Section 4.6.

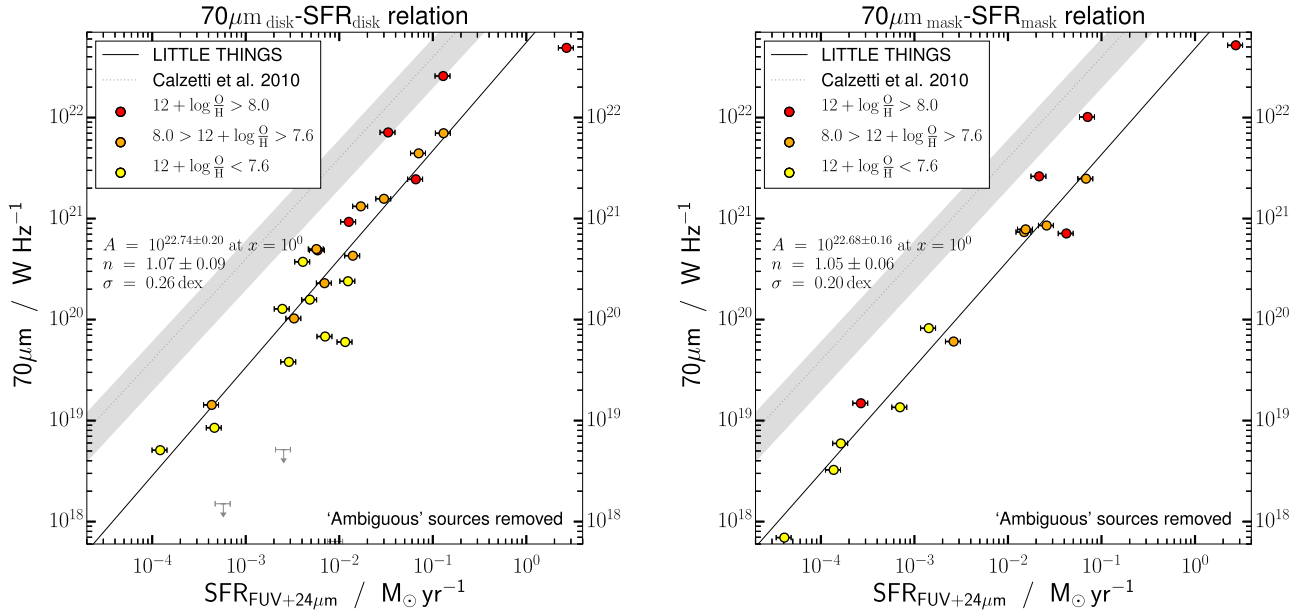


Figure 9. Total $70 \mu\text{m}$ luminosity as a function of SFR over our disk and RC masks. The solid line is the best-fit power law to our sample. For reference, we show the Calzetti et al. (2010) $70 \mu\text{m}$ –SFR relation assuming a factor of two uncertainty (shaded gray band). Upper limits of the $70 \mu\text{m}$ emission are shown as gray symbols with downward arrows.

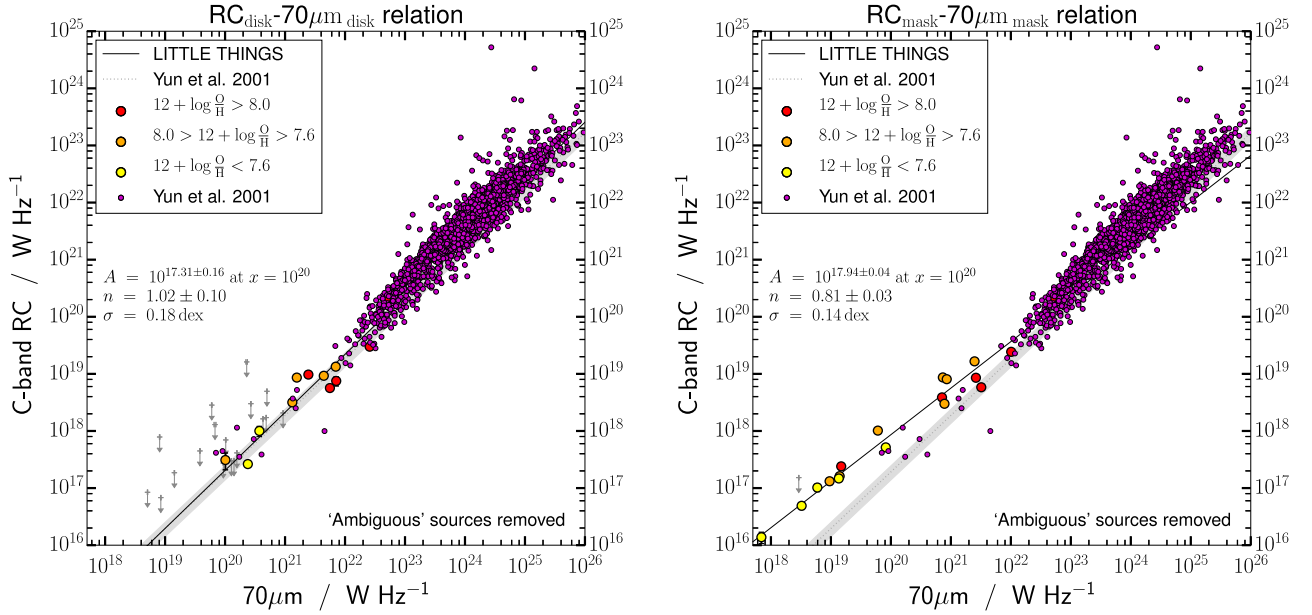


Figure 10. Comparison of the RC and FIR luminosities from this study to those from Yun et al. (2001); their VLA 1.4 GHz data have been extrapolated to 6 GHz and the *IRAS* $60 \mu\text{m}$ data corrected to *Spitzer* $70 \mu\text{m}$. Both definite background and ambiguous RC sources have been removed from the LITTLE THINGS galaxies. Integrated quantities were taken from regions of significant RC emission (i.e., the RC-based mask; right panel) and from over the whole optically defined disk (left). The LITTLE THINGS galaxies that remain undetected are represented by their 3σ upper limits (gray plus symbols with downward arrow). The uncertainties introduced by our conversion of the relation found by Yun et al. (2001) are reflected by the gray shaded band (see the text for details).

4.5. q Parameter

An alternative way of exploring the RC–FIR relation described by Yun et al. (2001) is through the q parameter. This is the natural logarithm of the ratio of the *IRAS* FIR (a weighted combination of 60 and $100 \mu\text{m}$ flux) to the VLA 1.4 GHz flux densities of the Yun et al. (2001) sample and is

described by

$$q_{\text{FIR:1.4}} = \log \left(\frac{\text{FIR [Jy]}}{\text{RC [Jy]}} \right). \quad (9)$$

The average $q_{\text{FIR:1.4}}$ parameter was found to be 2.34 ± 0.01 . Since our RC and FIR measurements were made in different

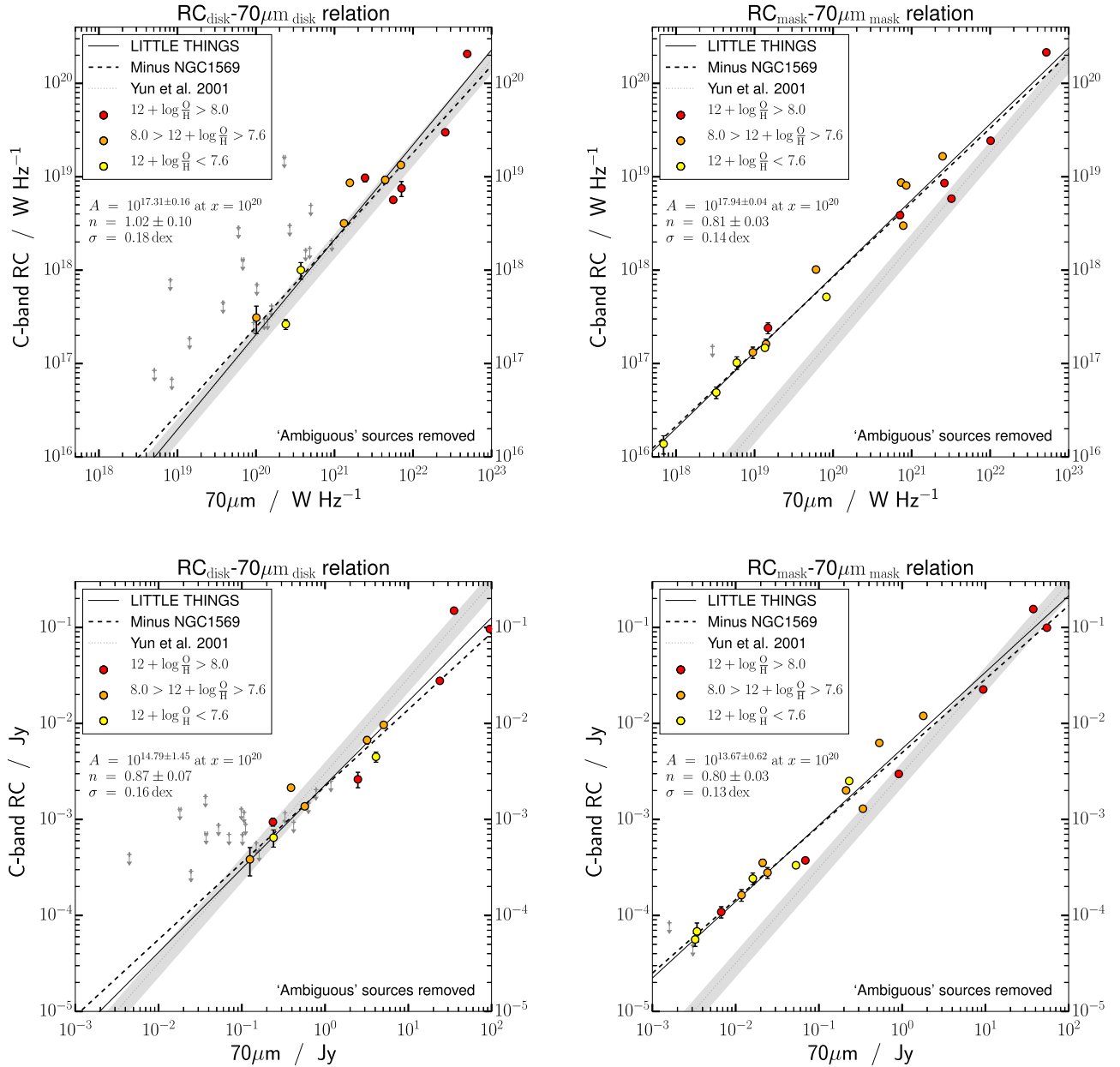


Figure 11. 6 cm luminosity as a function of the *Spitzer* $70\mu\text{m}$ FIR integrated over the disk mask (left) and RC mask (right). The top panels show the luminosity relation while the bottom panels have not been corrected for the distance and show the flux density. Definite and ambiguous background sources have been removed. The solid line is the best-fit power law to our sample. We draw the Yun et al. (2001) RC–FIR relation as described in Equation (8) (dotted line). The uncertainties introduced by our conversion are reflected by the gray shaded band (see text for details). The LITTLE THINGS galaxies that remain undetected are represented by their 3σ upper limits (gray plus symbols with downward arrow).

bands from those used by Yun et al. (2001), we convert their $q_{\text{FIR:1.4}}$ to $q_{70:6} = 2.68 \pm 0.12$, where the subscripts 70 and 6 refer to the $70\mu\text{m}$ FIR and 6 GHz RC, respectively. As before, the uncertainty is calculated by assuming a 0.2 uncertainty in the spectral index between 20 and 6 cm, and a 15 K uncertainty in dust temperature.

We plot $q_{70:6}$ values as a function of $70\mu\text{m}$ FIR luminosity in Figure 12. The LITTLE THINGS dwarfs are consistent with the Yun et al. (2001) sample when integrated over the disk (Figure 12; left). This reveals that the RC–FIR “conspiracy” continues in our dwarf galaxy sample. However, we see in the right panel of Figure 12 that when we integrate the emission over

the RC mask there is a considerable excess of RC emission compared to $70\mu\text{m}$ for sources that have a low radio luminosity, as was already evident in Figures 10 and 11 (right-hand panels).

4.6. The Interplay Between SF, RC, and FIR

The relationship between the RC, FIR, and SFR can be summarized by three equations. The RC–SFR and FUV–SFR relations can be expressed as

$$\frac{L_{\text{RC}}}{\text{W Hz}^{-1}} = 10^A \left(\frac{\text{SFR}}{M_{\odot} \text{ yr}^{-1}} \right)^n \quad (10)$$

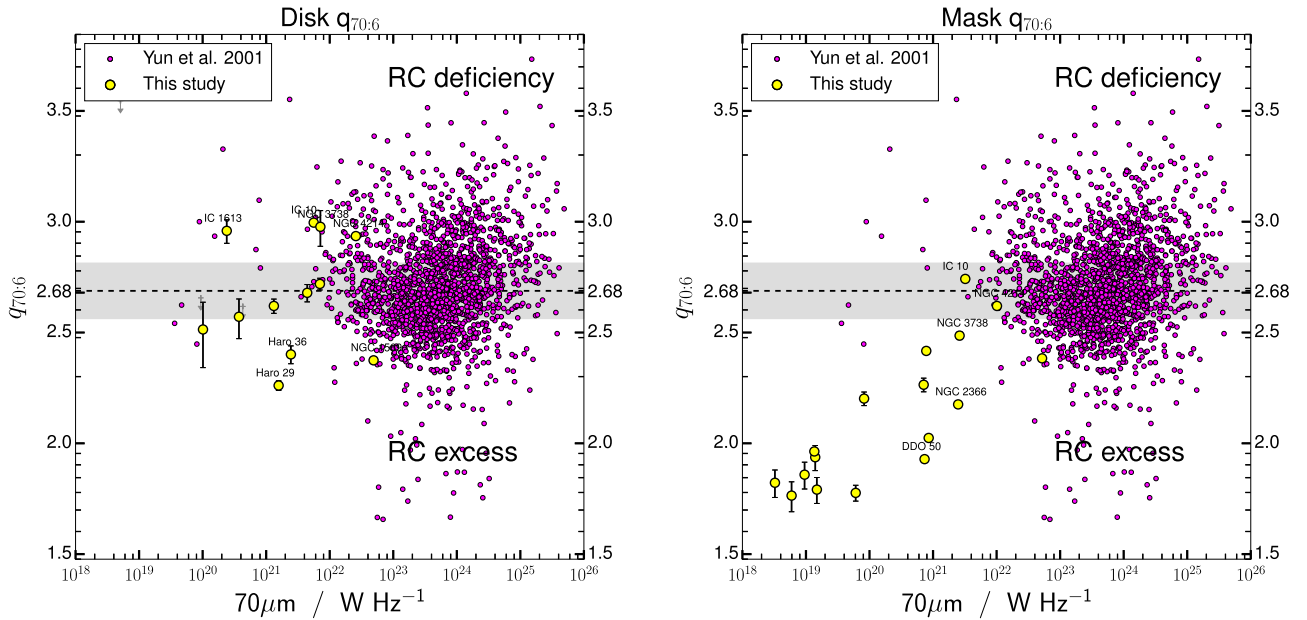


Figure 12. $q_{70:6}$ parameter as a function of $70 \mu\text{m}$ luminosity. Both obvious and ambiguous background sources have been removed. We also show the Yun et al. (2001) data points (purple) and their q parameter appropriately corrected to our observing bands (dashed line). The errors introduced by our conversion are reflected by the gray shaded band.

and

$$\frac{L_{\text{FIR}}}{\text{W Hz}^{-1}} = 10^A \left(\frac{\text{SFR}}{M_{\odot} \text{ yr}^{-1}} \right)^n, \quad (11)$$

while the RC–FIR relation can be described by

$$\frac{\text{RC}}{\text{W Hz}^{-1}} = 10^A \left(\frac{70 \mu\text{m FIR}}{10^{20} \text{ W Hz}^{-1}} \right)^n. \quad (12)$$

We summarize the results for the various fits for these relations over the disk and RC masks in Table 6.

We use the Pearson (P) and Spearman (S) coefficients to describe the strength and direction of the correlation in our relationships, where a value of -1.0 indicates a strong anti-correlation, 0.0 indicates the relationship is random or non-existent, and $+1.0$ indicates a strong, positive correlation. The Pearson coefficient assumes a purely linear relationship and so will approach 0.0 if there is an inconsistent relationship while the Spearman coefficient evaluates the monotonic relationship between two variables and so will remain high. Thus, a strong relationship that deviates from linearity will have a lower Pearson than Spearman score. Both the Pearson and Spearman coefficients indicate a strong correlation between all components of the RC and SFR, with values ranging from 0.77 to 1.00 depending on the relation and type of mask used.

The fitted parameters for A and n for each relation in Table 6 vary significantly based on the type of mask used except in the case of the FIR–SFR relation. The FIR–SFR relation has lower Pearson and Spearman scores compared to the RC-based relations, suggesting a weaker relationship and deviation from linearity and showing a larger scatter. Since the RC-based mask is able to probe significantly lower SFR galaxies, this suggests that the physical processes responsible for the FIR–SFR relation operate in the same way regardless of the level of SFR in our sample. The varying parameters that fit the various RC–SFR relations in the disk and RC masks indicate that there may be some change in the physical processes operating within

regions on the scale of the entire disk and resolved scales traced by the RC-based masks.

One of the most striking results of this study is the divergence we see in the RC–FIR relation at low luminosities when integrating over the RC mask (Figure 11, right). This appears to be caused by the FIR emission being underestimated in the RC mask relative to the expected Calzetti et al. (2010) SFR (Figure 9), whereas the RC emission continues to follow the SFR down to low values (Figure 5). Our disk-masked results on the other hand underestimate both the RC and FIR luminosity compared to the predicted SFR, leading to the linear slope that continues the RC–FIR “conspiracy” seen in the left panel of Figure 11. In the case of RC emission excess, we find evidence that it is the RC_{Nth} component that is responsible for the suppression of the RC on the scale of the disk (Figure 7).

We propose two possible scenarios that may be responsible for the relations we observe. The first is that dwarf galaxies do not act as calorimeters, and CR_e and dust-heating photons are able to escape the galaxy before they are able to generate the total RC_{Nth} and FIR emission associated with their host SF. The second possibility is that we are witnessing the effect of stochastic SF resulting in a partially sampled and/or truncated IMF. This may lead to the RC_{Nth} and FIR underestimating the SFR compared to studies of larger galaxies. It is possible that some combination of these scenarios is responsible for our results.

4.6.1. Calorimeter Breakdown

Given their low metallicity and dust content, it is possible that the mean free path of dust-heating photons is less than the galaxy scale height. This would mean that dust-heating photons are not completely absorbed and re-radiated into the FIR and instead escape the galaxy. This would result in the observed suppression of the FIR relative to the expected SFR from Calzetti et al. (2010) in both the RC and disk mask. Given the low optical depth of dwarf galaxies (Bell 2003), this is one plausible explanation for our observed FIR–SFR relation.

The low gravitational potential wells of dwarf galaxies make them particularly susceptible to outflows where material including CRe can escape the galaxy. In addition, CRe may diffuse out of the galaxy before they are able to emit all of their radiation if the magnetic field strength is low. Both these processes would lead to a suppression of the RC_{Nth} emission relative to the SFR (Figure 7, right). The RC_{Th} emission is expected to be consistent with theoretical predictions because it is directly associated with ongoing massive star formation (Murphy et al. 2011). This indeed seems to be the case in our study, except at low SFRs of $<10^{-2} M_{\odot} \text{yr}^{-1}$, where we see evidence of suppression and an increased scatter of RC_{Th} (and therefore $\text{H}\alpha$) relative to the SFR. The suppression of the RC_{Nth} emission relative to the expected SFR is only observed in our results when integrated over the disk mask. This may suggest that on the scales of concentrated SF traced by our RC mask, magnetic fields are strong enough to act as a local calorimeter. Therefore, CRe expend their energy and age to lower frequencies before they have a chance to diffuse into the wider ISM. We explore this possibility further in Section 4.7.

4.6.2. Stochastic Star Formation

An alternative explanation for our observed trends in the RC, FIR, and SFR could be due to the effects of stochastic SF within our dwarf galaxy sample. Synthesis models used to calibrate SFR indicators assume a sufficient number of stars to fully populate the IMF. In the case of dwarf galaxies with low SFRs, the short lived high-mass stars may be underrepresented, invalidating this assumption. Simulations of dwarf galaxies undergoing stochastic SF have found that FUV-inferred SFRs may be biased at the ~ 0.5 dex level for SFRs of $\sim 10^{-4} M_{\odot} \text{yr}^{-1}$ (da Silva et al. 2012a, 2012b). Moderate variations in the SFR have also been observed in the star formation histories of nearby dwarf galaxies (Dohm-Palmer et al. (1998; Weisz et al. 2008). We would also expect stochasticity to impact the generation of the FIR, RC, and $\text{H}\alpha$ emission because these are all sensitive to the high-mass end of the IMF. These effects will have complicated spatial and temporal dependencies that vary for each type of emission mechanism. If the high-mass end of the IMF is underpopulated, we would expect $\text{H}\alpha$ emission to be suppressed or even absent (Lee et al. 2009), resulting in an increase in scatter around SFRs of $10^{-2} M_{\odot} \text{yr}^{-1}$ and a suppression of the $\text{H}\alpha$ emission below $10^{-3} M_{\odot} \text{yr}^{-1}$. We see this behavior in our RC_{Th} -SFR relation in the disk mask results (Figure 7, top left). This agrees with the simple calculation of Lee et al. (2009), who find that the $\text{H}\alpha$ flux is only a robust tracer of SFR above $1.4 \times 10^{-3} M_{\odot} \text{yr}^{-1}$. However, Lee et al. (2009) argue that the stochastic SF alone is not sufficient to explain the suppression of $\text{H}\alpha$ emission. In any case, the suppression of the RC and FIR we see in our disk masks is evident at SFRs greater than $10^{-2} M_{\odot} \text{yr}^{-1}$.

From our current data set, it is unclear which of the scenarios we discuss above is responsible for our observed relations. Further work is required to investigate the impact of stochastic SF and a possible breakdown of the calorimeter model in these galaxies and the impact on our RC, FIR, and SFR measurements. In order to establish the origin of the observed suppression of the RC relative to SFR, we require further information on the spectral and spatial variation of the RC-SFR relation in these galaxies so that we can explore the effects of cosmic-ray aging and transport (Heesen et al.

2016). In order to explore the impact of stochastic SF, we require detailed Monte Carlo simulations of the underlying stellar populations or observations of the resolved stellar populations.

4.7. Cosmic-ray Electrons and Magnetic Fields

Our results suggest that it is the suppression of the RC_{Nth} emission that is responsible for the RC-FIR relation remaining consistent at low SFRs. To explore the source of the RC_{Nth} emission, we investigate the synchrotron emissivity in an optically thin region,

$$\epsilon_{\text{Nth}} \propto n_{\text{CR}} B_{\perp}^{\frac{\gamma+1}{2}}, \quad (13)$$

where n_{CR} is the number density of CRe present in the dwarf's galactic magnetic field, B_{\perp} is the strength of the transverse magnetic field, and γ is the power-law slope of the CRe injection spectrum.

The RC_{Nth} emission depends both on the energy density contained within the magnetic field and that of the population of CRe. The combined energy density associated with the magnetic field and CRe is usually assumed to be at a minimum (see Section 16.5 of Longair 1981). In galaxies, this is a reasonable assumption. If the energy densities are not equal, they will tend to balance: for example, if the energy density is dominated by the CRe, then they will rise out of the galactic disk in Parker lobes due to their buoyancy, expand, and escape, thus reducing their energy density until it is balanced with that in the magnetic field.

It is, however, conceivable that dwarf galaxies in particular deviate from equipartition. This would lead to a reduction in synchrotron emission (see Figure 7) in two different ways:

- (1) a low number density of CRe (n_{CR}) present in the dwarf's galactic magnetic field. Dwarf galaxies in particular are prone to galactic outflows since they have low masses and correspondingly shallow gravitational potentials, and winds can advect plasma and resident CRe away from the galaxy;
- (2) the magnetic field strength (B) being lower than the equipartition value at which the energy density of the magnetic field is equal to that of the cosmic rays (electrons and protons combined). In the standard paradigm of a mean field α - Ω dynamo, the key ingredients are turbulence and shear. Dwarf galaxies may be sites of weak, large-scale, ordered magnetic fields, so magnetic field amplification may be less efficient. Studies by Chyży et al. (2011) and Roychowdhury & Chengalur (2012) found global magnetic field strengths on the order of $<5 \mu\text{G}$ toward dwarf galaxies. However, the turbulent field in and around the SF regions may not necessarily be weaker than that found in spirals (e.g., Tabatabaei et al. 2013) as $30 \mu\text{G}$ is observed across some 100 pc regions.

In the following, the magnetic field strength in our sample of dwarf galaxies is estimated under the assumption of equipartition; this is the only practical way of estimating the field strengths given our current data set. We apply the equipartition formula for the total magnetic field following Equation (3) from Beck & Krause (2005). We made the standard assumptions of a spectral index of -0.7 ± 0.2 , proton-to-electron number density ratio K of 100 ± 50

(Beck & Krause 2005; Murphy et al. 2011), and that the dwarf galaxy has a scale height of 400 ± 200 pc independent of distance from the galaxy center (Banerjee et al. 2011; Elmegreen & Hunter 2015). We note that these assumptions are prone to significant uncertainty. The value of K depends on the acceleration process, propagation, and energy losses of the protons and electrons. As CRe propagate away from their sites of acceleration, they rapidly lose energy, leading to values of $K > 100$. If this is the case in our dwarf galaxies and if CRe are escaping the galaxy, altogether this will lead to an underestimate of the equipartition magnetic field. The scale height of dwarf galaxies is also prone to large variations due to their low mass and the potential for outflows. Typical scale heights have values ranging from 200–400 pc in the inner regions and 600–1000 pc in the outer regions.

The average transverse magnetic field strength of our sample is $5.2 \pm 2.6 \mu\text{G}$ and $7.5 \pm 3.3 \mu\text{G}$ when integrated over the RC and disk masks, respectively (see Tables 3 and 4 for galaxy specific values). These values are greater than the $\sim 2 \mu\text{G}$ found in the ~ 50 faint dwarf galaxies from the NVSS catalog (Roychowdhury & Chengalur 2012), and within the errors they are consistent with the $4.2 \mu\text{G}$ found toward the 12 local group dwarf galaxies reported in Chyży et al. (2011). The transverse field strength we measure in both masks is lower than the $9.7 \mu\text{G}$ found in the larger spiral galaxies in the WSRT SINGS sample (Heesen et al. 2014). The disk-integrated magnetic field strength is greater than the mask-integrated value because only the brightest galaxies can be integrated over the entire optical disk.

Our data allow the magnetic field strength to be measured on a resolved basis. In a few dwarf galaxies (e.g., NGC 1569, NGC 2366, NGC 4214), we find numerous regions where the magnetic field strength was measured to be as high as 30–50 μG in localized 100 pc regions (approximate area of the synthesized beam). In fact, the brightest RC_{Nth} flux density in our sample comes from a ~ 100 pc region in NGC 1569—the flux density from this unresolved region implied a magnetic field strength of $\sim 50 \mu\text{G}$. Heesen et al. (2015) analyzed in detail the RC_{Nth} spectrum of the nonthermal super bubble in IC 10, deriving a magnetic field strength of 44 μG . These are all strong magnetic fields akin to those found in the SF regions of larger spirals (e.g., the turbulent magnetic fields in NGC 6946’s SF regions; Tabatabaei et al. 2013). With such high magnetic field strengths, CRe could lose all their energy before diffusing into the ISM (rendering the region a local calorimeter). In IC 10, for example, Heesen et al. (2015) find that at 6.3 GHz, the CRe lifetime in the nonthermal super bubble is only 0.9 Myr, comparable with the age of 1 Myr derived from the observed curvature of the spectrum. For less intense SF regions, such as DDO 168, DDO 47, and DDO 53, we find peak local magnetic field strengths of 10–15 μG where CRe may have sufficient time to escape into the ISM. Once there:

- (1) the CRe , now losing energy through synchrotron radiation at a much slower rate, diffuse or are advected into the intergalactic medium (IGM) before they have time to radiate all their energy—this is the “non-calorimetric” situation that leads to the RC–FIR “conspiracy” (e.g., Bell 2003; Dale et al. 2009; Lacki et al. 2010), or
- (2) the CRe continue to diffuse to 1 kpc but, because they continue to radiate and lose energy, the frequency of

synchrotron emission shifts gradually to lower frequencies to the extent that emission falls outside of the 6 cm window.

Exploring these possibilities and their impact on the RC_{Nth} –SFR relation requires further information regarding the spectral index of the RC emission so that we can explore the CRe transport and aging timescales.

5. Summary

We used the VLA in C-configuration to make 6 cm ($\nu = 6.2$ GHz) observations of 40 dwarf galaxies taken from LITTLE THINGS (Hunter et al. 2012). Our images have a resolution of $3''\text{--}8''$ and an rms noise of $3\text{--}15 \mu\text{Jy beam}^{-1}$. We summarize our findings as follows:

1. Contamination from background sources is a prominent issue in earlier, low-resolution observations. Even at the high resolution of the current survey, it is not trivial to reliably remove the contribution from all unrelated background sources.
2. After removing background and ambiguous sources, a total of 22 out of the 40 LITTLE THINGS galaxies are associated with significant RC emission; eight are new detections. Where reliable flux densities of our sample exist in the literature, we find that our observations are generally in good agreement.
3. We find that the average thermal fraction in our sample is $50\% \pm 10\%$ and $70\% \pm 10\%$ at 6.2 GHz when integrating over the RC- and disk-based masks, respectively.
4. We present fits for the RC–SFR and FIR–SFR between SFRs of $\sim 10^{-4}$ and $1 M_{\odot} \text{ yr}^{-1}$ integrated over the RC mask and disk mask.
5. We find that the RC–SFR is broadly consistent with theoretical predictions when considering the RC mask but we find that the RC_{Nth} is suppressed when integrating over the disk.
6. The FIR emission in our sample is suppressed in both the RC and disk masks given the measured SFR.
7. When integrating the galaxy properties within the optical disk, we find that the dwarf galaxies are consistent with the linear Yun et al. (2001) RC–FIR relation. The “conspiracy” invoked to explain the relation continues to hold for our sample of dwarf galaxies (see Figure 11). The RC–FIR relation based on our RC mask-integrated results shows that our dwarf galaxies diverge from the linear Yun et al. (2001) relation with an RC excess at low luminosity.
8. In a few dwarf galaxies, the equipartition magnetic field strength reaches as high as 30 μG in several 100 pc regions, and in one case, 50 μG .
9. The average strength of the transverse magnetic field, based on equipartition, is $\sim 5.2 \mu\text{G}$ (RC mask) and $\sim 7.5 \mu\text{G}$ (disk averaged). This value is slightly lower than that for larger galaxies (e.g., 9.7 μG in WSRT SINGS; Heesen et al. 2014) but consistent with other studies of dwarf galaxies.

We thank Dan Smith for valuable discussions on the RC–FIR relation and his help with FIR-related work. We also appreciate Min Yun’s readiness to provide us with his *IRAS* and VLA data from the Yun et al. (2001) study. This manuscript has benefited from constructive comments on an

earlier version by the referee. G.K. acknowledges support from the UK Science and Technology Facilities Council (grant number ST/J501050/1). Likewise, E.B. and L.H. acknowledge support from the UK Science and Technology Facilities Council (grant number ST/M001008/1). This research has made use of the NASA/IPAC Extragalactic Database (NED), which is operated by the Jet Propulsion Laboratory, California Institute of Technology, under contract with the National Aeronautics and Space Administration.

Facilities: VLA, GALEX, Spitzer.

Appendix A

This appendix details notes on our individual RC observations. Here, we focus on prominent features and also on notable deviations from our normal line of calibration and image generation. Where no frequency is mentioned, flux densities were determined from the maps presented here. All other flux density values were taken from the NASA/IPAC Extragalactic Database (NED).

DDO 43: A bright source (87GB[BWE91] 0724+4053: flux density 37 mJy, located 2.5' from the image phase center) gave rise to prominent sidelobes across the FOV. DDO 43 was directly affected by, in particular, an E–W artifact.

DDO 50: A bright source (NVSS J081920+704907: flux density 18 mJy located 5.5' from the image phase center) exhibited weak sidelobes across the FOV. Selected parts of DDO 50 were directly affected by low-level artifacts. A single round of self-calibration was performed, which was successful in reducing the prominent sidelobes originating from NVSS J081920+704907.

DDO 52: Two bright sources (NVSS J082842+415056: flux density of 19 mJy located 2.5' from the image phase center, and NVSS J082814+415353: flux density of 39 mJy located 4' from the image phase center) generated weak sidelobes across the FOV. DDO 52 was not substantially affected by the artifacts. Self-calibration was not deemed necessary.

DDO 75: A bright source (NVSS J101030–044006) with a 1.4 GHz flux density of 305 mJy located 7' from the image phase center gave rise to weak sidelobes across the FOV. Parts of DDO 75 were directly affected by low-level artifacts. A single round of self-calibration was performed, which was successful in reducing the prominent sidelobes originating from NVSS J101030–044006.

DDO 101: A bright source (NVSS J115618+312805), with a 4.85 GHz flux density of 1.03 Jy located 9' from the image phase center, caused prominent sidelobes across the FOV. DDO 101 was directly affected by the artifacts. Self-calibration was not successful in reducing the effects of the sidelobes, which was attributed to the fact that NVSS J115618+312805 enters the first sidelobe of the primary beam, which results in it being seemingly time variable. We decided to use just three spectral windows for which NVSS J115618+312805 fell near the first null of the primary beam. This was successful in reducing its prominent sidelobes.

DDO 126: A bright double source (NVSS J122658+370719: flux density of 4.6 mJy located 1.5' from the image phase center) exhibited prominent sidelobes crossing the FOV. DDO 126 was directly affected by the artifacts. A single round of self-calibration was performed, which was successful in reducing the prominent sidelobes originating from NVSS J122658+370719.

DDO 154: Two bright sources (NVSS J125401+270357: flux density of 18 mJy located 5.5' from the image phase center and an

uncatalogued source of unknown flux density located 5.5' from the image phase center) led to weak sidelobes, which crossed through part of the FOV. DDO 154 was not directly affected. A single round of self-calibration was performed, which was successful in reducing the prominent sidelobes from both sources. Maps created with robust weighting (ROBUST = 0.0) did not reveal any significant regions of emission and instead another CLEAN was run using a robust weighting that was closer to natural weighting (ROBUST = 0.5).

DDO 187: A bright double source (NVSS J141556+230730: flux density of 55 mJy located 4.5' from the image phase center) caused prominent sidelobes across the FOV. DDO 187 was directly affected by the artifacts. A single round of self-calibration was performed, which was successful in reducing the prominent sidelobes originating from NVSS J141556+230730.

M81 dwA: A bright source (NVSS J082451+705808: 4.85 GHz flux density of 63 mJy, located 5.5' from the image phase center) gave rise to prominent sidelobes across the FOV. M81 dwA was directly affected by the artifacts. Self-calibration was not successful in reducing the effects of the sidelobes, which was attributed to the fact that NVSS J082451+705808 enters the first sidelobe of the primary beam, which results in it being seemingly time variable. We decided to use just three spectral windows for which NVSS J082451+705808 fell near the primary beam null. This was successful in reducing the prominent sidelobes originating from NVSS J082451+705808.

Mrk 178: The GALEX FUV image was dropped from the analysis due to being of poor quality.

NGC 1569: The Spitzer 24 μ m and 70 μ m images were dropped from the analysis due to being of poor quality.

NGC 3738: A bright triple source (NVSS J113545+543319: combined flux density of 63 mJy located 2' from the image phase center) exhibited prominent sidelobes across the FOV. NGC 3738 was directly affected by the artifacts. A single round of self-calibration was performed, which was successful in reducing the prominent sidelobes originating from NVSS J113545+543319.

NGC 4214: NGC 4214 (especially the H II region centered on 12^h15^m41^s.2, +36°19'04".6) was bright enough that prominent sidelobes were produced throughout the FOV. A single round of self-calibration was performed, which was successful in reducing the prominent sidelobes originating from NGC 4214.

UGC 8508: Two sources (not coincident with H α emission) from the 4' square aperture were judged as *not* originating from UGC 8508 and were accordingly masked out.

VII Zw 403: The Spitzer 24 μ m and 70 μ m images were dropped from the analysis due to being of poor quality.

WLM: A bright source (NVSS J000141–154040: 4.85 GHz flux density of 145 mJy, located 13' from the image phase center) caused prominent sidelobes across the FOV. WLM was directly affected by the artifacts. A single round of self-calibration was performed, which was successful in reducing the prominent sidelobes originating from NVSS J000141–154040.

Appendix B

4–8 GHz Radio Continuum Images of the LITTLE THINGS Sample

In this section, we provide images of the LITTLE THINGS sample. We show RC flux density contours superposed on ancillary LITTLE THINGS images (Hunter et al. 2012). As the dwarf galaxies are faint, extended RC emission does not show well when plotting contours at the native resolution. Therefore, for the lowest surface brightness contour, we smooth the RC

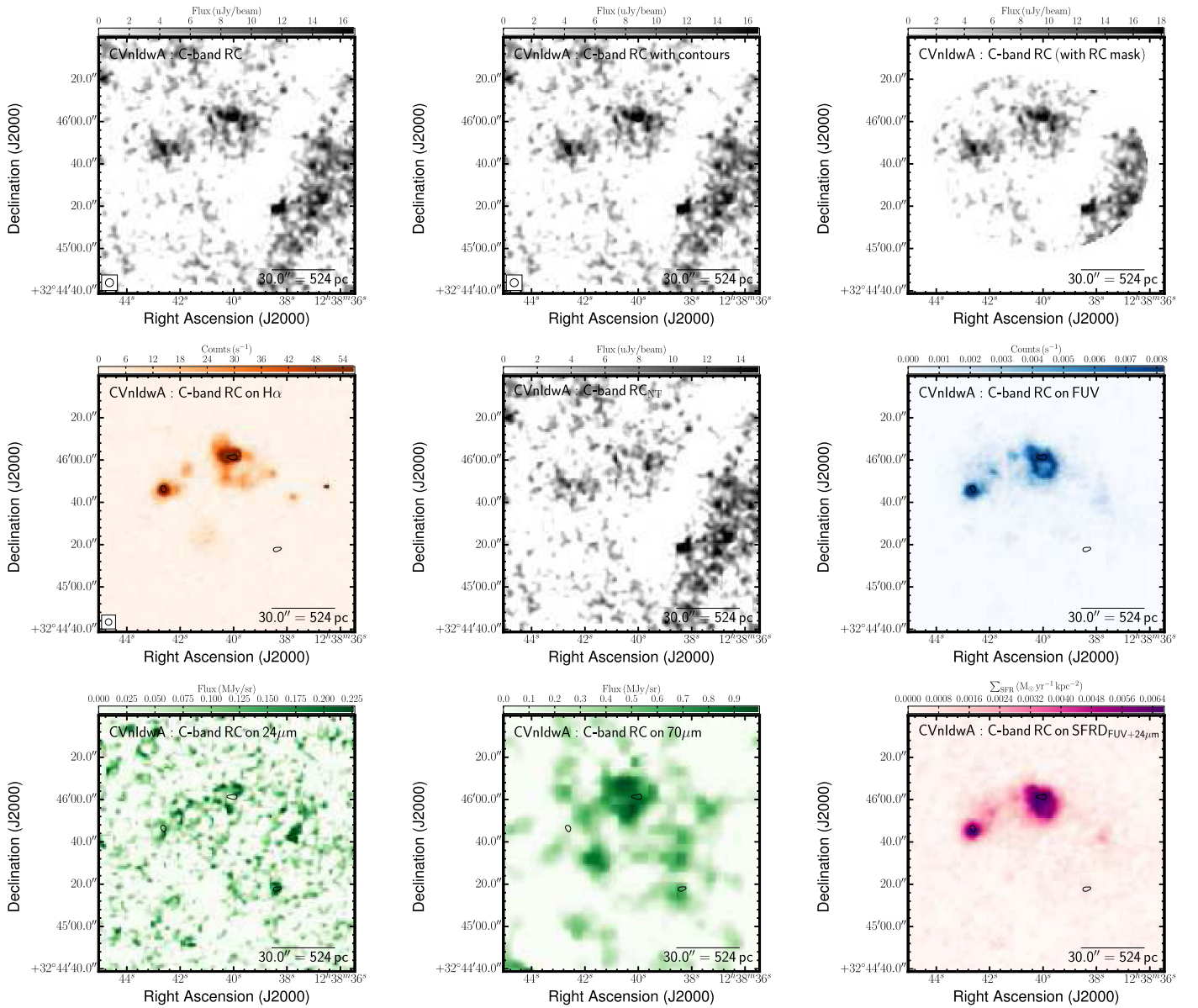


Figure 13. Multiwavelength coverage of CVn I dwA displaying a $2'0 \times 2'0$ area. We show the total RC flux density at the native resolution (top left) and again with contours (top-center). The RC contours are superposed on ancillary LITTLE THINGS images where possible: $H\alpha$ (middle left); RC_{Nth} obtained by subtracting the expected RC_{Th} based on the $H\alpha$ - RC_{Th} scaling factor of Deeg et al. (1997) from the total RC; *GALEX* FUV (middle right); *Spitzer* 24 μm (bottom left); *Spitzer* 70 μm (bottom center); FUV+24 μm -inferred SFRD from Leroy et al. (2012; bottom right). We also show the RC that was isolated by the RC-based masking technique (top right).

image with a Gaussian kernel of $10''$ and use a contour level corresponding to an S/N of 3. The remaining contours, at full spatial resolution, are drawn at S/N levels of 3, 6, 9, 18, 36, 72, and 144. We present the results of our RC-based masking technique and disk mask, which include ambiguous and background sources. Where ancillary data were available, we also show the following images: $H\alpha$, *GALEX* FUV, *Spitzer* 24 and 70 μm images, and FUV-inferred Σ_{SFR} from Leroy et al. (2012).

We provide images of the following dwarf galaxies: CVn I dwA (Figure 13), DDO 43 (Figure 14), DDO 46 (Figure 15), DDO 47 (Figure 16), DDO 50 (Figure 17), DDO 52 (Figure 18), DDO 53 (Figure 19), DDO 63

(Figure 20), DDO 69 (Figure 21), DDO 70 (Figure 22), DDO 75 (Figure 23), DDO 87 (Figure 24), DDO 101 (Figure 25), DDO 126 (Figure 26), DDO 133 (Figure 27), DDO 154 (Figure 28), DDO 155 (Figure 29), DDO 165 (Figure 30), DDO 167 (Figure 31), DDO 168 (Figure 32), DDO 187 (Figure 33), DDO 210 (Figure 34), DDO 216 (Figure 35), F564 V3 (Figure 36), Haro 29 (Figure 37), Haro 36 (Figure 38), IC 10 (Figure 39), IC 1613 (Figure 40), LGS 3 (Figure 41), M81 DwA (Figure 42), Mrk 178 (Figure 43), NGC 1569 (Figure 44), NGC 2366 (Figure 45), NGC 3738 (Figure 46), NGC 4163 (Figure 47), NGC 4214 (Figure 48), Sag DIG (Figure 49), UGC 8508 (Figure 50), VII Zw 403 (Figure 51), and WLM (Figure 52).

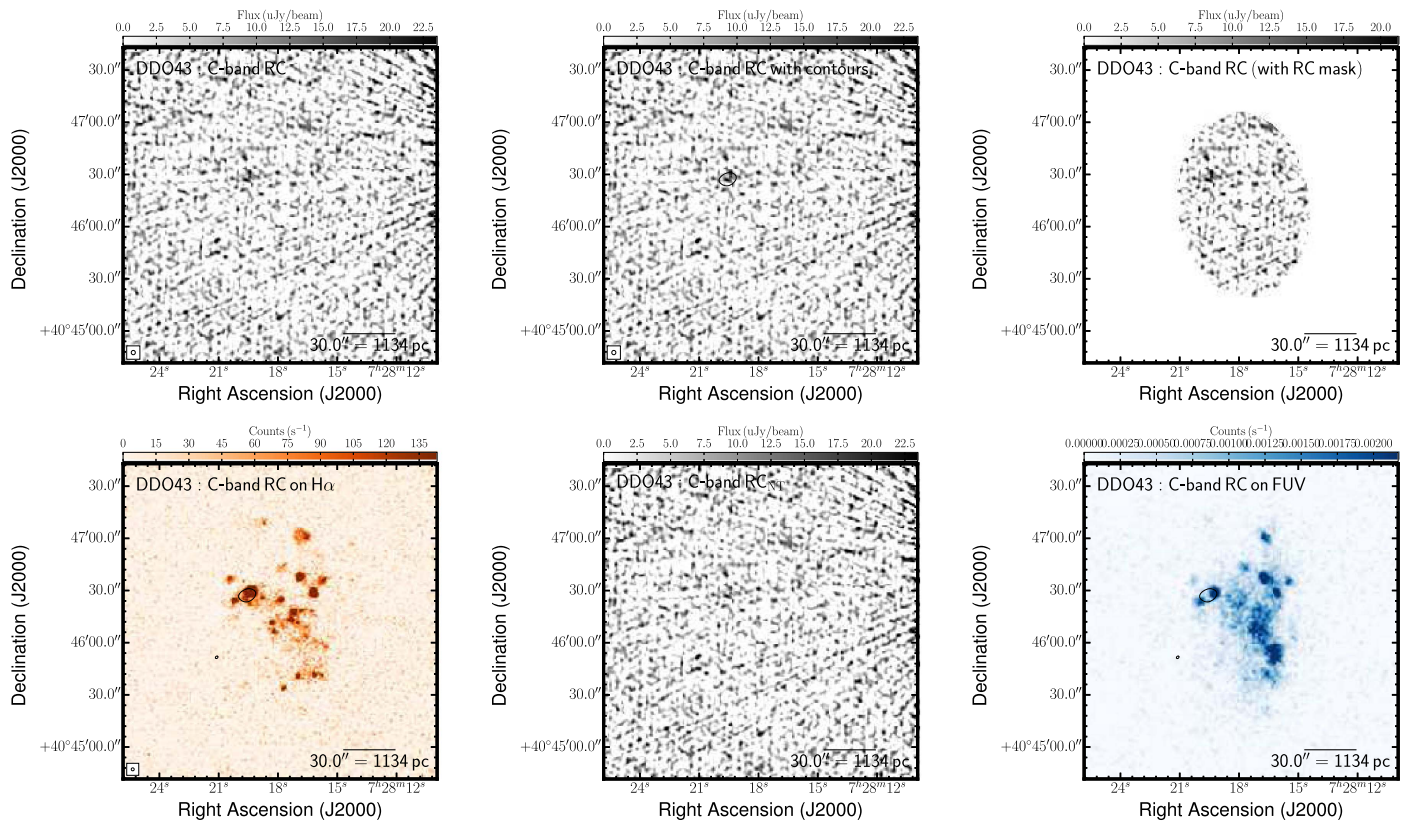


Figure 14. Multiwavelength coverage of DDO 43 displaying a $3'0 \times 3'0$ area. We show the total RC flux density at the native resolution (top left) and again with contours (top center). The RC contours are superposed on ancillary LITTLE THINGS images where possible: H α (middle left); RC_{Nth} obtained by subtracting the expected RC_{Th} based on the H α –RC_{Th} scaling factor of Deeg et al. (1997) from the total RC; GALEX FUV (middle right); *Spitzer* 24 μm (bottom left); *Spitzer* 70 μm (bottom center); FUV+24 μm -inferred SFRD from Leroy et al. (2012; bottom right). We also show the RC that was isolated by the RC-based masking technique (top right).

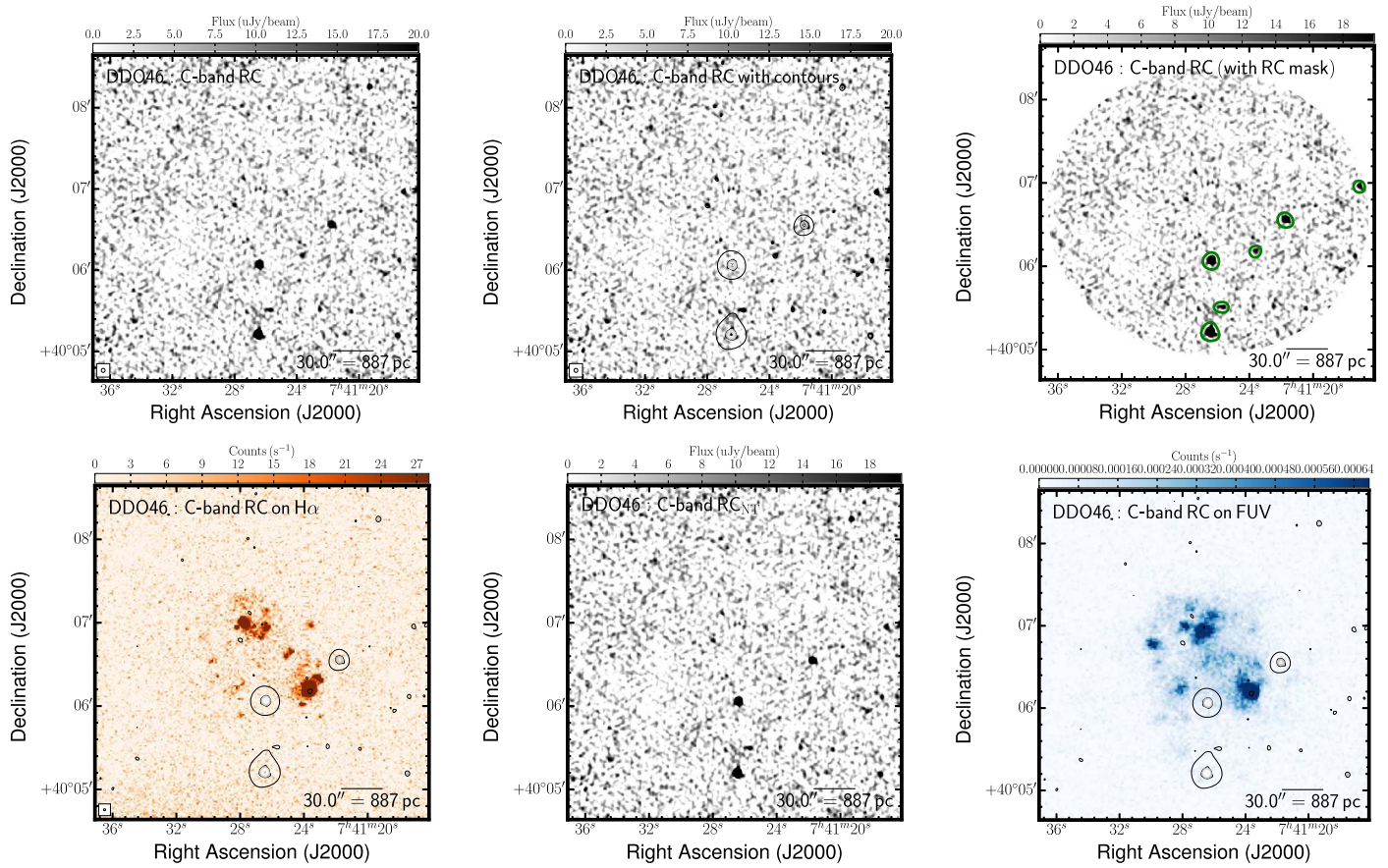


Figure 15. Multiwavelength coverage of DDO 46 displaying a $4'0 \times 4'0$ area. We show the total RC flux density at the native resolution (top left) and again with contours (top center). The RC contours are superposed on ancillary LITTLE THINGS images where possible: $H\alpha$ (middle left); RC_{Nth} obtained by subtracting the expected RC_{Th} based on the $H\alpha$ - RC_{Th} scaling factor of Deeg et al. (1997) from the total RC; *GALEX* FUV (middle right); *Spitzer* $24 \mu m$ (bottom left); *Spitzer* $70 \mu m$ (bottom center); FUV+ $24 \mu m$ -inferred SFRD from Leroy et al. (2012; bottom right). We also show the RC that was isolated by the RC-based masking technique (top right).

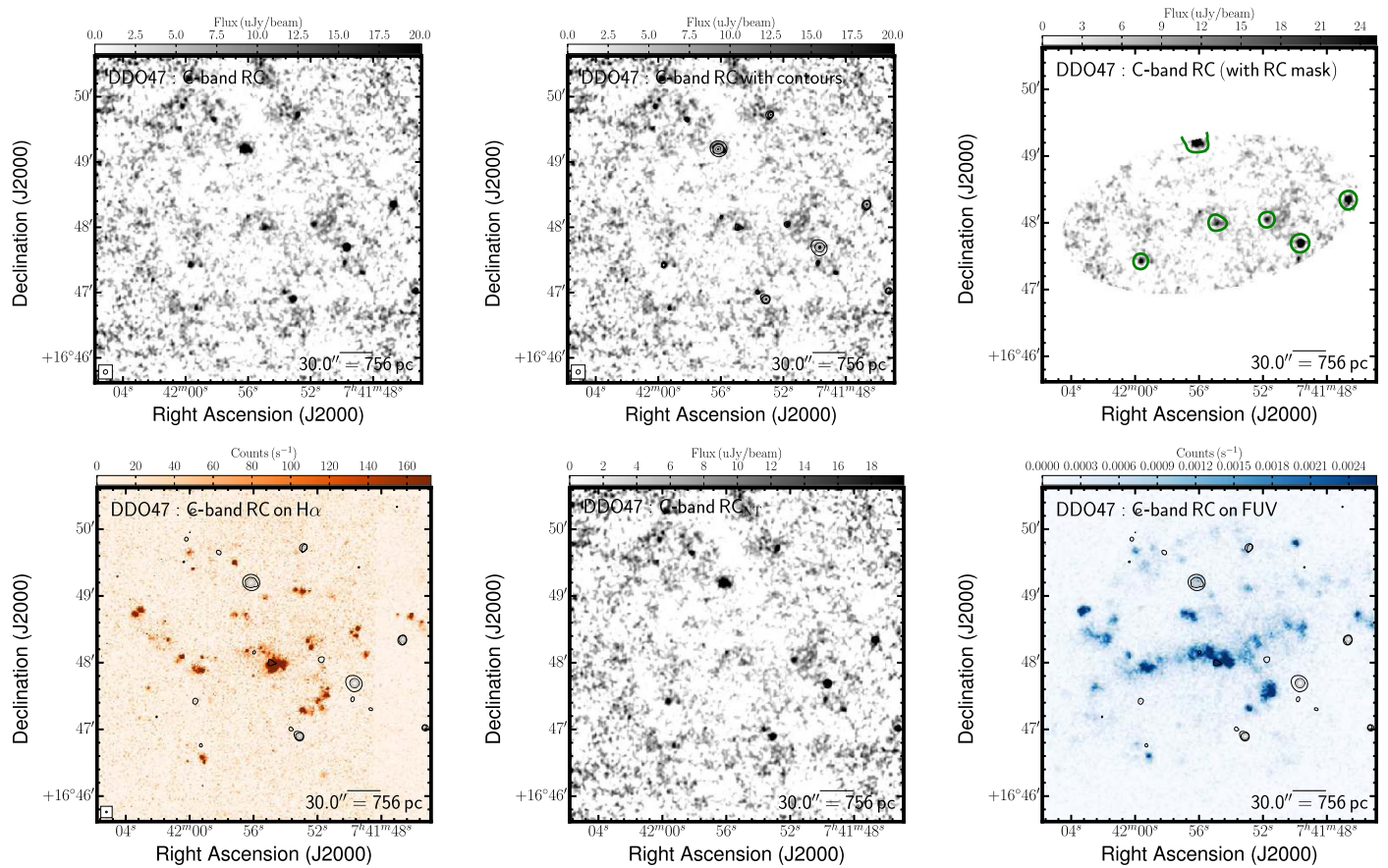


Figure 16. Multiwavelength coverage of DDO 47 displaying a $5'0 \times 5'0$ area. We show the total RC flux density at the native resolution (top left) and again with contours (top center). The RC contours are superposed on ancillary LITTLE THINGS images where possible: $H\alpha$ (middle left); RC_{Nth} obtained by subtracting the expected RC_{Th} based on the $H\alpha$ - RC_{Th} scaling factor of Deeg et al. (1997) from the total RC; *GALEX* FUV (middle right); *Spitzer* $24 \mu\text{m}$ (bottom left); *Spitzer* $70 \mu\text{m}$ (bottom center); FUV+ $24 \mu\text{m}$ -inferred SFRD from Leroy et al. (2012; bottom right). We also show the RC that was isolated by the RC-based masking technique (top right).

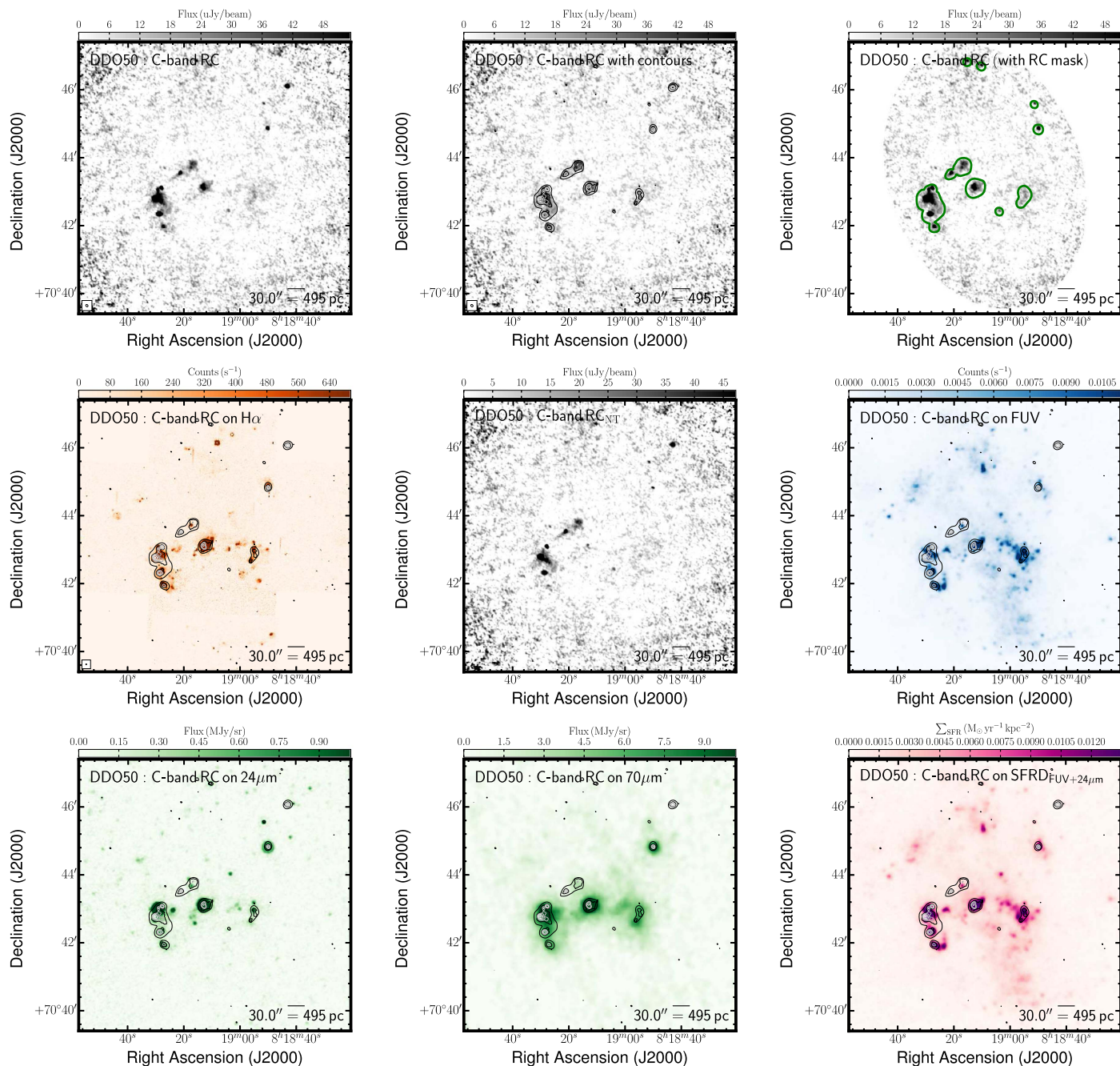


Figure 17. Multiwavelength coverage of DDO 50 displaying a $8'0 \times 8'0$ area. We show the total RC flux density at the native resolution (top left) and again with contours (top center). The RC contours are superposed on ancillary LITTLE THINGS images where possible: $H\alpha$ (middle left); RC_{Nth} obtained by subtracting the expected RC_{Th} based on the $H\alpha$ - RC_{Th} scaling factor of Deeg et al. (1997) from the total RC; *GALEX* FUV (middle right); *Spitzer* $24 \mu m$ (bottom left); *Spitzer* $70 \mu m$ (bottom center); FUV+ $24 \mu m$ -inferred SFRD from Leroy et al. (2012; bottom right). We also show the RC that was isolated by the RC-based masking technique (top right).

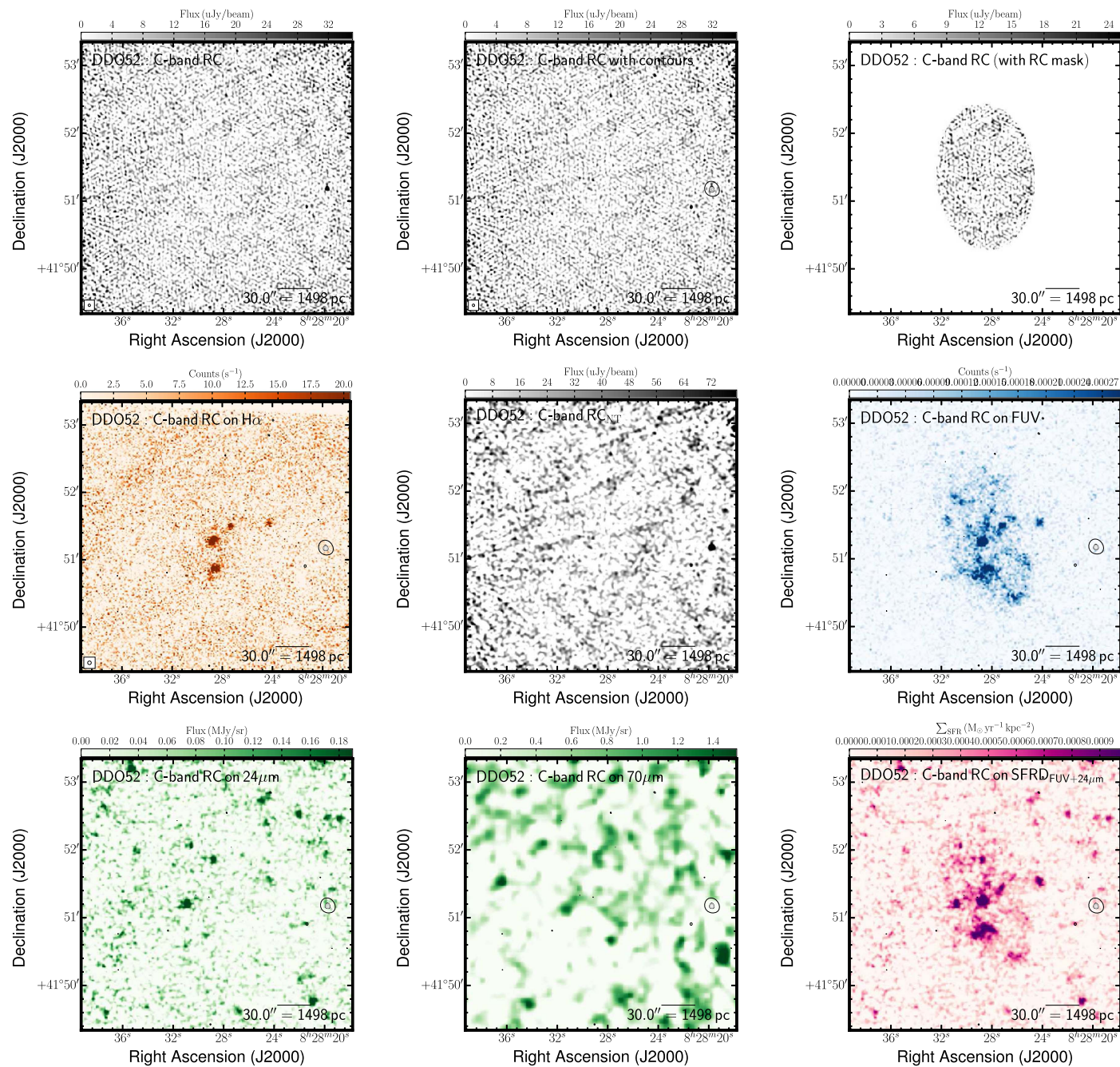


Figure 18. Multiwavelength coverage of DDO 52 displaying a $4'0 \times 4'0$ area. We show the total RC flux density at the native resolution (top left) and again with contours (top center). The RC contours are superposed on ancillary LITTLE THINGS images where possible: $H\alpha$ (middle left); RC_{Nth} obtained by subtracting the expected RC_{Th} based on the $H\alpha$ – RC_{Th} scaling factor of Deeg et al. (1997) from the total RC; *GALEX* FUV (middle right); *Spitzer* $24 \mu m$ (bottom left); *Spitzer* $70 \mu m$ (bottom center); FUV+ $24 \mu m$ -inferred SFRD from Leroy et al. (2012; bottom right). We also show the RC that was isolated by the RC-based masking technique (top right).

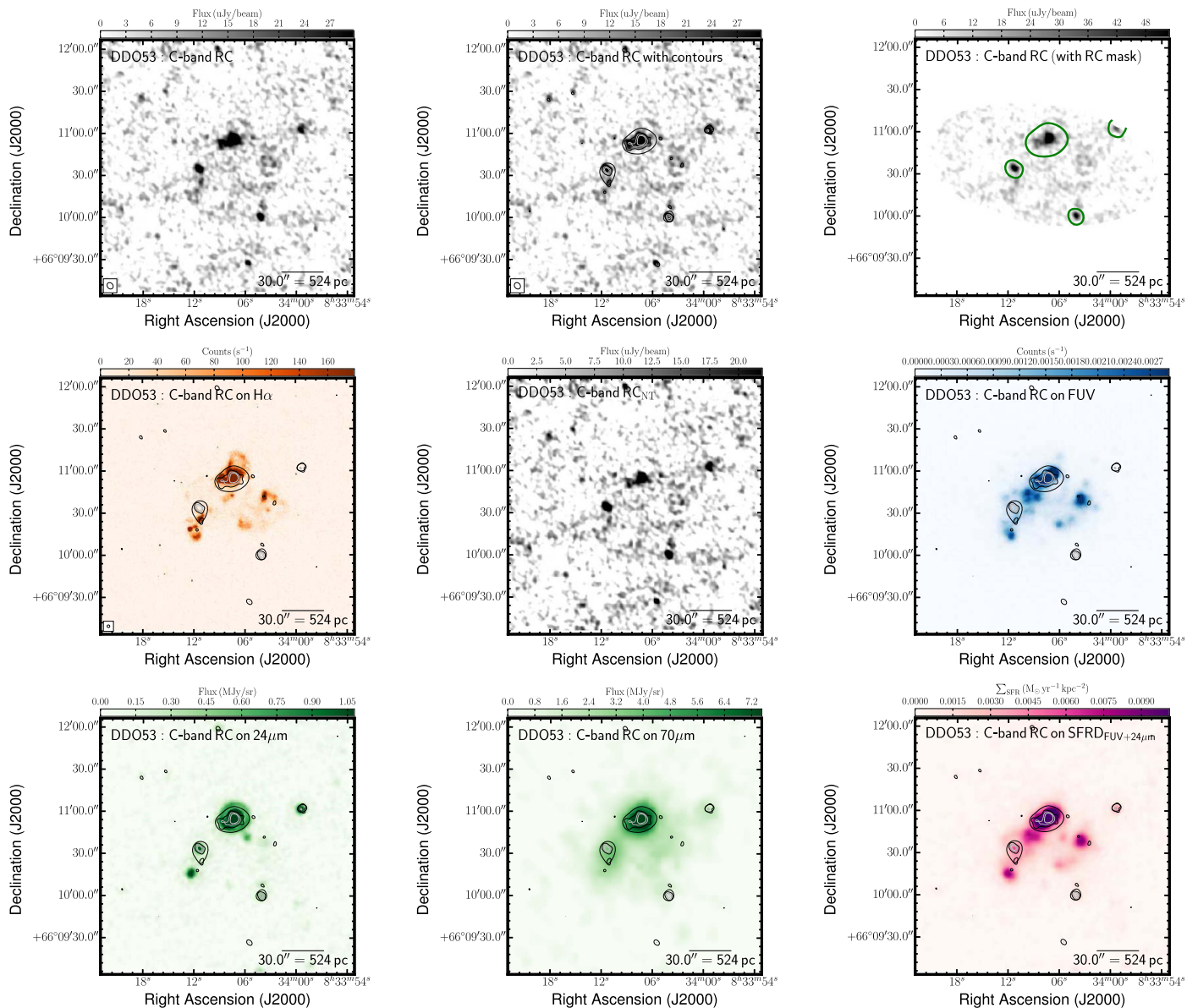


Figure 19. Multiwavelength coverage of DDO 53 displaying a $3\frac{1}{6} \times 3\frac{1}{6}$ area. We show the total RC flux density at the native resolution (top left) and again with contours (top center). The RC contours are superposed on ancillary LITTLE THINGS images where possible: $H\alpha$ (middle left); RC_{Nth} obtained by subtracting the expected RC_{Th} based on the $H\alpha$ - RC_{Th} scaling factor of Deeg et al. (1997) from the total RC; *GALEX* FUV (middle right); *Spitzer* $24\ \mu m$ (bottom left); *Spitzer* $70\ \mu m$ (bottom center); FUV+ $24\ \mu m$ -inferred SFRD from Leroy et al. (2012; bottom right). We also show the RC that was isolated by the RC-based masking technique (top right).

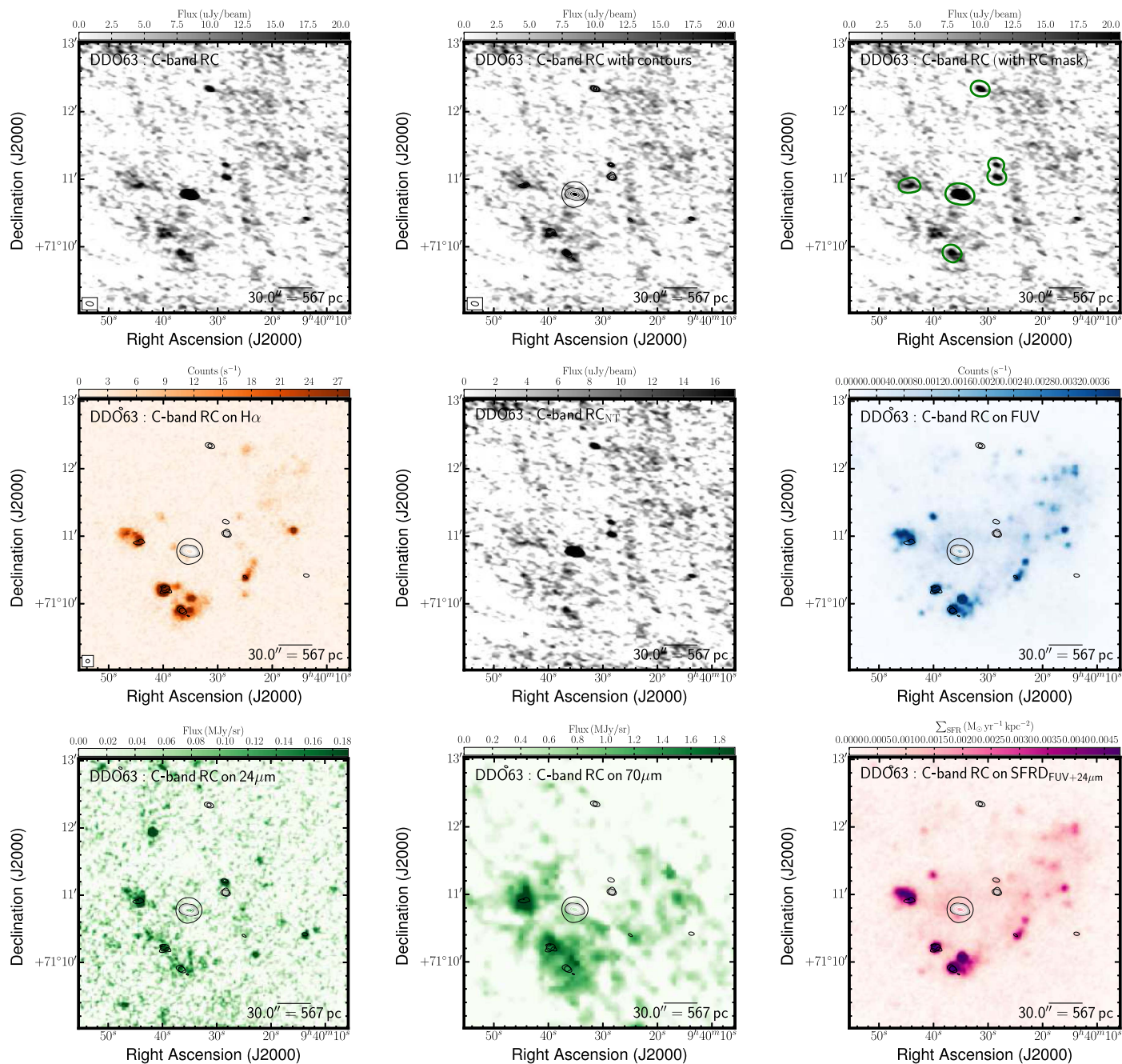


Figure 20. Multiwavelength coverage of DDO 63 displaying a 4.0×4.0 area. We show the total RC flux density at the native resolution (top left) and again with contours (top center). The RC contours are superposed on ancillary LITTLE THINGS images where possible: $H\alpha$ (middle left); RC_{NTh} obtained by subtracting the expected RC_{Th} based on the $H\alpha$ - RC_{Th} scaling factor of Deeg et al. (1997) from the total RC; *GALEX* FUV (middle right); *Spitzer* $24 \mu m$ (bottom left); *Spitzer* $70 \mu m$ (bottom center); FUV+ $24 \mu m$ -inferred SFRD from Leroy et al. (2012; bottom right). We also show the RC that was isolated by the RC-based masking technique (top right).

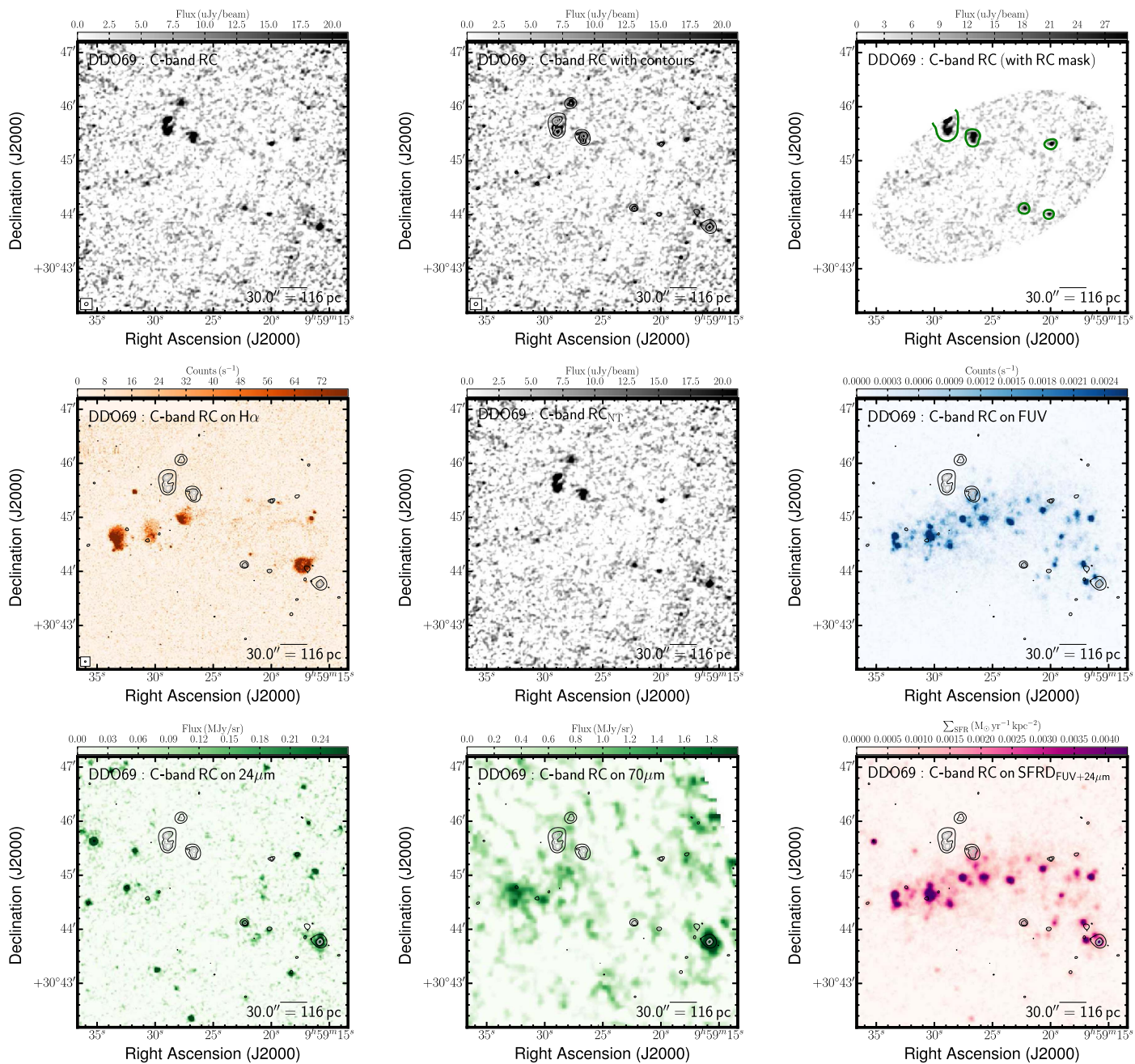


Figure 21. Multiwavelength coverage of DDO 69 displaying a $5'.0 \times 5'.0$ area. We show the total RC flux density at the native resolution (top left) and again with contours (top center). The RC contours are superposed on ancillary LITTLE THINGS images where possible: $H\alpha$ (middle left); RC_{NTh} obtained by subtracting the expected RC_{Th} based on the $H\alpha$ - RC_{Th} scaling factor of Deeg et al. (1997) from the total RC; *GALEX* FUV (middle right); *Spitzer* $24 \mu m$ (bottom left); *Spitzer* $70 \mu m$ (bottom center); FUV+ $24 \mu m$ -inferred SFRD from Leroy et al. (2012; bottom right). We also show the RC that was isolated by the RC-based masking technique (top right).

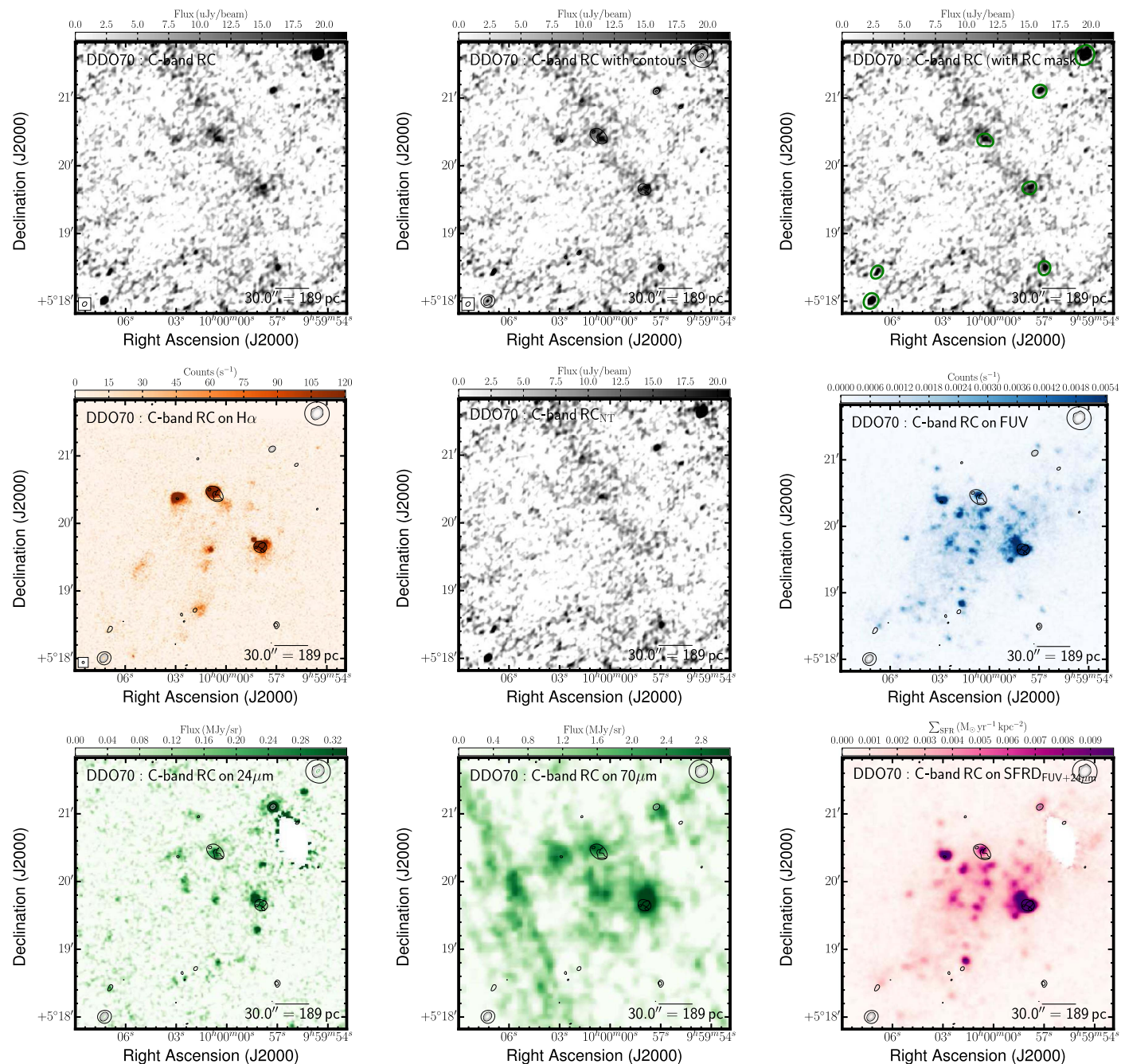


Figure 22. Multiwavelength coverage of DDO 70 displaying a 4.0×4.0 area. We show the total RC flux density at the native resolution (top left) and again with contours (top center). The RC contours are superposed on ancillary LITTLE THINGS images where possible: $H\alpha$ (middle left); RC_{Nth} obtained by subtracting the expected RC_{Th} based on the $H\alpha$ - RC_{Th} scaling factor of Deeg et al. (1997) from the total RC; *GALEX* FUV (middle right); *Spitzer* $24 \mu m$ (bottom left); *Spitzer* $70 \mu m$ (bottom center); FUV+ $24 \mu m$ -inferred SFRD from Leroy et al. (2012; bottom right). We also show the RC that was isolated by the RC-based masking technique (top right).

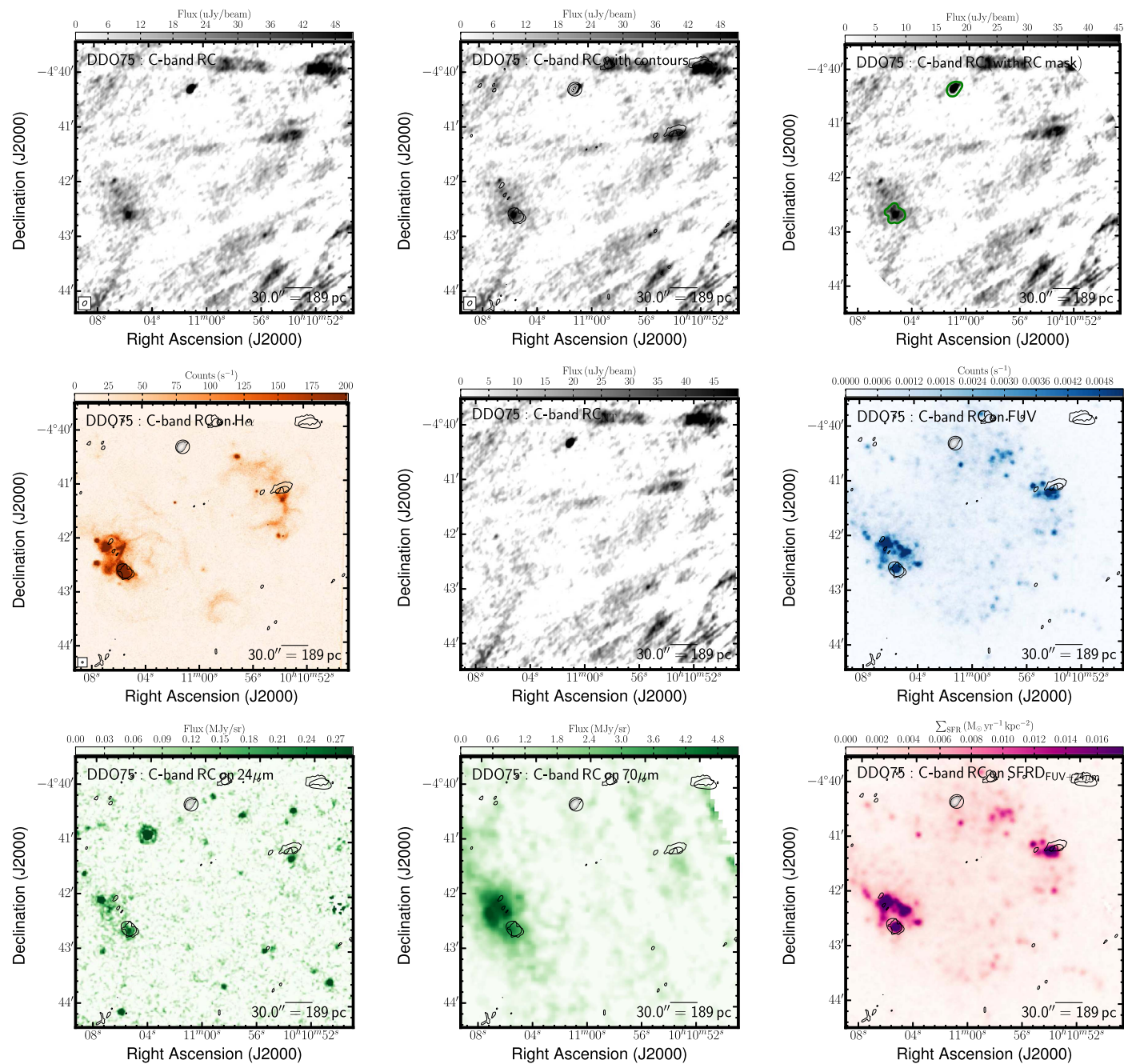


Figure 23. Multiwavelength coverage of DDO 75 displaying a $6/3 \times 6/3$ area. We show the total RC flux density at the native resolution (top left) and again with contours (top center). The RC contours are superposed on ancillary LITTLE THINGS images where possible: $H\alpha$ (middle left); RC_{Nth} obtained by subtracting the expected RC_{Th} based on the $H\alpha$ - RC_{Th} scaling factor of Deeg et al. (1997) from the total RC; *GALEX* FUV (middle right); *Spitzer* $24 \mu m$ (bottom left); *Spitzer* $70 \mu m$ (bottom center); FUV+ $24 \mu m$ -inferred SFRD from Leroy et al. (2012; bottom right). We also show the RC that was isolated by the RC-based masking technique (top right).

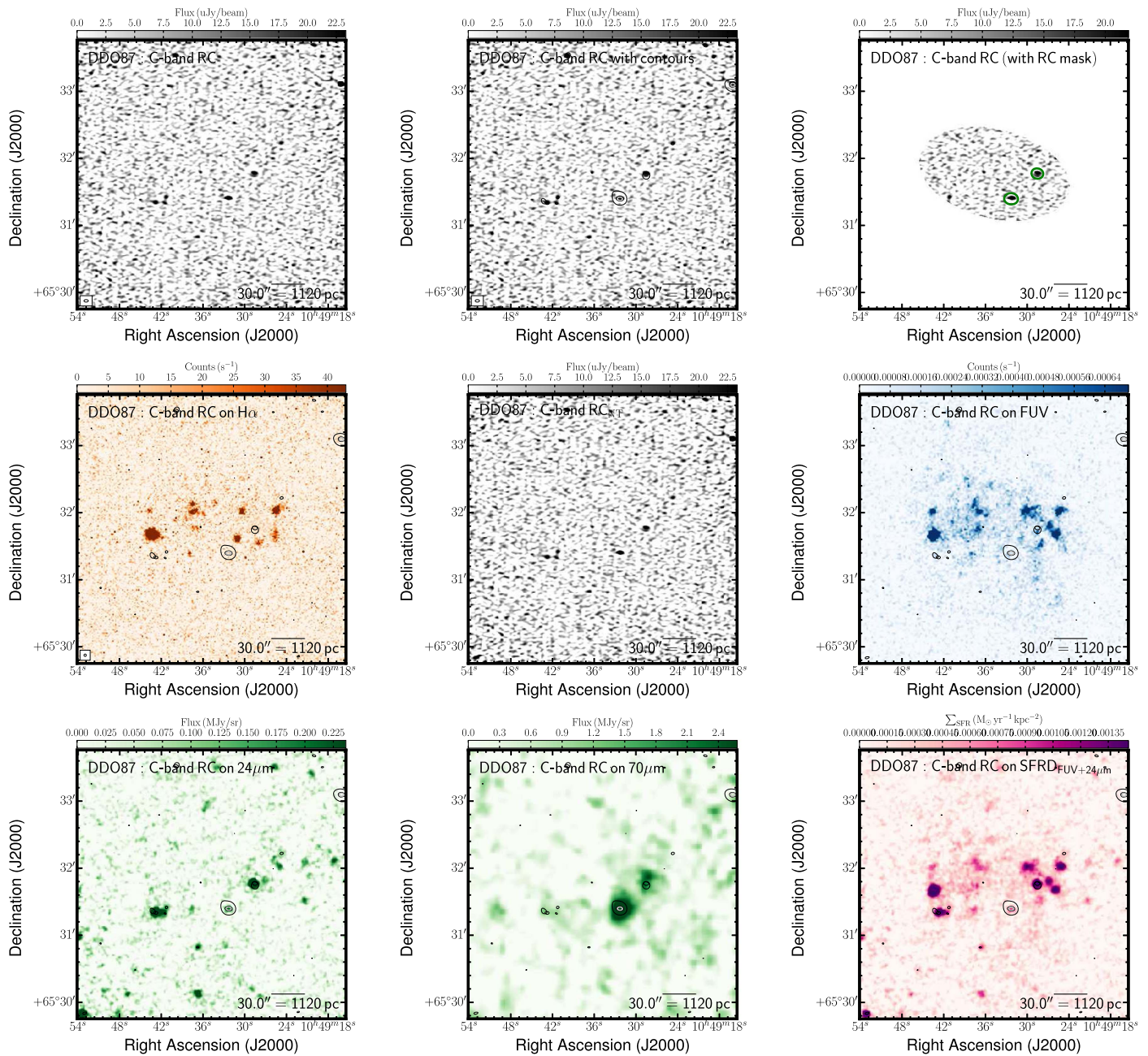


Figure 24. Multiwavelength coverage of DDO 87 displaying a 4.0×4.0 area. We show the total RC flux density at the native resolution (top left) and again with contours (top center). The RC contours are superposed on ancillary LITTLE THINGS images where possible: $H\alpha$ (middle left); RC_{Nth} obtained by subtracting the expected RC_{Th} based on the $H\alpha$ - RC_{Th} scaling factor of Deeg et al. (1997) from the total RC; *GALEX* FUV (middle right); *Spitzer* $24 \mu m$ (bottom left); *Spitzer* $70 \mu m$ (bottom center); FUV+ $24 \mu m$ -inferred SFRD from Leroy et al. (2012; bottom right). We also show the RC that was isolated by the RC-based masking technique (top right).

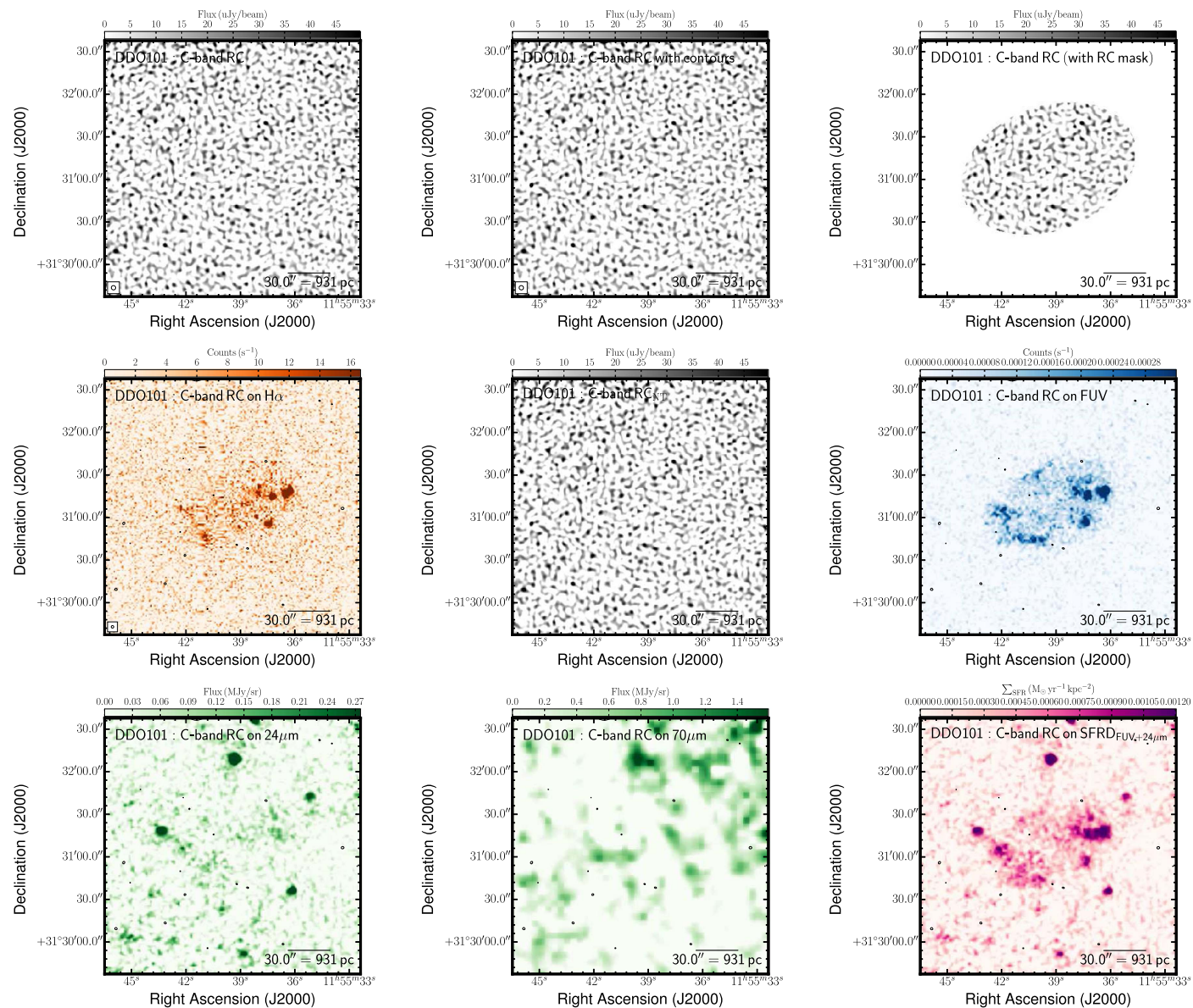


Figure 25. Multiwavelength coverage of DDO 101 displaying a $3'0 \times 3'0$ area. We show the total RC flux density at the native resolution (top left) and again with contours (top center). The RC contours are superposed on ancillary LITTLE THINGS images where possible: $H\alpha$ (middle left); RC_{Nth} obtained by subtracting the expected RC_{Th} based on the $H\alpha$ - RC_{Th} scaling factor of Deeg et al. (1997) from the total RC; *GALEX* FUV (middle right); *Spitzer* $24 \mu m$ (bottom left); *Spitzer* $70 \mu m$ (bottom center); FUV+ $24 \mu m$ -inferred SFRD from Leroy et al. (2012; bottom right). We also show the RC that was isolated by the RC-based masking technique (top right).

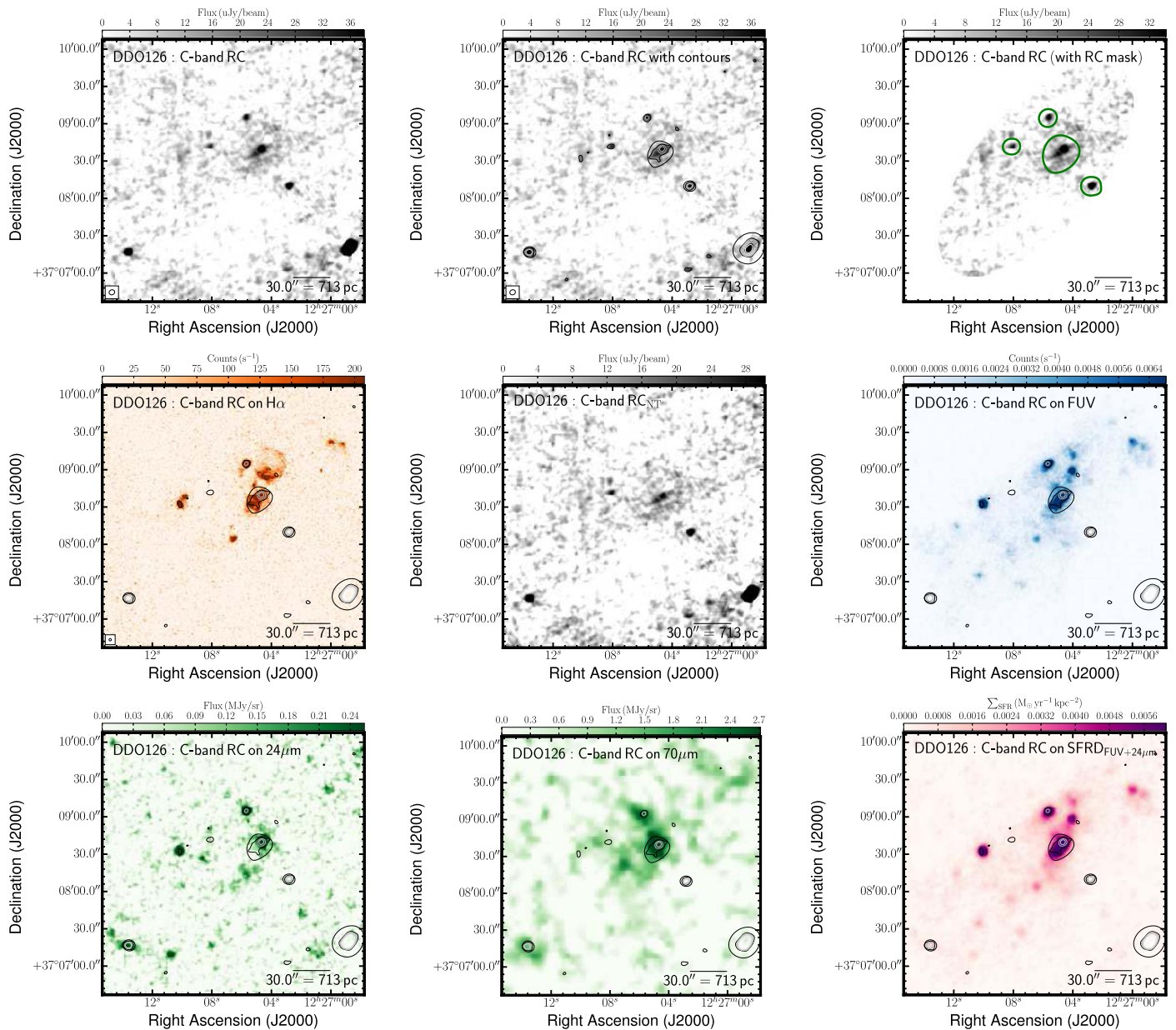


Figure 26. Multiwavelength coverage of DDO 126 displaying a $3\frac{1}{5} \times 3\frac{1}{5}$ area. We show the total RC flux density at the native resolution (top left) and again with contours (top center). The RC contours are superposed on ancillary LITTLE THINGS images where possible: $H\alpha$ (middle left); RC_{Nth} obtained by subtracting the expected RC_{Th} based on the $H\alpha$ - RC_{Th} scaling factor of Deeg et al. (1997) from the total RC; *GALEX* FUV (middle right); *Spitzer* $24\ \mu\text{m}$ (bottom left); *Spitzer* $70\ \mu\text{m}$ (bottom center); FUV+ $24\ \mu\text{m}$ -inferred SFRD from Leroy et al. (2012; bottom right). We also show the RC that was isolated by the RC-based masking technique (top right).

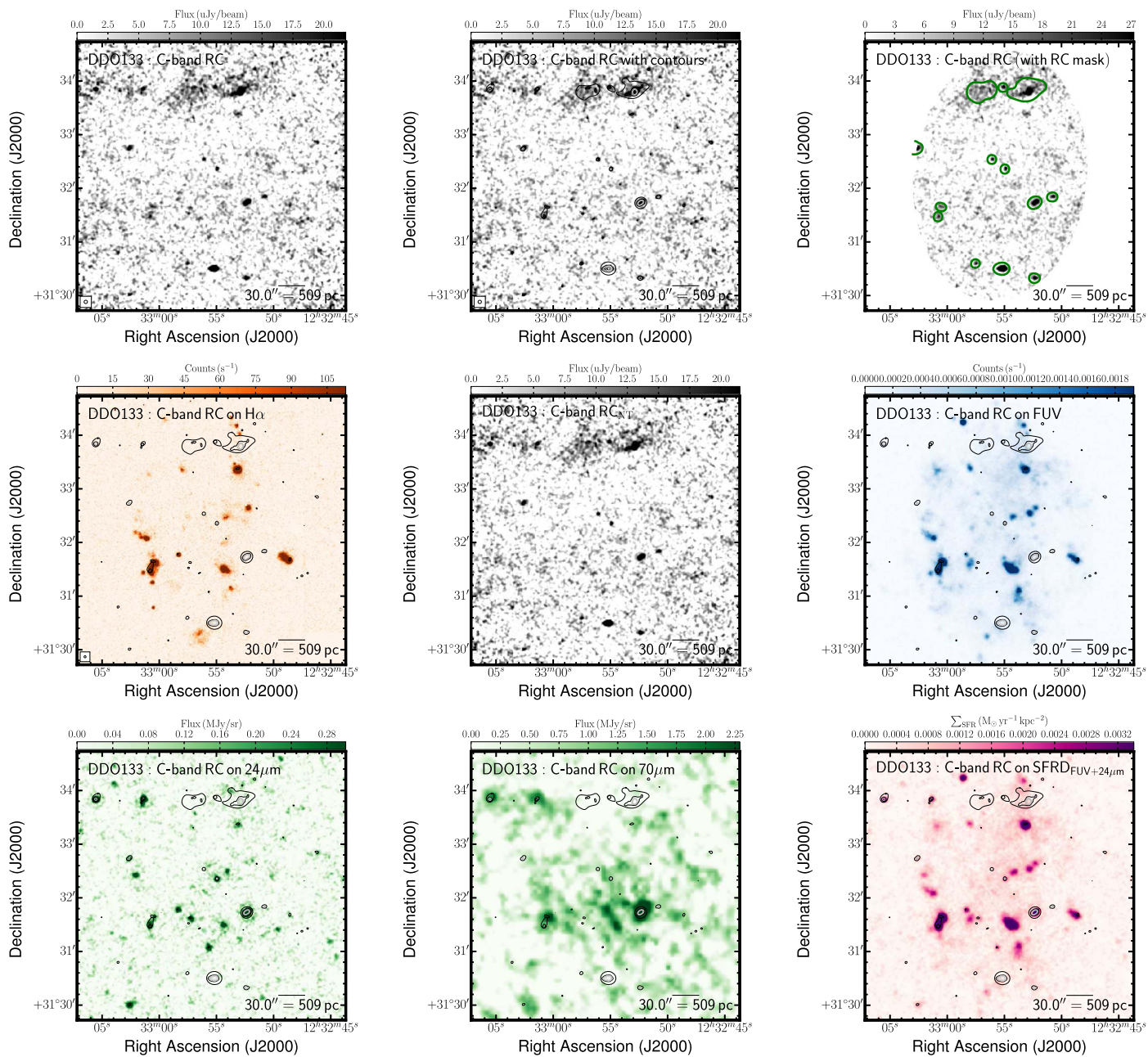


Figure 27. Multiwavelength coverage of DDO 133 displaying a $5'0 \times 5'0$ area. We show the total RC flux density at the native resolution (top left) and again with contours (top center). The RC contours are superposed on ancillary LITTLE THINGS images where possible: $H\alpha$ (middle left); RC_{Nth} obtained by subtracting the expected RC_{Th} based on the $H\alpha$ - RC_{Th} scaling factor of Deeg et al. (1997) from the total RC; *GALEX* FUV (middle right); *Spitzer* $24 \mu m$ (bottom center); *Spitzer* $70 \mu m$ (bottom center); FUV+ $24 \mu m$ -inferred SFRD from Leroy et al. (2012; bottom right). We also show the RC that was isolated by the RC-based masking technique (top right).

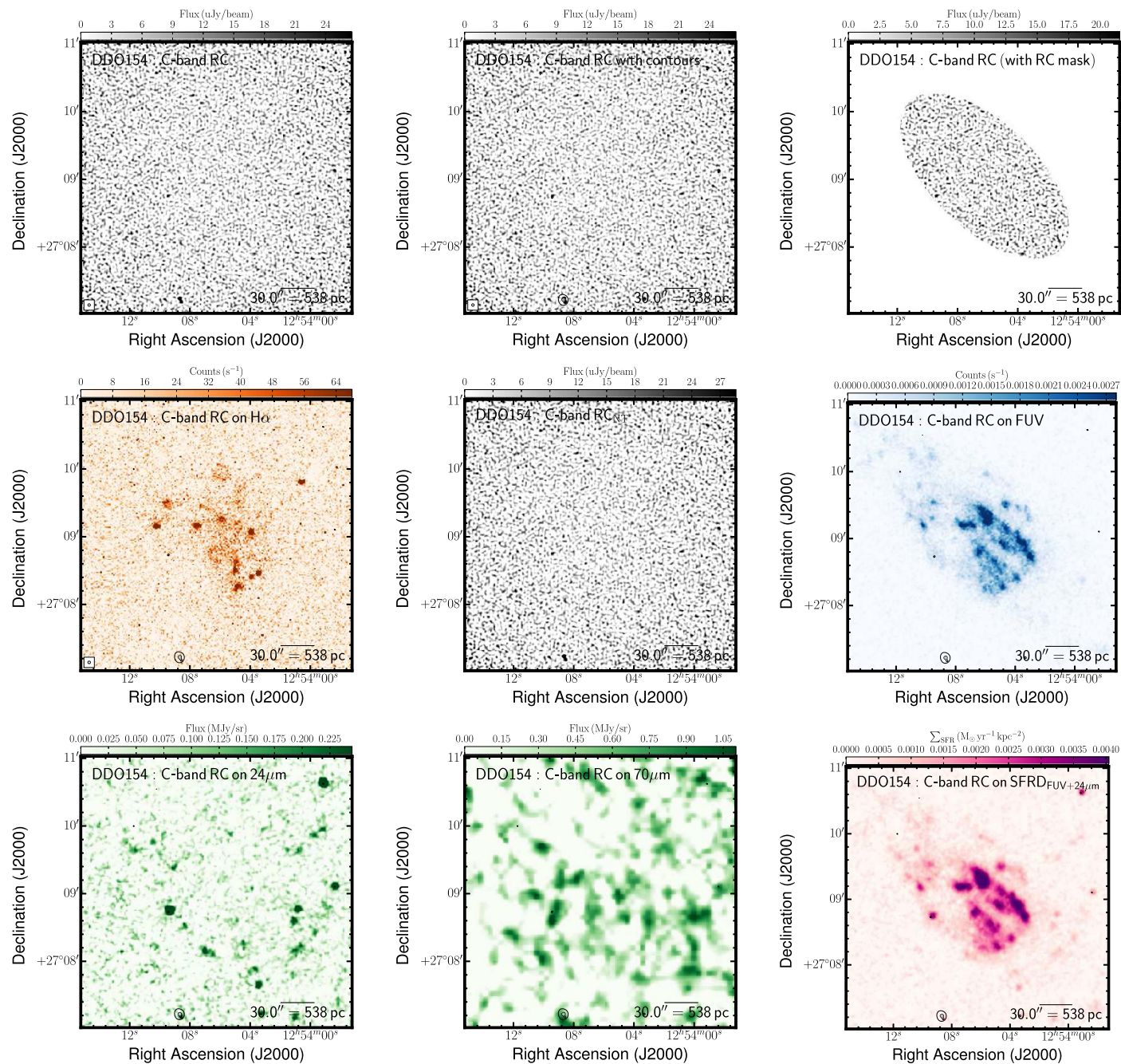


Figure 28. Multiwavelength coverage of DDO 154 displaying a $4'0 \times 4'0$ area. We show the total RC flux density at the native resolution (top left) and again with contours (top center). The RC contours are superposed on ancillary LITTLE THINGS images where possible: $H\alpha$ (middle left); RC_{Nth} obtained by subtracting the expected RC_{Th} based on the $H\alpha$ - RC_{Th} scaling factor of Deeg et al. (1997) from the total RC; *GALEX* FUV (middle right); *Spitzer* $24 \mu m$ (bottom left); *Spitzer* $70 \mu m$ (bottom center); FUV+ $24 \mu m$ -inferred SFRD from Leroy et al. (2012; bottom right). We also show the RC that was isolated by the RC-based masking technique (top right).

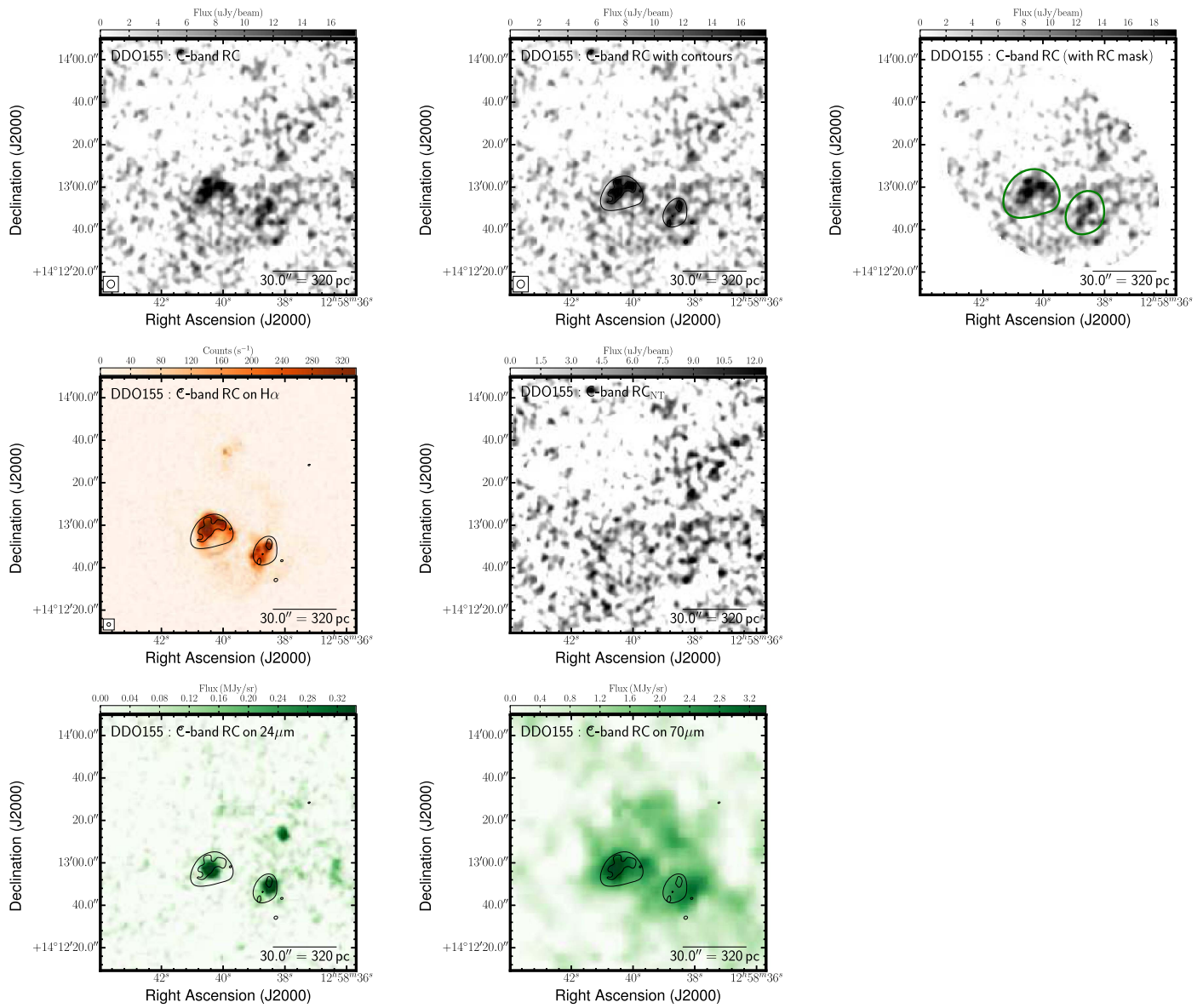


Figure 29. Multiwavelength coverage of DDO 155 displaying a $2'0 \times 2'0$ area. We show the total RC flux density at the native resolution (top left) and again with contours (top center). The RC contours are superposed on ancillary LITTLE THINGS images where possible: $H\alpha$ (middle left); RC_{Nth} obtained by subtracting the expected RC_{Th} based on the $H\alpha$ - RC_{Th} scaling factor of Deeg et al. (1997) from the total RC; *GALEX* FUV (middle right); *Spitzer* $24 \mu m$ (bottom left); *Spitzer* $70 \mu m$ (bottom center); FUV+ $24 \mu m$ -inferred SFRD from Leroy et al. (2012; bottom right). We also show the RC that was isolated by the RC-based masking technique (top right).

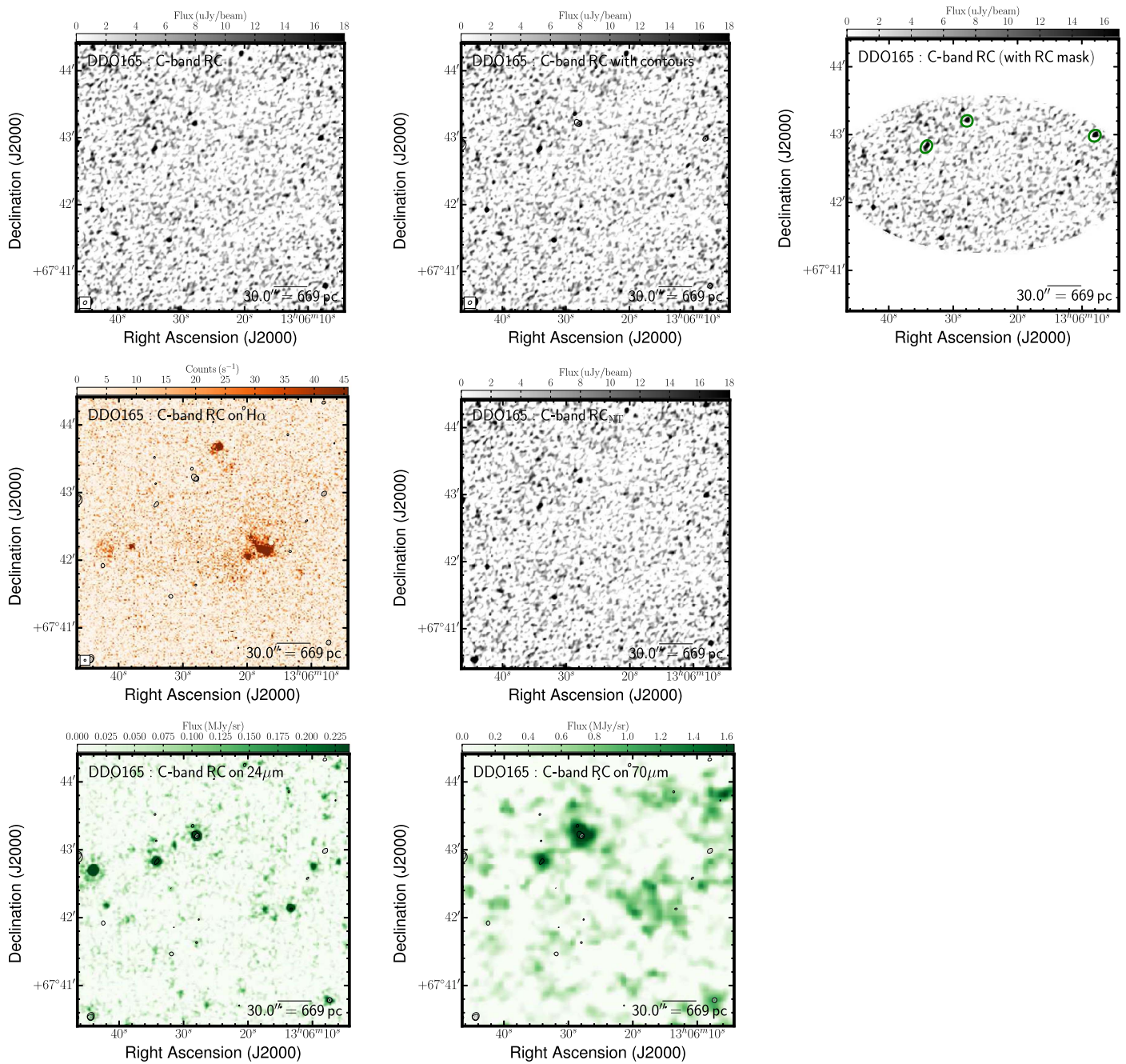


Figure 30. Multiwavelength coverage of DDO 165 displaying a $4'0 \times 4'0$ area. We show the total RC flux density at the native resolution (top left) and again with contours (top center). The RC contours are superposed on ancillary LITTLE THINGS images where possible: H α (middle left); RC_{Nth} obtained by subtracting the expected RC_{Th} based on the H α –RC_{Th} scaling factor of Deeg et al. (1997) from the total RC; GALEX FUV (middle right); Spitzer 24 μ m (bottom left); Spitzer 70 μ m (bottom center); FUV+24 μ m-inferred SFRD from Leroy et al. (2012; bottom right). We also show the RC that was isolated by the RC-based masking technique (top right).

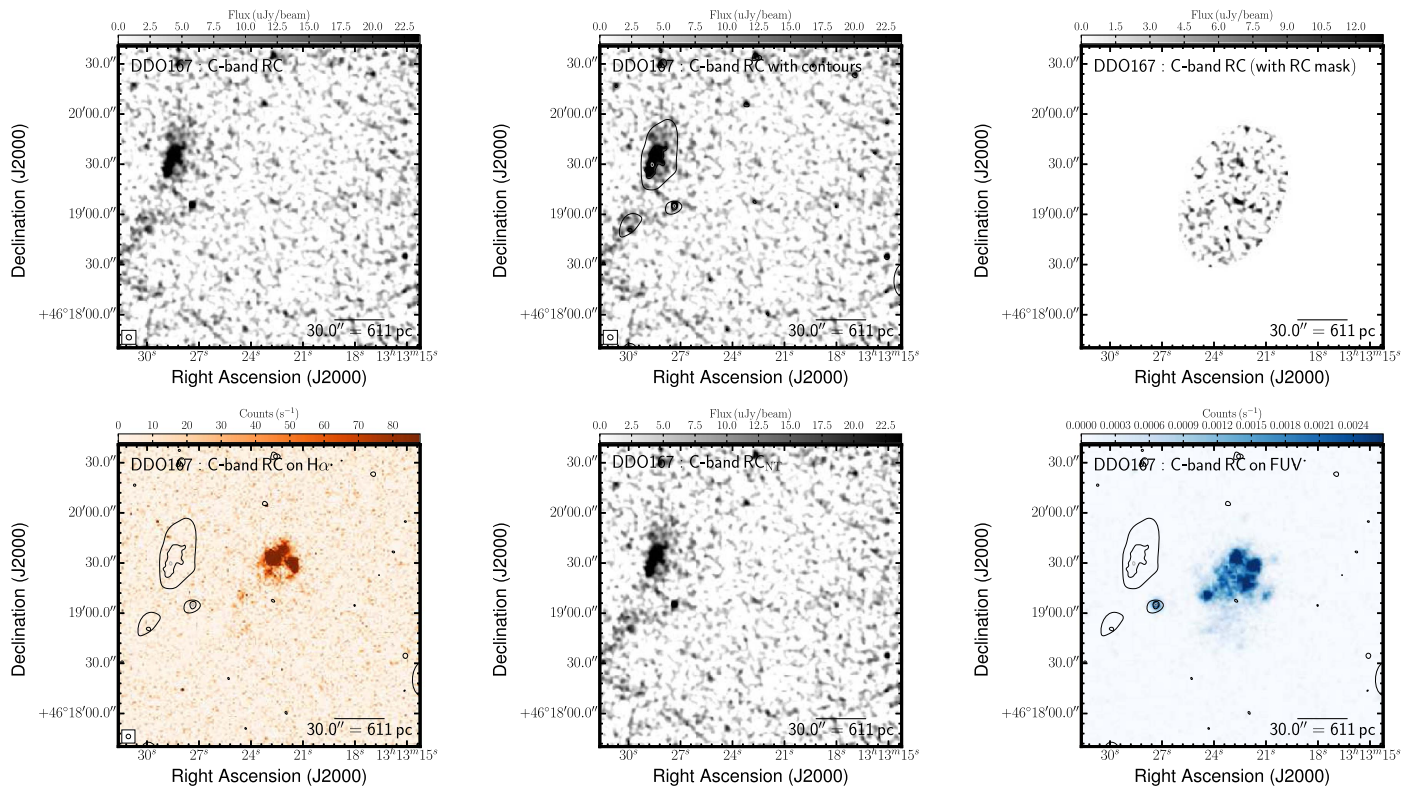


Figure 31. Multiwavelength coverage of DDO 167 displaying a $3'0 \times 3'0$ area. We show the total RC flux density at the native resolution (top left) and again with contours (top center). The RC contours are superposed on ancillary LITTLE THINGS images where possible: H α (middle left); RC $_{Nth}$ obtained by subtracting the expected RC $_{Th}$ based on the H α -RC $_{Th}$ scaling factor of Deeg et al. (1997) from the total RC; GALEX FUV (middle right); *Spitzer* 24 μ m (bottom left); *Spitzer* 70 μ m (bottom center); FUV+24 μ m-inferred SFRD from Leroy et al. (2012; bottom right). We also show the RC that was isolated by the RC-based masking technique (top right).

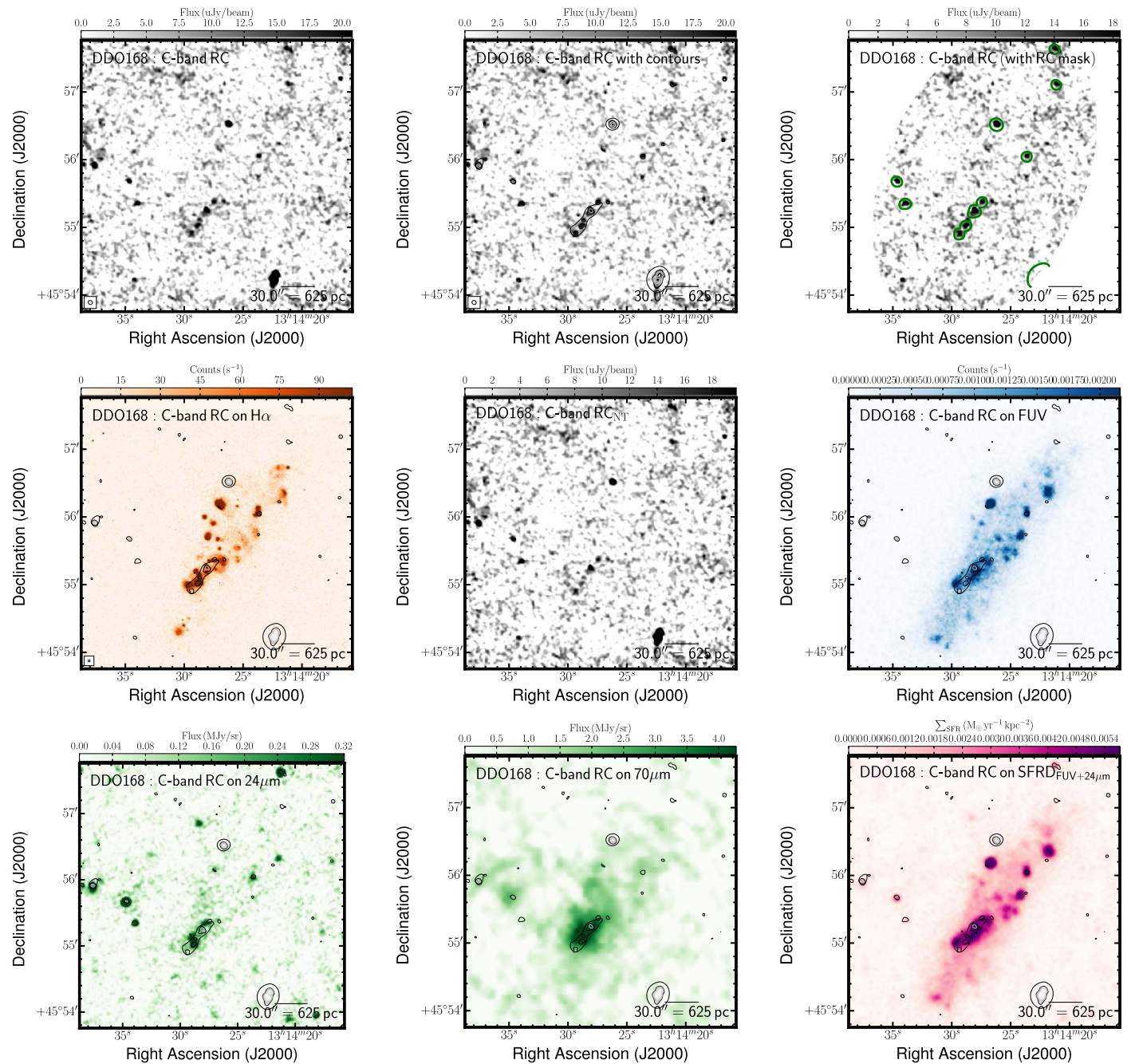


Figure 32. Multiwavelength coverage of DDO 168 displaying a $4'0 \times 4'0$ area. We show the total RC flux density at the native resolution (top left) and again with contours (top center). The RC contours are superposed on ancillary LITTLE THINGS images where possible: $H\alpha$ (middle left); RC_{Nth} obtained by subtracting the expected RC_{Th} based on the $H\alpha$ – RC_{Th} scaling factor of Deeg et al. (1997) from the total RC; *GALEX* FUV (middle right); *Spitzer* $24 \mu m$ (bottom left); *Spitzer* $70 \mu m$ (bottom center); FUV+ $24 \mu m$ -inferred SFRD from Leroy et al. (2012; bottom right). We also show the RC that was isolated by the RC-based masking technique (top right).

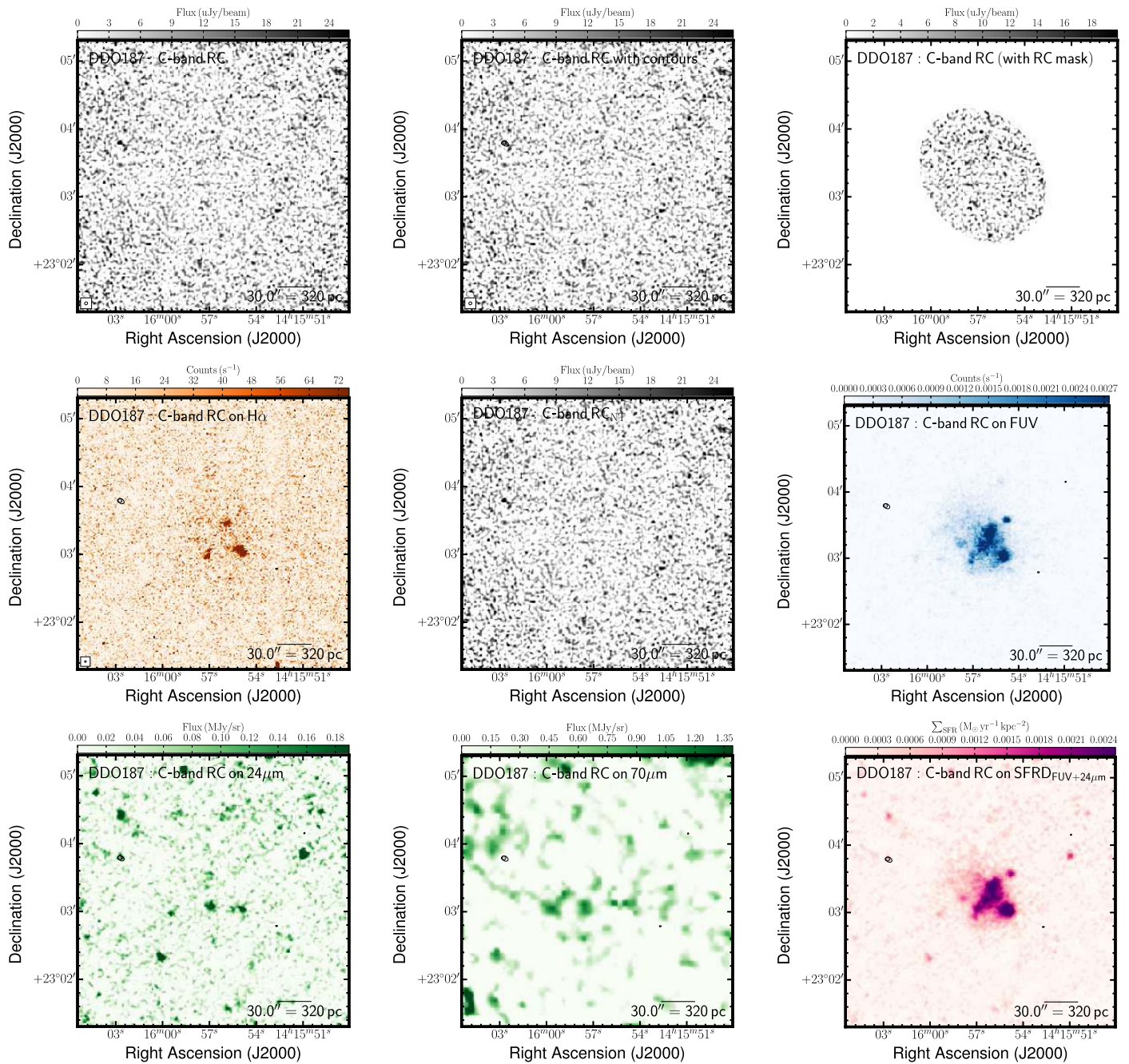


Figure 33. Multiwavelength coverage of DDO 187 displaying a $4'0 \times 4'0$ area. We show the total RC flux density at the native resolution (top left) and again with contours (top center). The RC contours are superposed on ancillary LITTLE THINGS images where possible: $H\alpha$ (middle left); RC_{Nth} obtained by subtracting the expected RC_{Th} based on the $H\alpha$ - RC_{Th} scaling factor of Deeg et al. (1997) from the total RC; *GALEX* FUV (middle right); *Spitzer* $24 \mu m$ (bottom left); *Spitzer* $70 \mu m$ (bottom center); FUV+ $24 \mu m$ -inferred SFRD from Leroy et al. (2012; bottom right). We also show the RC that was isolated by the RC-based masking technique (top right).

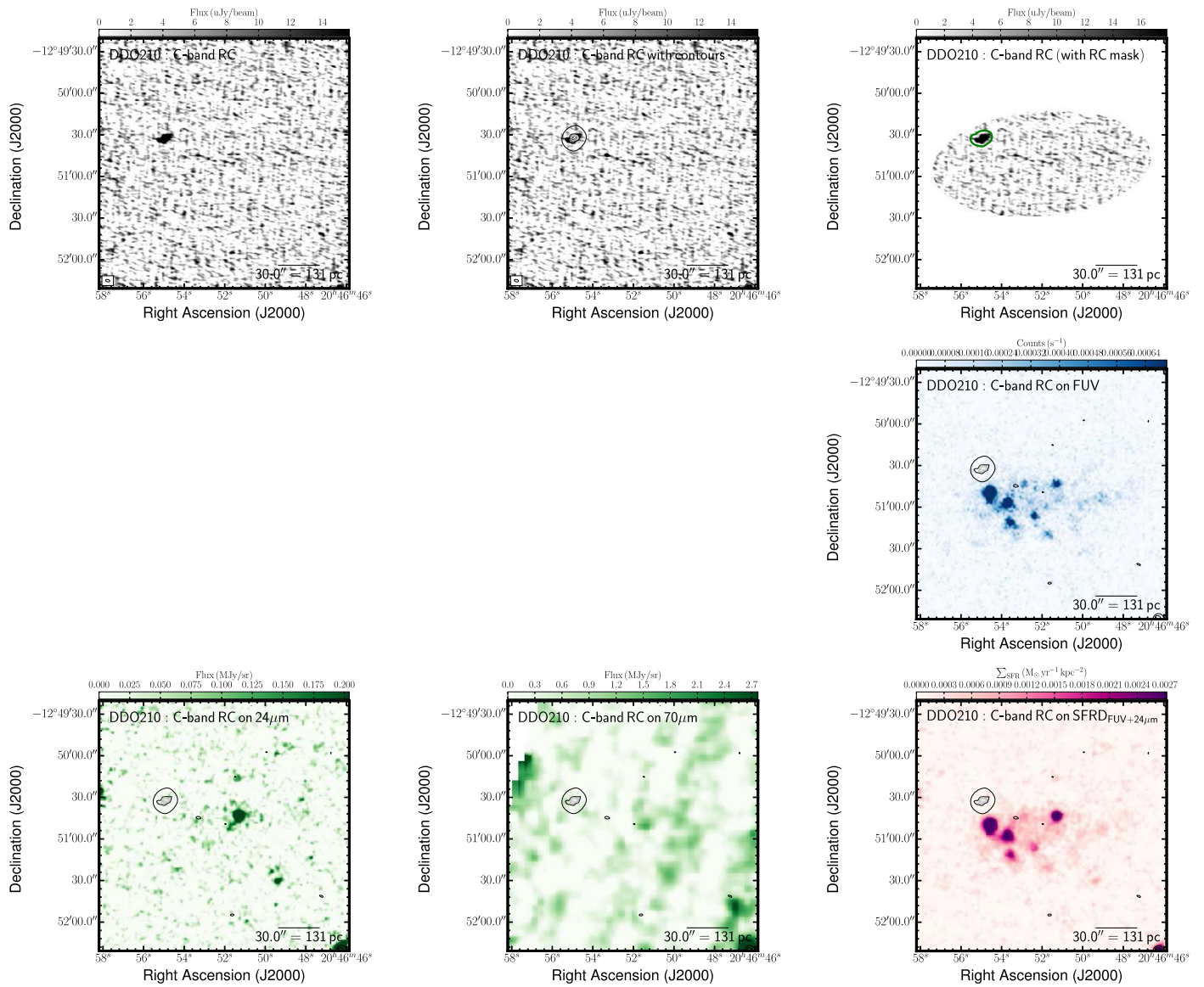


Figure 34. Multiwavelength coverage of DDO 210 displaying a $3'0 \times 3'0$ area. We show the total RC flux density at the native resolution (top left) and again with contours (top center). The RC contours are superposed on ancillary LITTLE THINGS images where possible: $H\alpha$ (middle left); RC_{Nth} obtained by subtracting the expected RC_{Th} based on the $H\alpha$ - RC_{Th} scaling factor of Deeg et al. (1997) from the total RC; *GALEX* FUV (middle right); *Spitzer* $24 \mu m$ (bottom left); *Spitzer* $70 \mu m$ (bottom center); FUV+ $24 \mu m$ -inferred SFRD from Leroy et al. (2012; bottom right). We also show the RC that was isolated by the RC-based masking technique (top right).

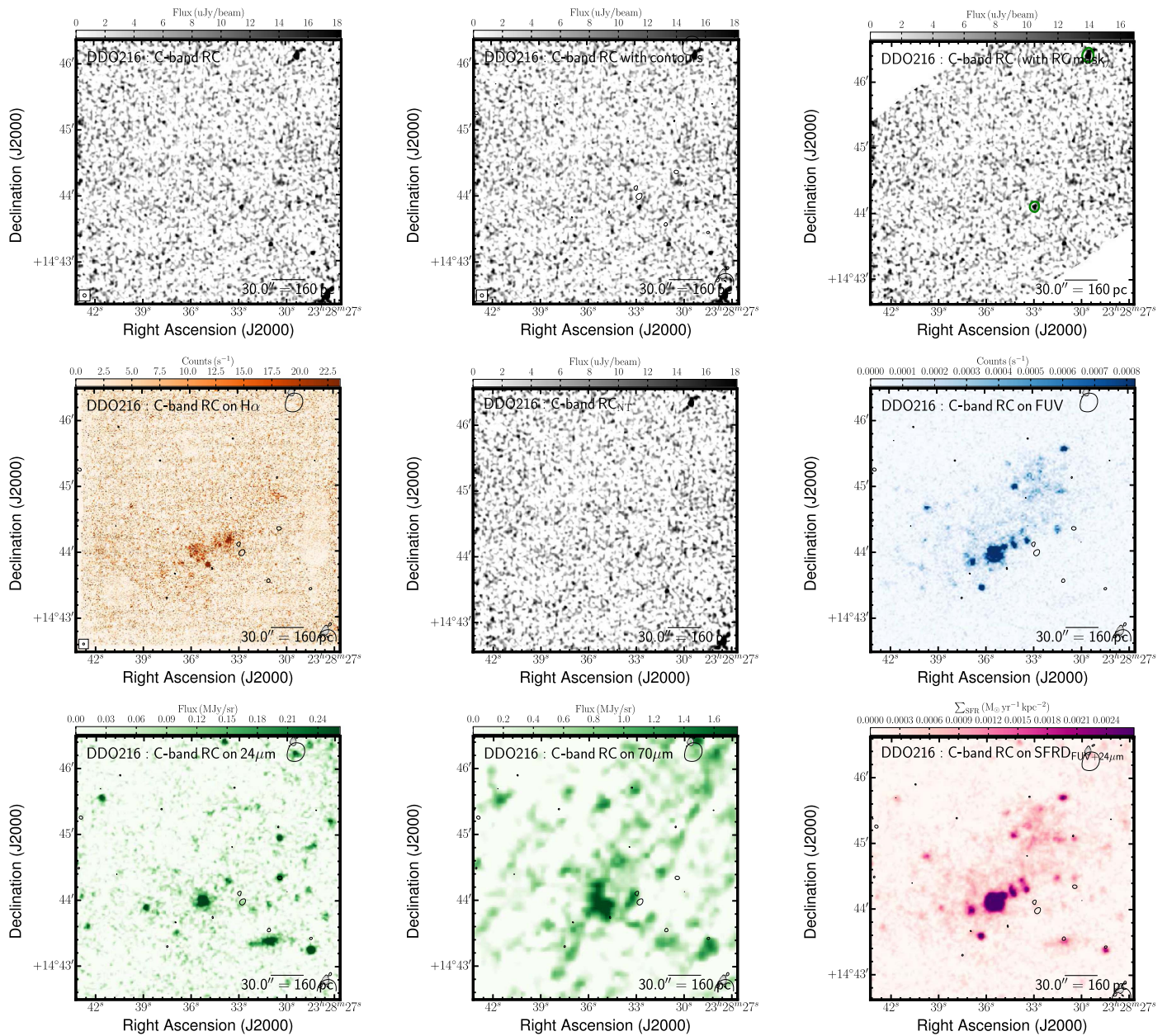


Figure 35. Multiwavelength coverage of DDO 216 displaying a 3.7×3.7 area. We show the total RC flux density at the native resolution (top left) and again with contours (top center). The RC contours are superposed on ancillary LITTLE THINGS images where possible: $H\alpha$ (middle left); RC_{NII} obtained by subtracting the expected RC_{Th} based on the $H\alpha$ - RC_{Th} scaling factor of Deeg et al. (1997) from the total RC; *GALEX* FUV (middle right); *Spitzer* $24 \mu m$ (bottom left); *Spitzer* $70 \mu m$ (bottom center); FUV+ $24 \mu m$ -inferred SFRD from Leroy et al. (2012; bottom right). We also show the RC that was isolated by the RC-based masking technique (top right).

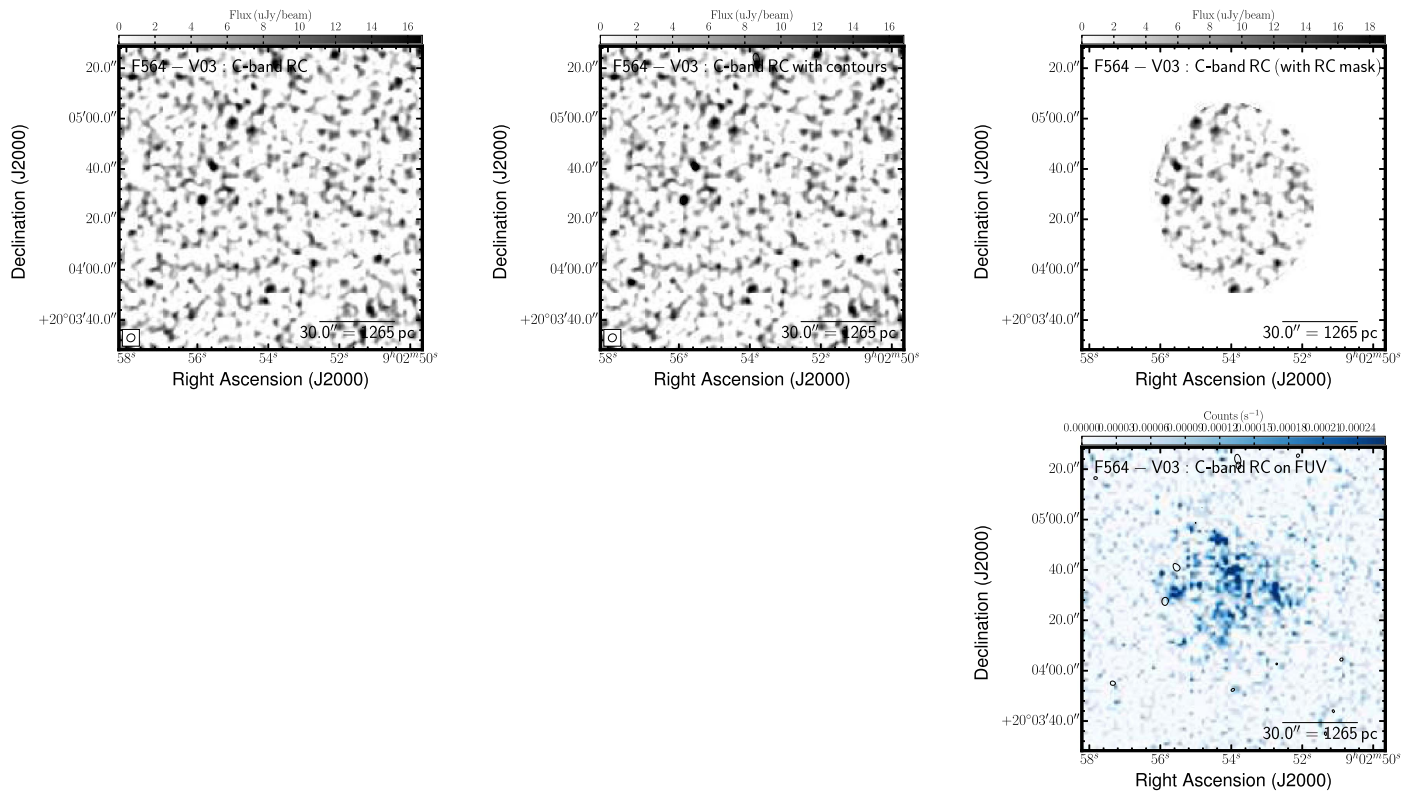


Figure 36. Multiwavelength coverage of F564-V03 displaying a $2'0 \times 2'0$ area. We show the total RC flux density at the native resolution (top left) and again with contours (top center). The RC contours are superposed on ancillary LITTLE THINGS images where possible: $H\alpha$ (middle left); RC_{Nth} obtained by subtracting the expected RC_{Th} based on the $H\alpha$ - RC_{Th} scaling factor of Deeg et al. (1997) from the total RC; *GALEX* FUV (middle right); *Spitzer* $24 \mu m$ (bottom left); *Spitzer* $70 \mu m$ (bottom center); FUV+ $24 \mu m$ -inferred SFRD from Leroy et al. (2012; bottom right). We also show the RC that was isolated by the RC-based masking technique (top right).

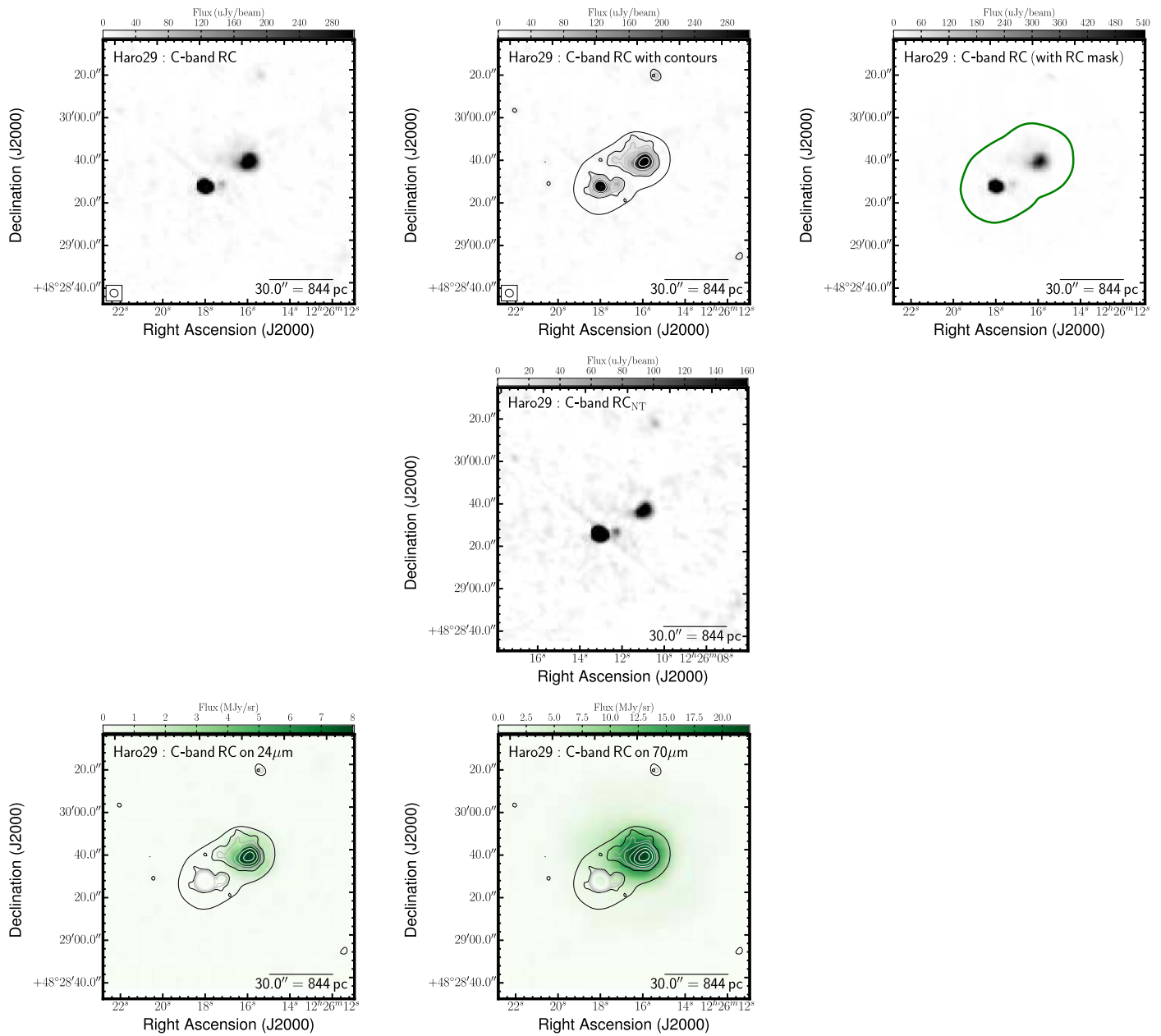


Figure 37. Multiwavelength coverage of Haro 29 displaying a $2'0 \times 2'0$ area. We show the total RC flux density at the native resolution (top left) and again with contours (top center). The RC contours are superposed on ancillary LITTLE THINGS images where possible: $H\alpha$ (middle left); RC_{NTh} obtained by subtracting the expected RC_{Th} based on the $H\alpha$ -RC_{Th} scaling factor of Deeg et al. (1997) from the total RC; GALEX FUV (middle right); *Spitzer* 24 μm (bottom left); *Spitzer* 70 μm (bottom center); FUV+24 μm-inferred SFRD from Leroy et al. (2012; bottom right). We also show the RC that was isolated by the RC-based masking technique (top right).

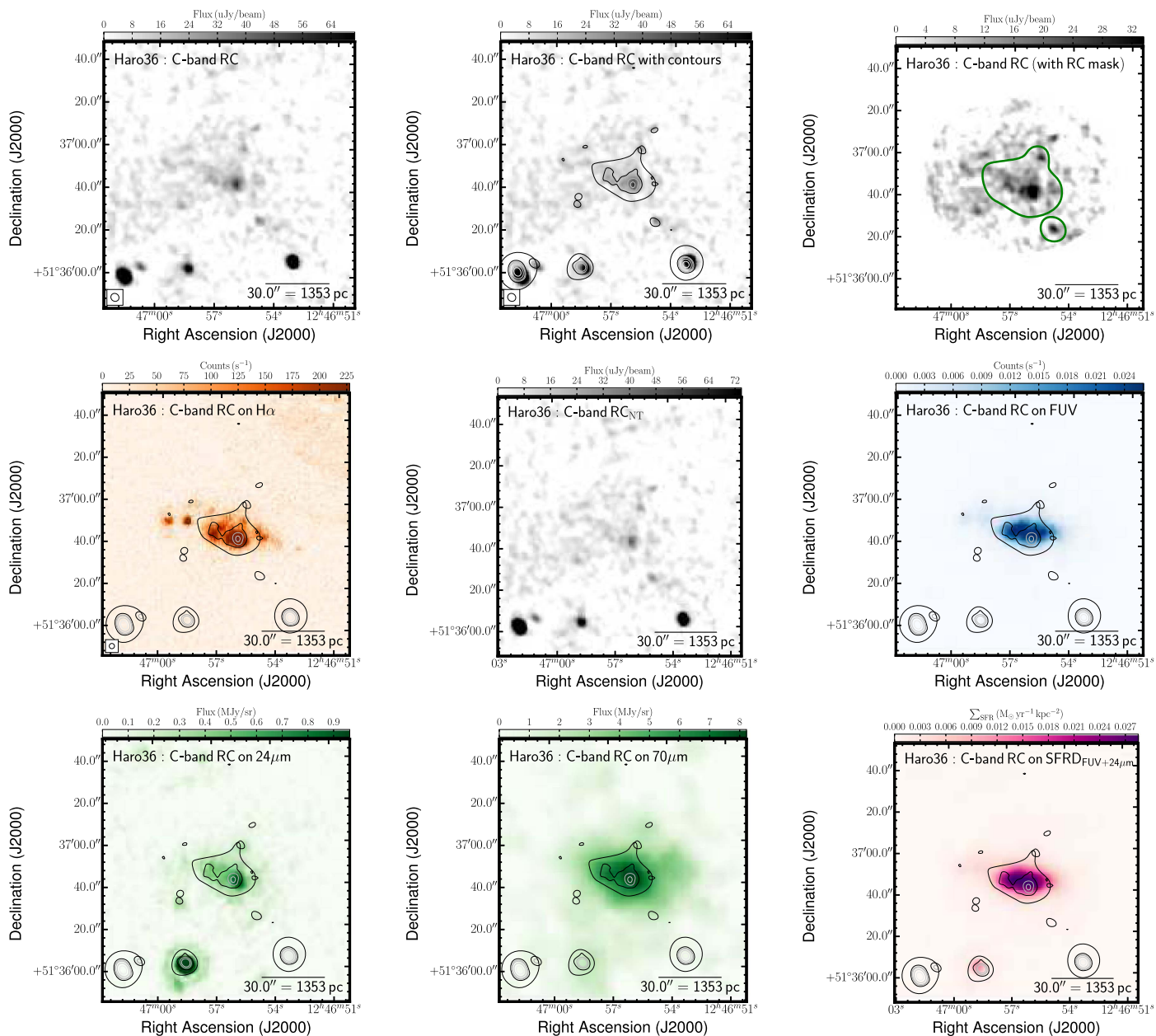


Figure 38. Multiwavelength coverage of Haro 36 displaying a $2'0 \times 2'0$ area. We show the total RC flux density at the native resolution (top left) and again with contours (top center). The RC contours are superposed on ancillary LITTLE THINGS images where possible: $H\alpha$ (middle left); RC_{Nth} obtained by subtracting the expected RC_{Th} based on the $H\alpha$ - RC_{Th} scaling factor of Deeg et al. (1997) from the total RC; *GALEX* FUV (middle right); *Spitzer* $24 \mu m$ (bottom left); *Spitzer* $70 \mu m$ (bottom center); FUV+ $24 \mu m$ -inferred SFRD from Leroy et al. (2012; bottom right). We also show the RC that was isolated by the RC-based masking technique (top right).

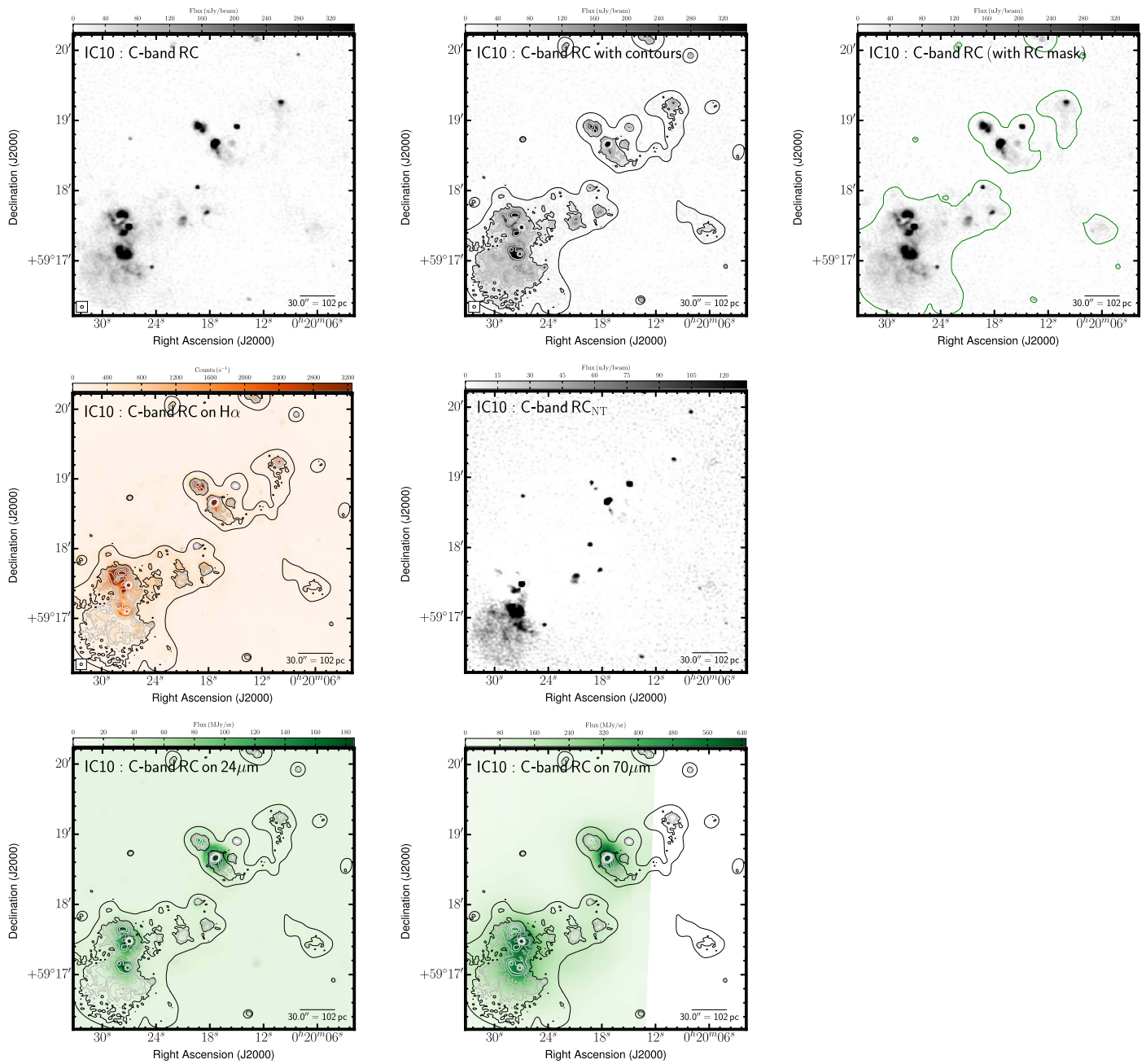


Figure 39. Multiwavelength coverage of IC 10 displaying a $4'0 \times 4'0$ area. We show the total RC flux density at the native resolution (top left) and again with contours (top center). The RC contours are superposed on ancillary LITTLE THINGS images where possible: H α (middle left); RC_{Nth} obtained by subtracting the expected RC_{Th} based on the H α -RC_{Th} scaling factor of Deeg et al. (1997) from the total RC; GALEX FUV (middle right); Spitzer 24 μ m (bottom left); Spitzer 70 μ m (bottom center); FUV+24 μ m-inferred SFRD from Leroy et al. (2012; bottom right). We also show the RC that was isolated by the RC-based masking technique (top right).

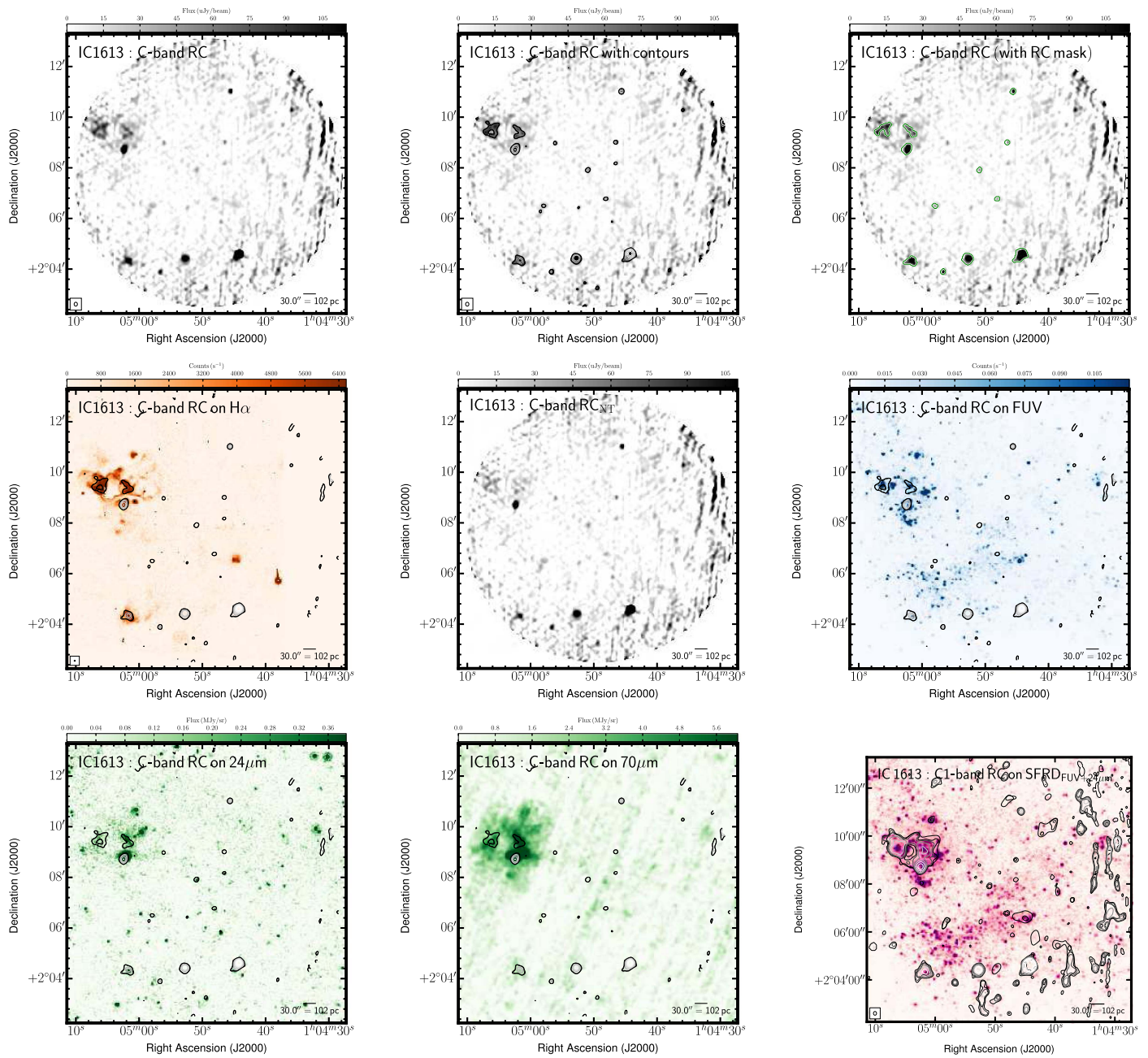


Figure 40. Multiwavelength coverage of IC 1613 displaying a $11\prime.1 \times 11\prime.1$ area. We show the total RC flux density at the native resolution (top left) and again with contours (top center). The RC contours are superposed on ancillary LITTLE THINGS images where possible: $H\alpha$ (middle left); RC_{Nth} obtained by subtracting the expected RC_{Th} based on the $H\alpha$ - RC_{Th} scaling factor of Deeg et al. (1997) from the total RC; *GALEX* FUV (middle right); *Spitzer* $24\ \mu\text{m}$ (bottom left); *Spitzer* $70\ \mu\text{m}$ (bottom center); FUV+ $24\ \mu\text{m}$ -inferred SFRD from Leroy et al. (2012; bottom right). We also show the RC that was isolated by the RC-based masking technique (top right).

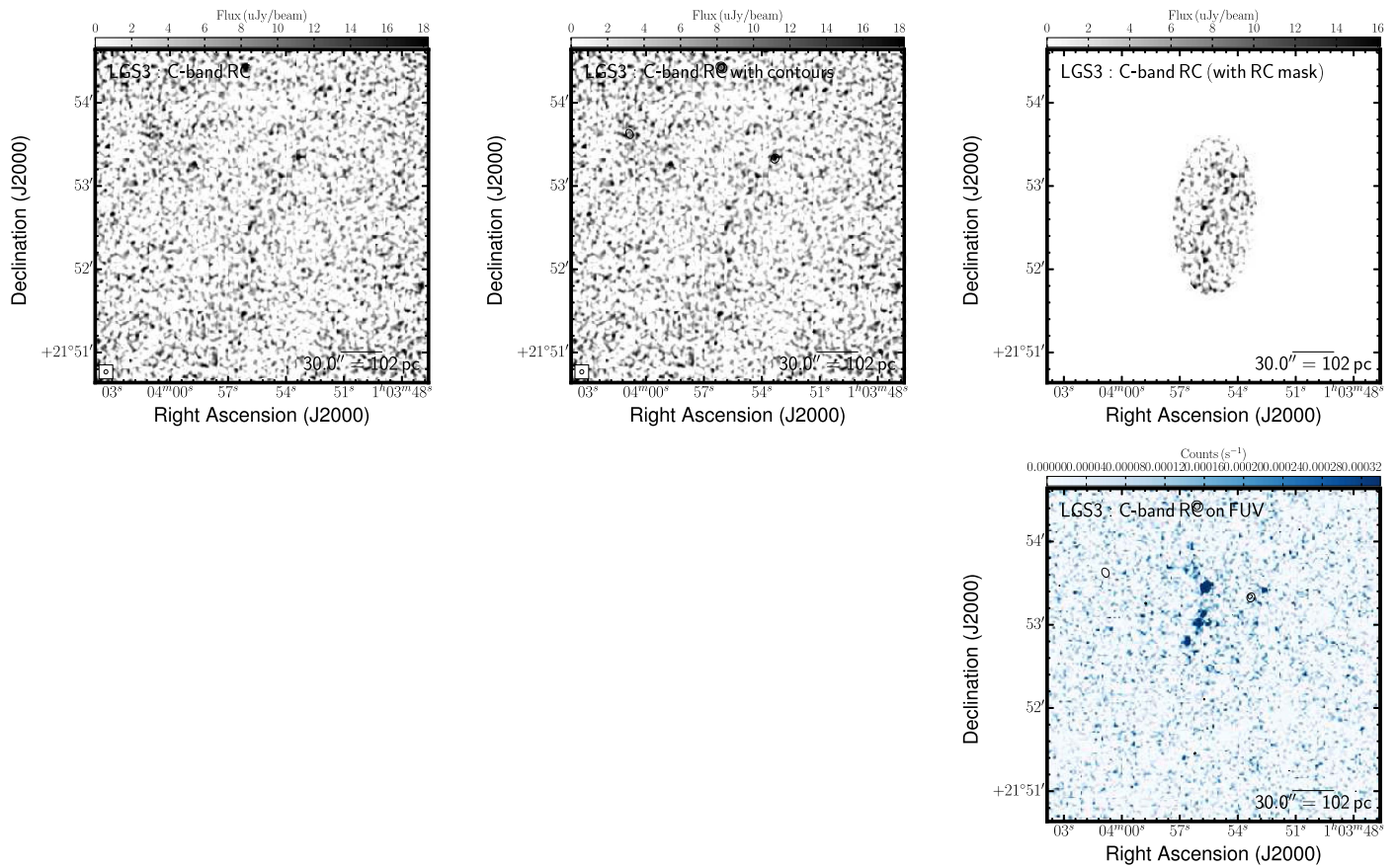


Figure 41. Multiwavelength coverage of LGS 3 displaying a $4'0 \times 4'0$ area. We show the total RC flux density at the native resolution (top left) and again with contours (top center). The RC contours are superposed on ancillary LITTLE THINGS images where possible: $H\alpha$ (middle left); RC_{Nth} obtained by subtracting the expected RC_{Th} based on the $H\alpha$ - RC_{Th} scaling factor of Deeg et al. (1997) from the total RC; *GALEX* FUV (middle right); *Spitzer* $24 \mu m$ (bottom left); *Spitzer* $70 \mu m$ (bottom center); FUV+ $24 \mu m$ -inferred SFRD from Leroy et al. (2012; bottom right). We also show the RC that was isolated by the RC-based masking technique (top right).

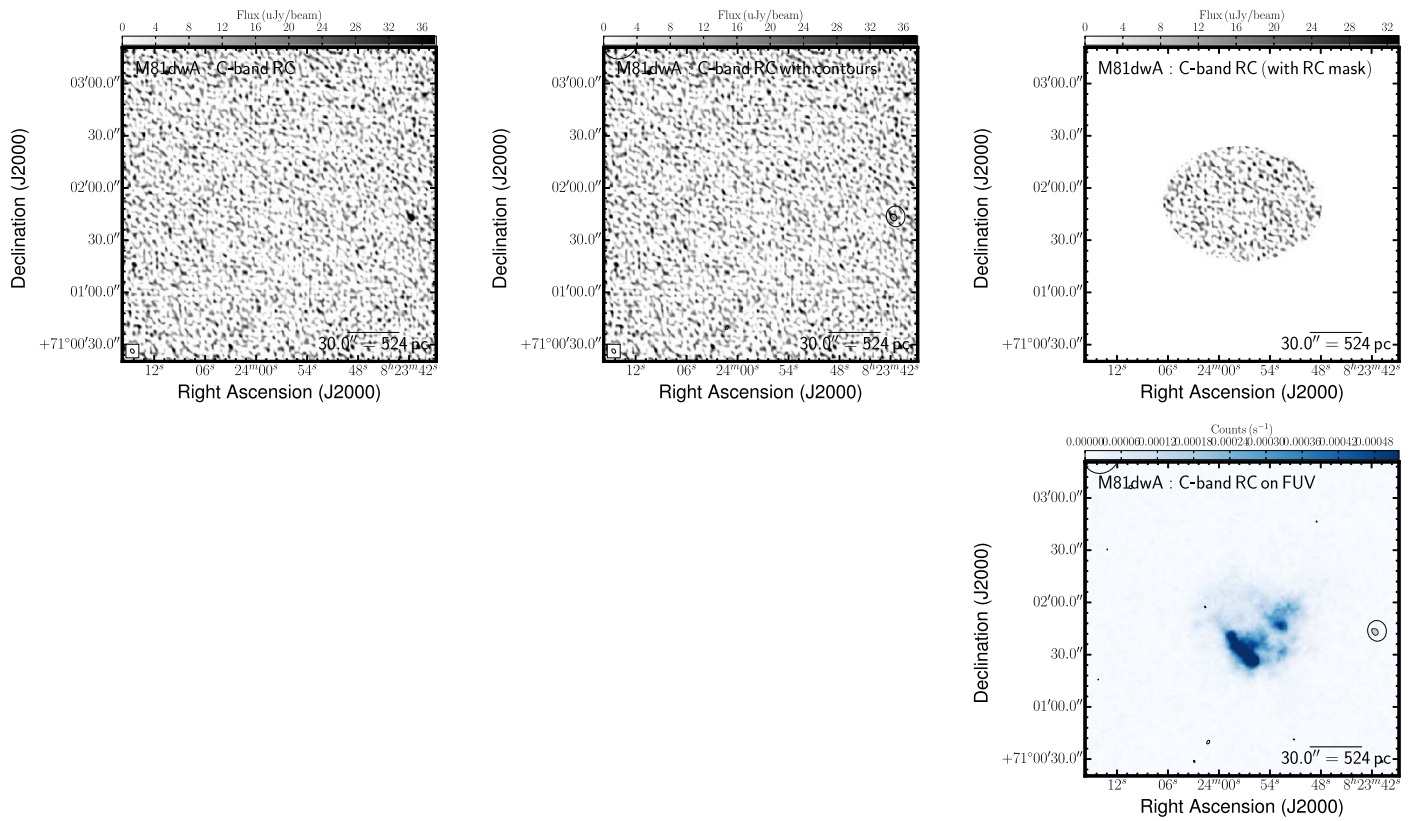


Figure 42. Multiwavelength coverage of M81 dwA displaying a $3'0 \times 3'0$ area. We show the total RC flux density at the native resolution (top left) and again with contours (top center). The RC contours are superposed on ancillary LITTLE THINGS images where possible: $H\alpha$ (middle left); RC_{Nth} obtained by subtracting the expected RC_{Th} based on the $H\alpha-RC_{Th}$ scaling factor of Deeg et al. (1997) from the total RC; *GALEX* FUV (middle right); *Spitzer* $24 \mu m$ (bottom left); *Spitzer* $70 \mu m$ (bottom center); FUV+ $24 \mu m$ -inferred SFRD from Leroy et al. (2012; bottom right). We also show the RC that was isolated by the RC-based masking technique (top right).

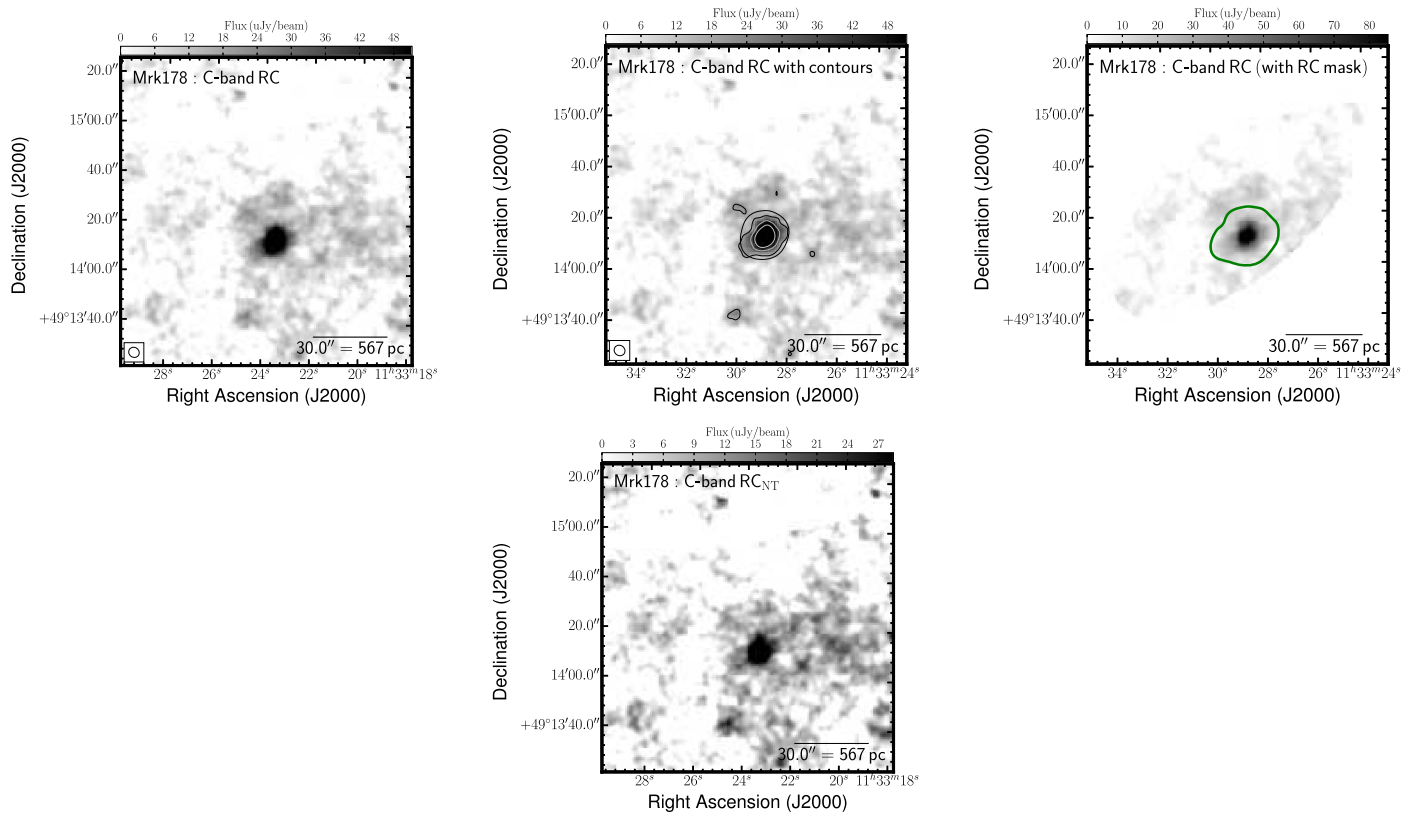


Figure 43. Multiwavelength coverage of Mrk 178 displaying a $2'0 \times 2'0$ area. We show the total RC flux density at the native resolution (top left) and again with contours (top center). The RC contours are superposed on ancillary LITTLE THINGS images where possible: $H\alpha$ (middle left); RC_{Nth} obtained by subtracting the expected RC_{Th} based on the $H\alpha$ – RC_{Th} scaling factor of Deeg et al. (1997) from the total RC; *GALEX* FUV (middle right); *Spitzer* 24 μm (bottom left); *Spitzer* 70 μm (bottom center); FUV+24 μm -inferred SFRD from Leroy et al. (2012; bottom right). We also show the RC that was isolated by the RC-based masking technique (top right).

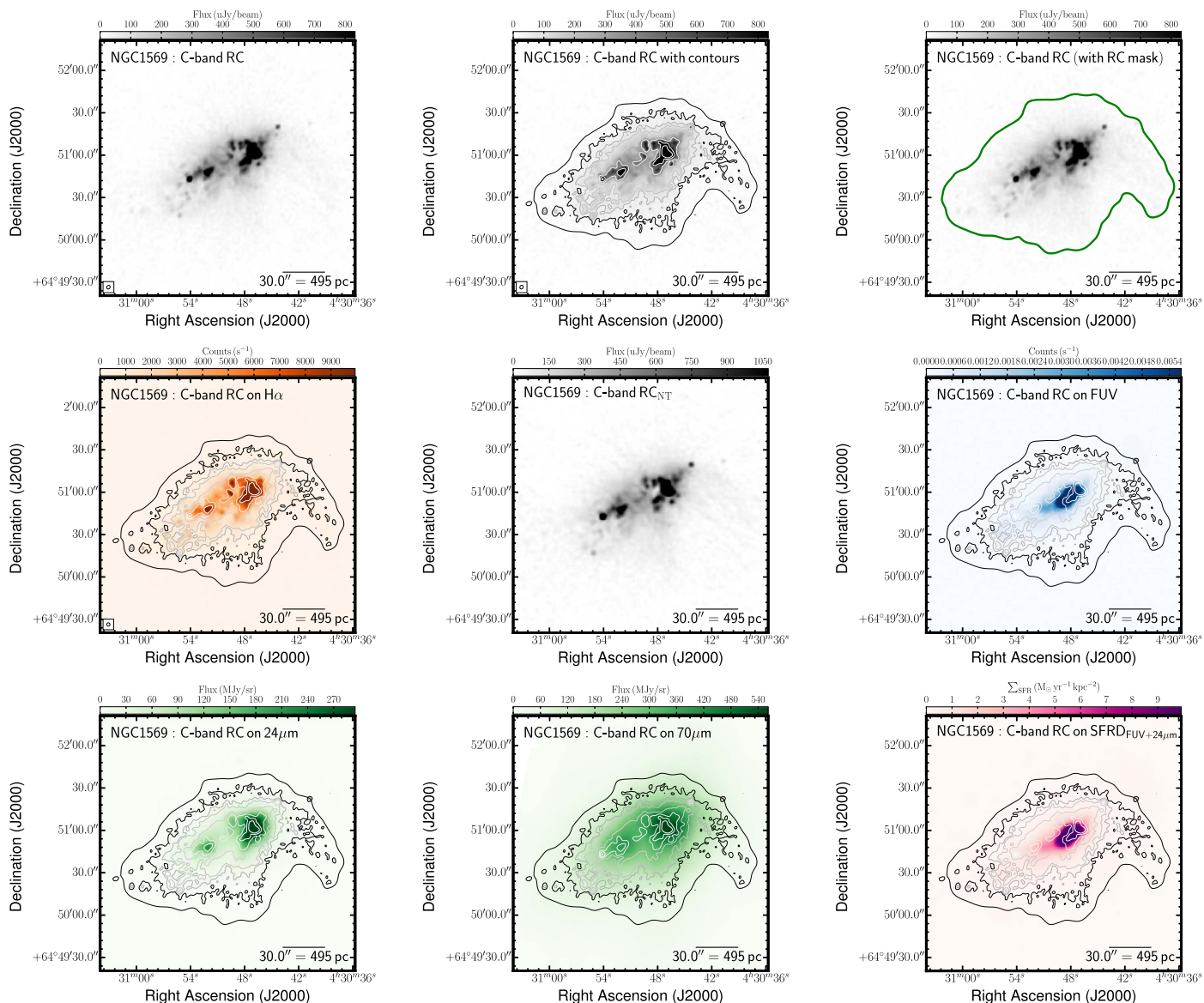


Figure 44. Multiwavelength coverage of NGC 1569 displaying a $3'0 \times 3'0$ area. We show the total RC flux density at the native resolution (top left) and again with contours (top center). The RC contours are superposed on ancillary LITTLE THINGS images where possible: $H\alpha$ (middle left); RC_{NTh} obtained by subtracting the expected RC_{Th} based on the $H\alpha$ - RC_{Th} scaling factor of Deeg et al. (1997) from the total RC; *GALEX* FUV (middle right); *Spitzer* $24 \mu m$ (bottom left); *Spitzer* $70 \mu m$ (bottom center); FUV+ $24 \mu m$ -inferred SFRD from Leroy et al. (2012; bottom right). We also show the RC that was isolated by the RC-based masking technique (top right).

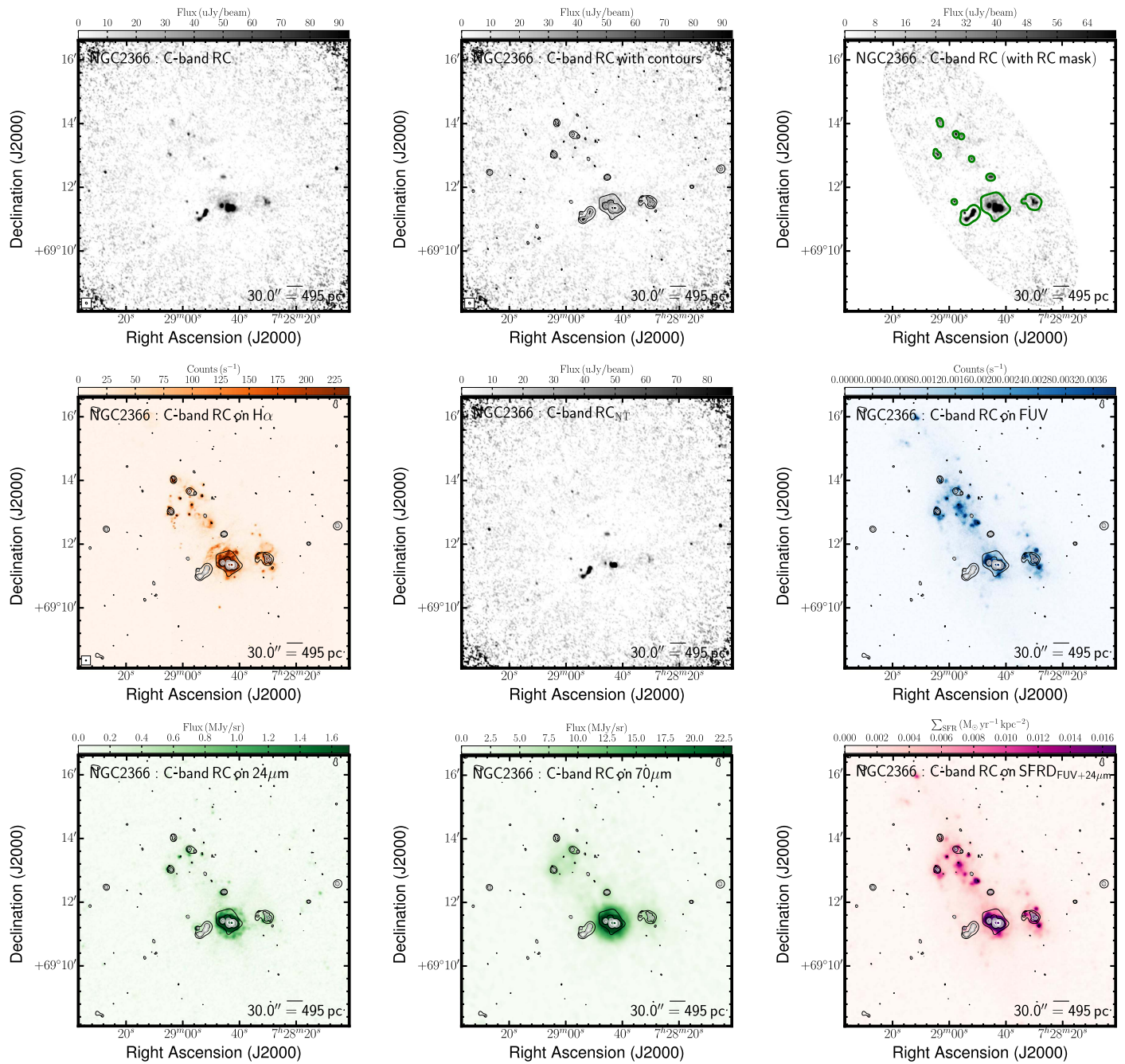


Figure 45. Multiwavelength coverage of NGC 2366 displaying a $8'.5 \times 8'.5$ area. We show the total RC flux density at the native resolution (top left) and again with contours (top center). The RC contours are superposed on ancillary LITTLE THINGS images where possible: $H\alpha$ (middle left); RC_{Nth} obtained by subtracting the expected RC_{Th} based on the $H\alpha$ – RC_{Th} scaling factor of Deeg et al. (1997) from the total RC; *GALEX* FUV (middle right); *Spitzer* $24 \mu m$ (bottom left); *Spitzer* $70 \mu m$ (bottom center); FUV+ $24 \mu m$ -inferred SFRD from Leroy et al. (2012; bottom right). We also show the RC that was isolated by the RC-based masking technique (top right).

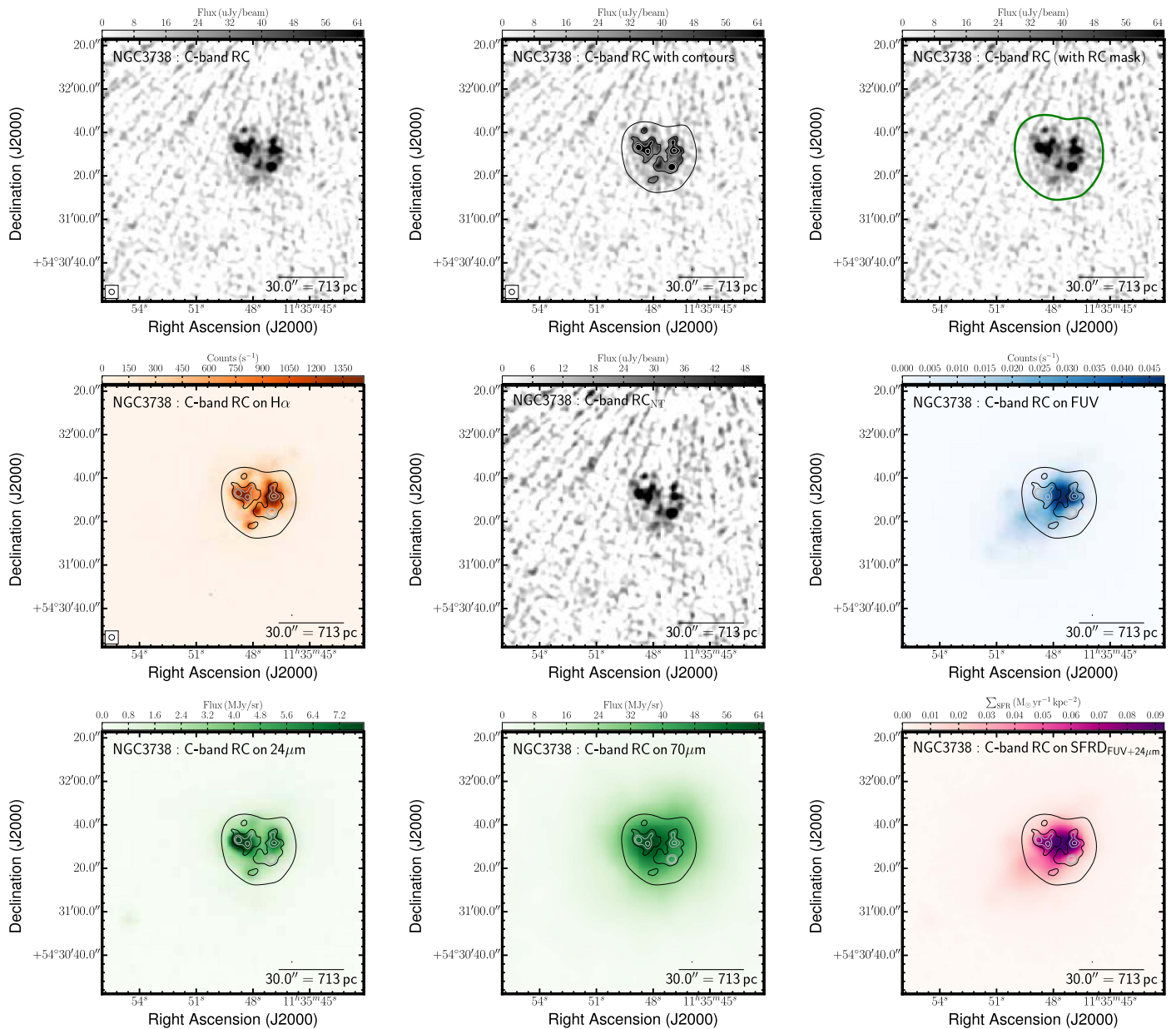


Figure 46. Multiwavelength coverage of NGC 3738 displaying a $2'0'' \times 2'0''$ area. We show the total RC flux density at the native resolution (top left) and again with contours (top center). The RC contours are superposed on ancillary LITTLE THINGS images where possible: $H\alpha$ (middle left); RC_{NTH} obtained by subtracting the expected RC_{Th} based on the $H\alpha$ - RC_{Th} scaling factor of Deeg et al. (1997) from the total RC; *GALEX* FUV (middle right); *Spitzer* $24 \mu m$ (bottom left); *Spitzer* $70 \mu m$ (bottom center); FUV+ $24 \mu m$ -inferred SFRD from Leroy et al. (2012; bottom right). We also show the RC that was isolated by the RC-based masking technique (top right).

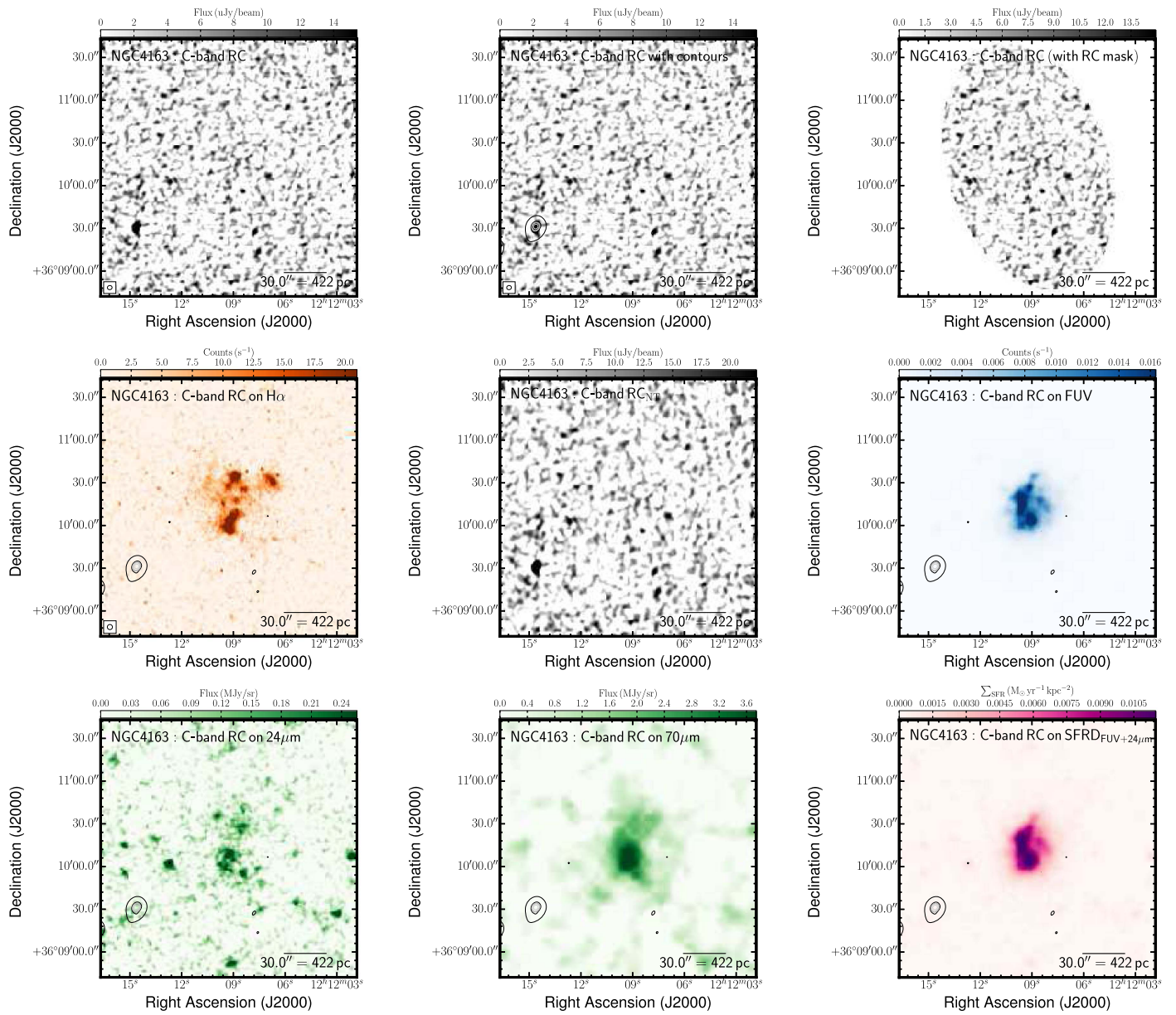


Figure 47. Multiwavelength coverage of NGC 4163 displaying a $3'0 \times 3'0$ area. We show the total RC flux density at the native resolution (top left) and again with contours (top center). The RC contours are superposed on ancillary LITTLE THINGS images where possible: $H\alpha$ (middle left); RC_{Nth} obtained by subtracting the expected RC_{Th} based on the $H\alpha$ - RC_{Th} scaling factor of Deeg et al. (1997) from the total RC; *GALEX* FUV (middle right); *Spitzer* $24 \mu m$ (bottom left); *Spitzer* $70 \mu m$ (bottom center); FUV+ $24 \mu m$ -inferred SFRD from Leroy et al. (2012; bottom right). We also show the RC that was isolated by the RC-based masking technique (top right).

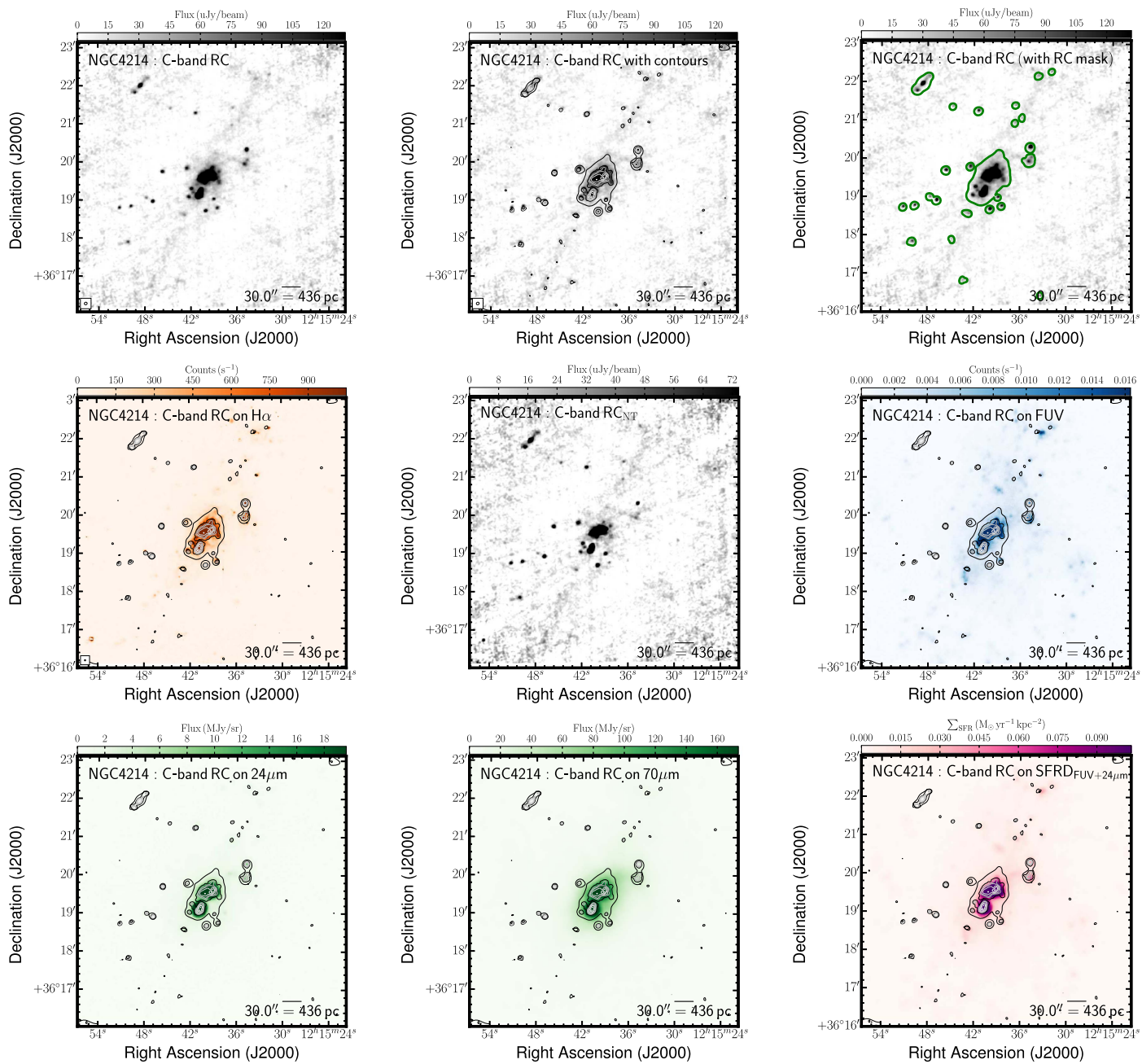


Figure 48. Multiwavelength coverage of NGC 4214 displaying a $7'0 \times 7'0$ area. We show the total RC flux density at the native resolution (top left) and again with contours (top center). The RC contours are superposed on ancillary LITTLE THINGS images where possible: $H\alpha$ (middle left); RC_{Nth} obtained by subtracting the expected RC_{Th} based on the $H\alpha$ - RC_{Th} scaling factor of Deeg et al. (1997) from the total RC; *GALEX* FUV (middle right); *Spitzer* $24 \mu m$ (bottom left); *Spitzer* $70 \mu m$ (bottom center); FUV+ $24 \mu m$ -inferred SFRD from Leroy et al. (2012; bottom right). We also show the RC that was isolated by the RC-based masking technique (top right).

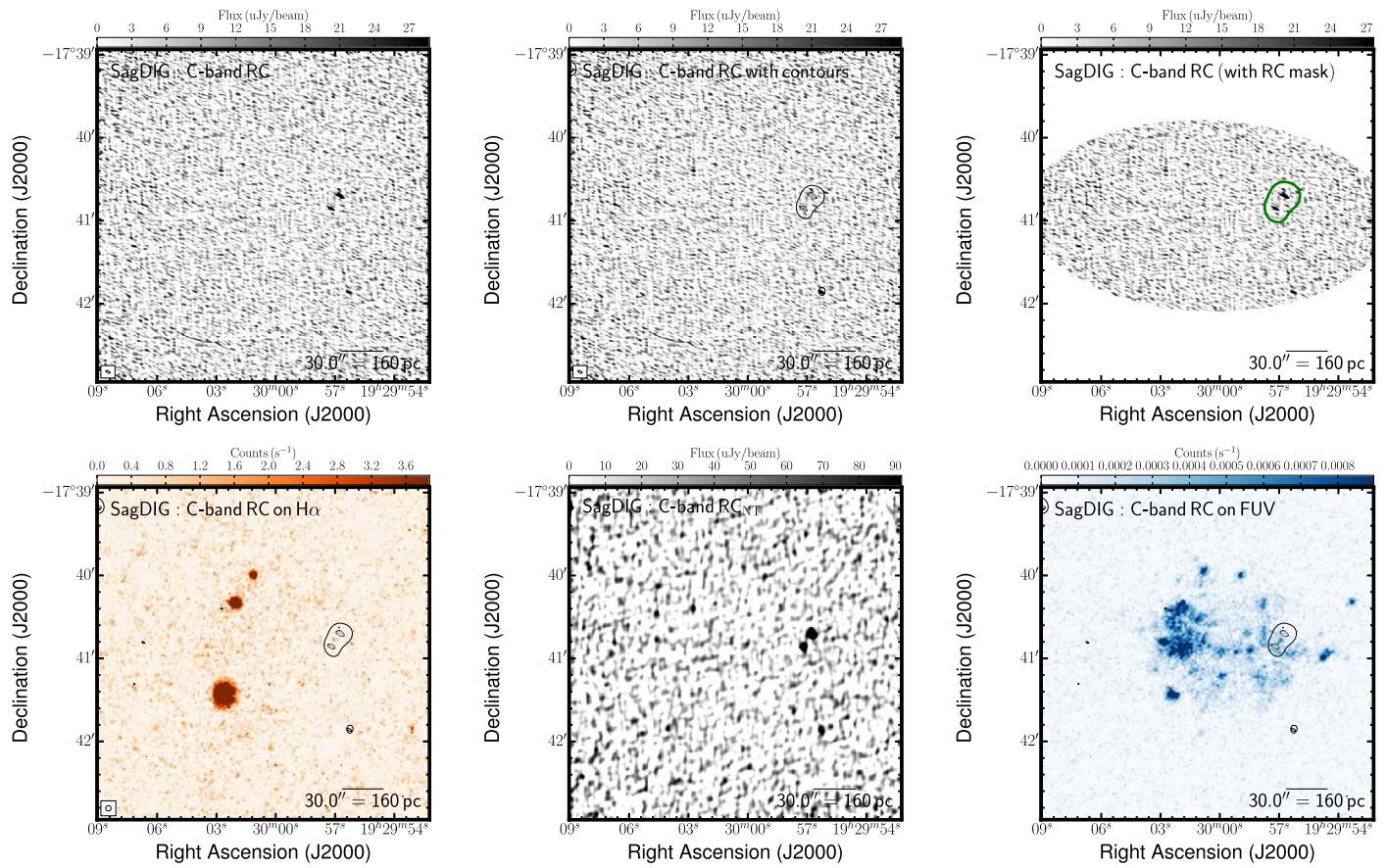


Figure 49. Multiwavelength coverage of Sag DIG displaying a 4'0" \times 4'0" area. We show the total RC flux density at the native resolution (top left) and again with contours (top center). The RC contours are superposed on ancillary LITTLE THINGS images where possible: H α (middle left); RC_{N th} obtained by subtracting the expected RC_{Th} based on the H α -RC_{Th} scaling factor of Deeg et al. (1997) from the total RC; GALEX FUV (middle right); Spitzer 24 μm (bottom left); Spitzer 70 μm (bottom center); FUV+24 μm -inferred SFRD from Leroy et al. (2012; bottom right). We also show the RC that was isolated by the RC-based masking technique (top right).

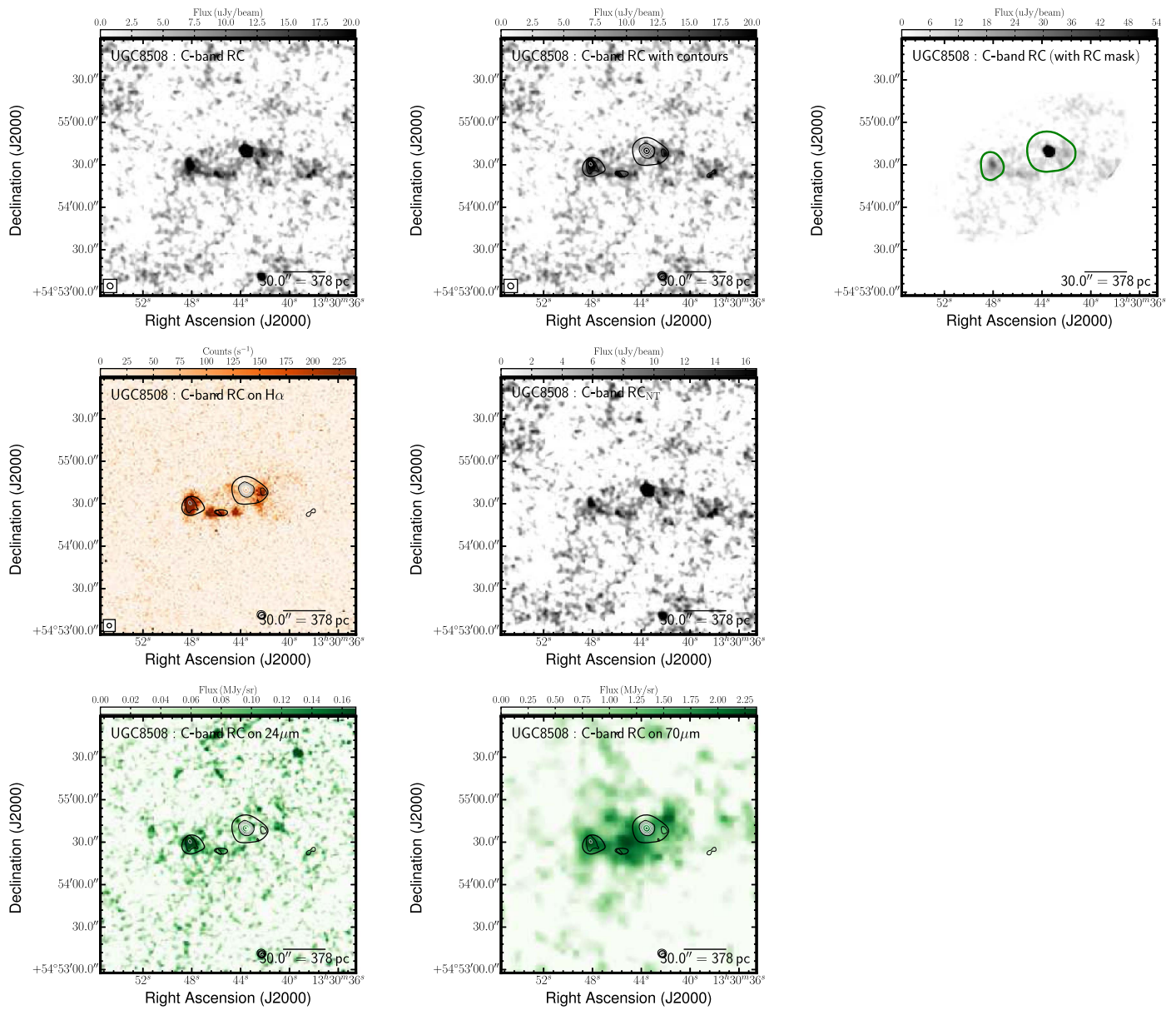


Figure 50. Multiwavelength coverage of UGC 8508 displaying a $3' \times 3'$ area. We show the total RC flux density at the native resolution (top left) and again with contours (top center). The RC contours are superposed on ancillary LITTLE THINGS images where possible: $H\alpha$ (middle left); RC_{Nth} obtained by subtracting the expected RC_{Th} based on the $H\alpha$ - RC_{Th} scaling factor of Deeg et al. (1997) from the total RC; *GALEX* FUV (middle right); *Spitzer* $24 \mu m$ (bottom left); *Spitzer* $70 \mu m$ (bottom center); FUV+ $24 \mu m$ -inferred SFRD from Leroy et al. (2012; bottom right). We also show the RC that was isolated by the RC-based masking technique (top right).

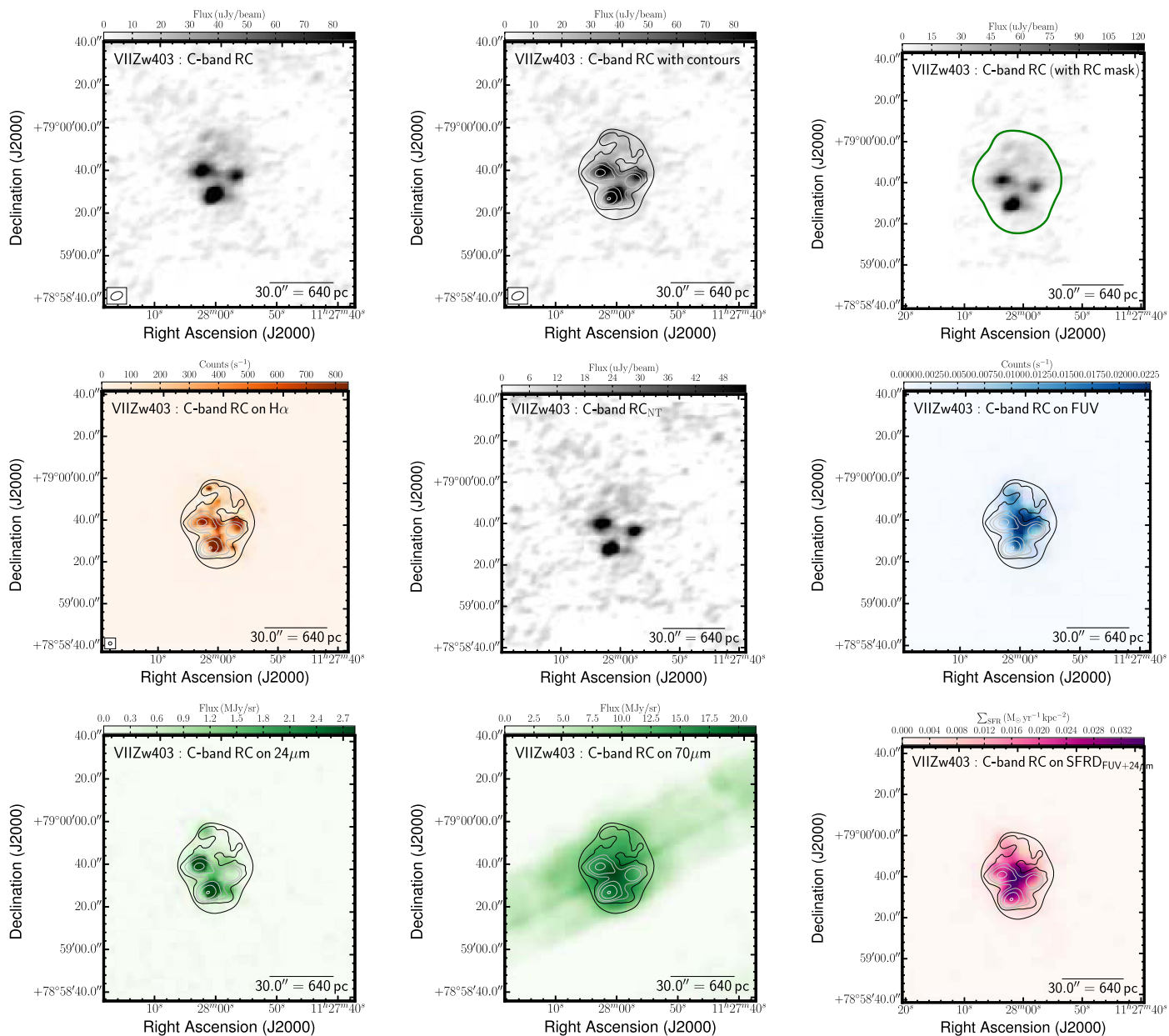


Figure 51. Multiwavelength coverage of VII Zw 403 displaying a $2.6' \times 2.6'$ area. We show the total RC flux density at the native resolution (top left) and again with contours (top center). The RC contours are superposed on ancillary LITTLE THINGS images where possible: $H\alpha$ (middle left); RC_{Nth} obtained by subtracting the expected RC_{Th} based on the $H\alpha$ - RC_{Th} scaling factor of Deeg et al. (1997) from the total RC; *GALEX* FUV (middle right); *Spitzer* $24 \mu m$ (bottom left); *Spitzer* $70 \mu m$ (bottom center); FUV+ $24 \mu m$ -inferred SFRD from Leroy et al. (2012; bottom right). We also show the RC that was isolated by the RC-based masking technique (top right).

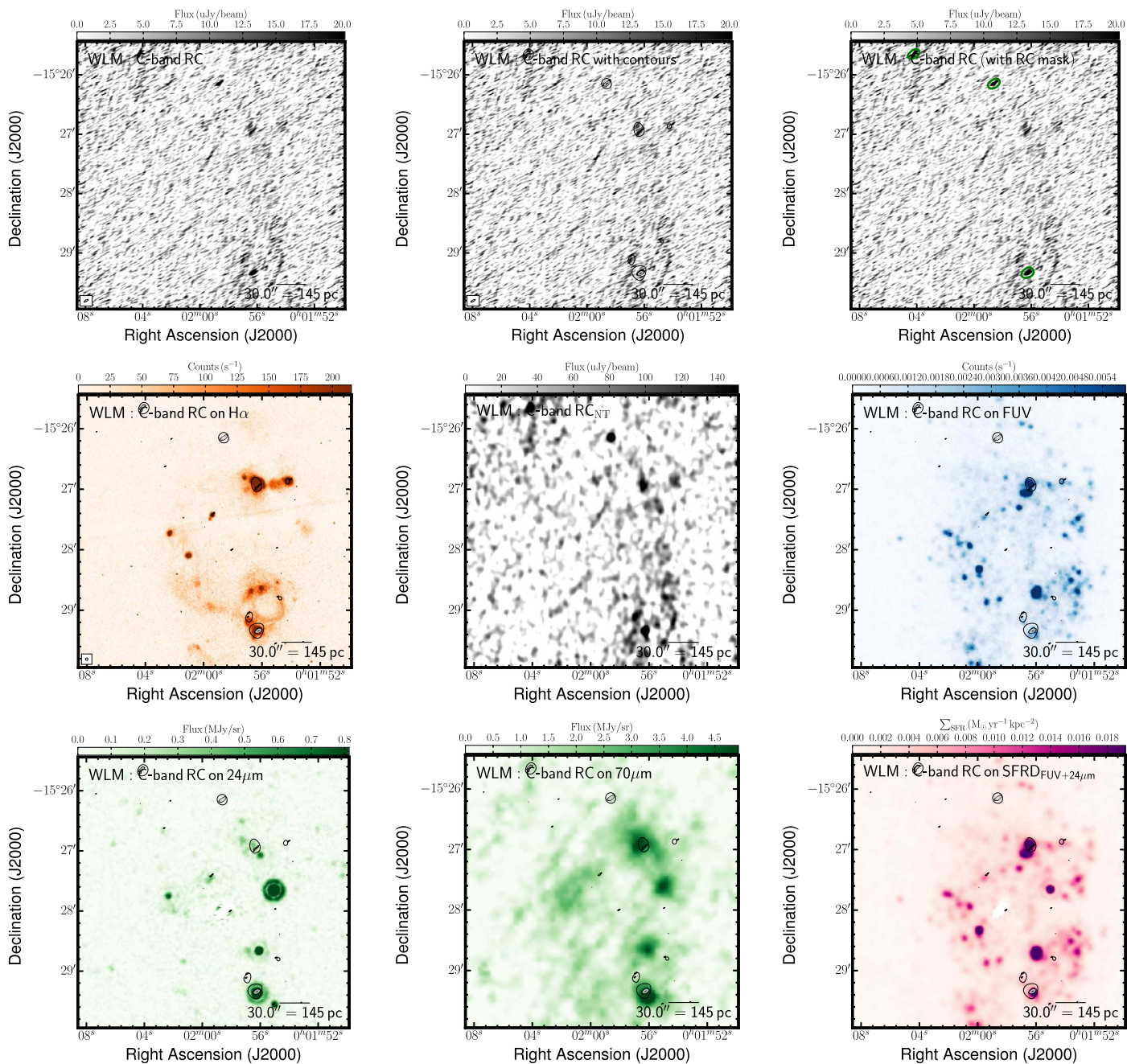


Figure 52. Multiwavelength coverage of WLM displaying a $4\frac{1}{2} \times 4\frac{1}{2}$ area. We show the total RC flux density at the native resolution (top left) and again with contours (top center). The RC contours are superposed on ancillary LITTLE THINGS images where possible: $H\alpha$ (middle left); RC_{Nth} obtained by subtracting the expected RC_{Th} based on the $H\alpha$ - RC_{Th} scaling factor of Deeg et al. (1997) from the total RC; *GALEX* FUV (middle right); *Spitzer* $24\ \mu m$ (bottom center); *Spitzer* $70\ \mu m$ (bottom center); FUV+ $24\ \mu m$ -inferred SFRD from Leroy et al. (2012; bottom right). We also show the RC that was isolated by the RC-based masking technique (top right).

Appendix C

Integrated Properties Including Ambiguous Sources

Table 7
Integrated Emission Over the Disk of the LITTLE THINGS Galaxies, Including Ambiguous Sources

Galaxy	Size	P.A.	6 cm RC	H α (10^{-13} erg s $^{-1}$ cm $^{-2}$)	FUV	24 μ m MIR	70 μ m FIR	6 cm RC $_{\text{Nth}}$	B_{eq}
(1)	($'$) (2)	($^{\circ}$) (3)	(mJy) (4)	(5)	(mJy) (6)	(10^{-2} Jy) (7)	(10^{-2} Jy) (8)	(mJy) (9)	(μ G) (10)
CVn I dwA	1.7 \times 1.4	80	>0.29	1.95 \pm 0.03	1.04 \pm 0.11	0.16 \pm 0.06	2.48 \pm 0.04	>0.29	<2
DDO 43	1.8 \times 1.2	6	>0.99	1.28 \pm 0.03	1.07 \pm 0.11	>0.99	<2
DDO 46 ^V	3.8 \times 3.4	84	>1.17	1.09 \pm 0.02	1.76 \pm 0.18	>1.17	<2
DDO 47	4.5 \times 2.3	-79	>0.62	3.01 \pm 0.03	3.02 \pm 0.30	>0.62	<1
DDO 50	7.9 \times 5.7	18	7.32 \pm 0.60	60.49 \pm 0.49	42.13 \pm 4.22	17.89 \pm 0.01	322.60 \pm 0.28	1.56 \pm 0.60	<1
DDO 52	2.2 \times 1.4	4	>1.28	0.29 \pm 0.01	0.61 \pm 0.06	-0.04 \pm 0.02	1.81 \pm 0.05	>1.28	<1
DDO 53	2.7 \times 1.4	81	0.82 \pm 0.13	4.46 \pm 0.04	2.68 \pm 0.27	2.52 \pm 0.02	25.74 \pm 0.03	0.40 \pm 0.13	<1
DDO 63	4.3 \times 4.3	0	1.11 \pm 0.24	4.46 \pm 0.04	5.16 \pm 0.52	1.83 \pm 0.01	3.88 \pm 0.13	0.69 \pm 0.24	<1
DDO 69	4.8 \times 2.7	-64	>0.91	1.71 \pm 0.01	4.87 \pm 0.49	-0.65 \pm 0.01	11.80 \pm 0.07	>0.91	<1
DDO 70	7.4 \times 4.4	88	>1.50	6.38 \pm 0.04	11.68 \pm 1.17	0.58 \pm 0.01	63.30 \pm 0.14	>1.50	<1
DDO 75	6.2 \times 5.2	42	>1.95	40.35 \pm 0.10	29.23 \pm 2.92	0.45 \pm 0.01	75.03 \pm 0.19	>1.95	<1
DDO 87	2.3 \times 1.3	76	>0.70	0.68 \pm 0.01	0.65 \pm 0.07	0.09 \pm 0.02	7.60 \pm 0.03	>0.70	<1
DDO 101	2.1 \times 1.5	-69	>1.79	0.82 \pm 0.01	0.39 \pm 0.04	0.24 \pm 0.02	-0.54 \pm 0.04	>1.79	<1
DDO 126	3.5 \times 1.7	-41	>0.57	3.66 \pm 0.08	2.91 \pm 0.29	0.32 \pm 0.03	14.92 \pm 0.10	>0.57	<1
DDO 133	4.7 \times 3.2	-6	>1.19	4.61 \pm 0.03	4.18 \pm 0.42	0.64 \pm 0.01	33.71 \pm 0.13	>1.19	<2
DDO 154	3.1 \times 1.6	46	>1.73	2.21 \pm 0.02	3.77 \pm 0.38	0.28 \pm 0.03	3.66 \pm 0.04	>1.73	<1
DDO 155	1.9 \times 1.3	51	>0.47	4.85 \pm 0.05	...	0.22 \pm 0.03	16.15 \pm 0.05	>0.47	<2
DDO 165	4.3 \times 2.3	89	>1.19	1.53 \pm 0.01	...	0.03 \pm 0.01	10.69 \pm 0.06	>1.19	<2
DDO 167	1.5 \times 1.0	-24	>0.51	0.80 \pm 0.01	1.05 \pm 0.11	>0.51	<3
DDO 168	4.6 \times 2.9	-25	>0.94	5.95 \pm 0.03	5.57 \pm 0.56	0.67 \pm 0.01	42.28 \pm 0.10	>0.94	<1
DDO 187	2.1 \times 1.7	37	>1.17	0.57 \pm 0.01	1.15 \pm 0.12	-0.02 \pm 0.03	-1.94 \pm 0.09	>1.17	<1
DDO 210	2.6 \times 1.3	-85	>0.88	...	0.80 \pm 0.08	-0.17 \pm 0.02	5.37 \pm 0.04	>0.87	<2
DDO 216	8.0 \times 3.6	-58	>1.29	0.10 \pm 0.01	2.00 \pm 0.20	-0.09 \pm 0.01	9.96 \pm 0.08	>1.29	<1
F564-V03 ^V	1.3 \times 1.0	7	>0.35	...	0.10 \pm 0.01	>0.35	<3
Haro 29	1.7 \times 1.0	85	2.18 \pm 0.11	13.06 \pm 0.45	3.05 \pm 0.33	5.89 \pm 0.05	39.80 \pm 0.05	0.94 \pm 0.12	6
Haro 36 ^V	1.5 \times 1.2	90	0.94 \pm 0.09	2.41 \pm 0.03	2.84 \pm 0.29	0.94 \pm 0.04	23.66 \pm 0.06	0.71 \pm 0.09	5
IC 1613	18.2 \times 14.7	71	5.81 \pm 0.55	56.21 \pm 0.87	93.29 \pm 9.38	6.86 \pm 0.02	417.00 \pm 1.74	0.51 \pm 0.56	5
IC 10 ^V	11.6 \times 9.1	-38	96.38 \pm 0.81	1191.00 \pm 5.73	...	3741.00 \pm 4.83	9547.00 \pm 12.08	-16.78 \pm 0.97	<1
LGS 3	1.9 \times 1.0	-3	>0.57	...	0.08 \pm 0.01	>0.57	<2
M81 dwA ^V	1.5 \times 1.1	86	>1.28	...	0.38 \pm 0.04	>1.28	<2
Mrk 178	2.0 \times 0.9	-51	1.01 \pm 0.14	5.38 \pm 0.09	2.56 \pm 0.27	0.45 \pm 0.03	0.45 \pm 0.01	0.50 \pm 0.14	5
NGC 1569 ^V	2.3 \times 1.3	-59	151.60 \pm 0.31	489.50 \pm 3.03	750.50 \pm 76.03	709.10 \pm 13.47	3596.00 \pm 2.69	72.90 \pm 0.58	17
NGC 2366	9.4 \times 4.0	33	9.82 \pm 0.59	96.45 \pm 1.11	37.34 \pm 3.74	65.64 \pm 0.01	507.90 \pm 0.31	0.66 \pm 0.60	17
NGC 3738	4.8 \times 4.8	0	2.62 \pm 0.48	16.26 \pm 0.17	11.22 \pm 1.13	11.65 \pm 0.03	248.10 \pm 0.41	1.07 \pm 0.48	17
NGC 4163	2.9 \times 1.9	18	>0.69	1.48 \pm 0.02	2.68 \pm 0.27	0.44 \pm 0.03	10.16 \pm 0.11	>0.69	<2
NGC 4214	9.3 \times 8.5	16	27.74 \pm 0.55	178.00 \pm 0.92	79.44 \pm 7.96	199.50 \pm 0.01	2383.00 \pm 1.09	10.83 \pm 0.55	6
Sag DIG ^V	4.3 \times 2.3	88	>2.47	1.28 \pm 0.01	4.55 \pm 0.46	>2.47	6
UGC 8508	2.5 \times 1.4	-60	0.96 \pm 0.13	2.85 \pm 0.04	...	0.40 \pm 0.03	13.04 \pm 0.04	0.69 \pm 0.13	4
VIIZw 403	2.2 \times 1.1	-11	1.50 \pm 0.09	7.44 \pm 0.15	3.66 \pm 0.37	2.05 \pm 16.60	62.33 \pm 1.24	0.80 \pm 0.09	6
WLM	11.6 \times 5.1	-2	>2.51	16.81 \pm 0.06	29.55 \pm 2.96	4.62 \pm 0.01	117.80 \pm 0.18	>2.51	<1

Note. (Column 1) Name of dwarf galaxy. The superscript “V” means that disk properties (columns 2–5) are taken from V-band data; otherwise, properties are taken from the B-band; (Columns 2 and 3) Size (major and minor axes) and position angle (P.A.) of the optical disk (Hunter & Elmegreen 2006); (Column 4) 6 cm (\sim 6 GHz) radio continuum flux density. This and the following values are presented including ambiguous sources; (Column 5) H α flux (units of 10^{-13} erg s $^{-1}$ cm $^{-2}$); (Column 6) GALEX FUV flux density; (Column 7) *Spitzer* 24 μ m MIR flux density; (Column 8) *Spitzer* 70 μ m FIR flux density; (Column 9) 6 cm (\sim 6 GHz) radio continuum nonthermal (synchrotron) flux density. All RC $_{\text{Nth}}$ emission is assumed to be synchrotron and is inferred by subtracting the RC $_{\text{Th}}$ component from the total RC following Deeg et al. (1997). The quantity in parentheses is the amount that was regarded as ambiguous. (Column 10) Equipartition magnetic field strength in the plane of the sky (see Equation (3) in Beck & Krause 2005).

Table 8
Integrated Emission Over the RC Mask of the LITTLE THINGS Galaxies, Including Ambiguous Sources

Galaxy	R.A	Decl.	f_{disk}	6 cm RC	H α	FUV	24 μm MIR	70 μm FIR	6 cm RC _{Nth}	B_{eq}
(1)	hh mm ss.s	dd mm ss.s	(%)	(mJy)	(10^{-13} erg s $^{-1}$ cm $^{-2}$)	(mJy)	(10^{-2} Jy)	(10^{-2} Jy)	(mJy)	(μG)
	(2)	(3)	(4)	(5)	(6)	(7)	(8)	(9)	(10)	(11)
DDO 46	07 41 26.6	+40 06 39	0.2	1.29 \pm 0.02	0.16 \pm 0.01	0.02 \pm 0.01	1.28 \pm 0.02	5
DDO 47	07 41 55.3	+16 48 08	0.8	0.38 \pm 0.02	0.16 \pm 0.02	0.06 \pm 0.01	0.37 \pm 0.02	4
DDO 50	08 19 08.7	+70 43 25	2.3	6.81 \pm 0.09	25.52 \pm 0.42	7.57 \pm 0.77	8.12 \pm 0.06	54.72 \pm 0.04	4.46 \pm 0.10	5
DDO 53	08 34 08.0	+66 10 37	3.7	0.45 \pm 0.03	1.91 \pm 0.04	0.74 \pm 0.08	1.41 \pm 0.08	5.66 \pm 0.01	0.27 \pm 0.03	4
DDO 63	09 40 30.4	+71 11 02	0.5	1.56 \pm 0.02	0.27 \pm 0.01	0.20 \pm 0.02	0.07 \pm 0.17	0.47 \pm 0.01	1.54 \pm 0.02	5
DDO 69	09 59 25.0	+30 44 42	1.8	0.96 \pm 0.04	0.02 \pm 0.01	0.08 \pm 0.01	0.12 \pm 0.11	0.74 \pm 0.01	0.96 \pm 0.04	4
DDO 70	10 00 00.9	+05 19 50	0.3	1.53 \pm 0.03	0.29 \pm 0.02	0.21 \pm 0.03	0.04 \pm 0.19	0.47 \pm 0.01	1.51 \pm 0.03	4
DDO 75	10 10 59.2	-04 41 56	0.4	0.27 \pm 0.04	2.89 \pm 0.06	0.90 \pm 0.10	0.06 \pm 0.19	1.71 \pm 0.01	0.01 \pm 0.04	4
DDO 87	10 49 34.7	+65 31 46	0.2	0.13 \pm 0.01	0.01 \pm 0.01	0.01 \pm 0.01	0.01 \pm 0.45	0.18 \pm 0.01	0.13 \pm 0.01	3
DDO 126	12 27 06.5	+37 08 23	4.2	0.33 \pm 0.04	1.45 \pm 0.07	0.54 \pm 0.06	0.15 \pm 0.15	2.14 \pm 0.02	0.21 \pm 0.04	3
DDO 133	12 32 55.4	+31 32 14	0.3	0.39 \pm 0.02	0.01 \pm 0.01	0.01 \pm 0.01	0.02 \pm 0.21	0.03 \pm 0.01	0.39 \pm 0.02	3
DDO 155	12 58 39.8	+14 13 10	5.2	0.28 \pm 0.04	2.23 \pm 0.04	...	0.15 \pm 0.12	2.42 \pm 0.01	0.08 \pm 0.04	>0
DDO 168	13 14 27.2	+45 55 46	0.9	0.24 \pm 0.03	0.26 \pm 0.01	0.12 \pm 0.01	0.04 \pm 0.09	0.77 \pm 0.01	0.21 \pm 0.03	3
DDO 210	20 46 52.0	-12 50 50	0.6	0.39 \pm 0.02	...	0.00 \pm 0.01	0.03 \pm 0.28	0.10 \pm 0.01	0.01 \pm 0.01	>2
Haro 29	12 26 16.7	+48 29 38	14.2	2.04 \pm 0.04	12.59 \pm 0.45	2.68 \pm 0.29	5.01 \pm 0.13	21.99 \pm 0.02	0.85 \pm 0.06	6
Haro 36	12 46 56.3	+51 36 48	9.2	0.38 \pm 0.03	1.17 \pm 0.03	1.94 \pm 0.21	0.41 \pm 0.13	6.88 \pm 0.02	0.26 \pm 0.03	4
IC 1613	01 04 49.2	+02 07 48	1.0	3.69 \pm 0.06	10.30 \pm 0.43	5.19 \pm 0.71	1.70 \pm 0.19	24.14 \pm 0.15	2.81 \pm 0.07	3
IC 10	00 20 17.5	+59 18 14	22.9	99.33 \pm 0.39	887.90 \pm 5.68	...	1369.00 \pm 10.10	5482.00 \pm 6.68	14.96 \pm 0.66	8
M81 dwA	08 23 57.2	+71 01 51	0.2	0.15 \pm 0.02	...	0.01 \pm 0.01	0.01 \pm 0.01	<2
Mrk 178	11 33 29.0	+49 14 24	3.8	0.46 \pm 0.03	2.33 \pm 0.08	0.97 \pm 0.12	0.16 \pm 0.17	0.16 \pm 0.01	0.25 \pm 0.03	4
NGC 1569	04 30 49.8	+64 50 51	125.5	157.30 \pm 0.35	506.70 \pm 3.03	759.10 \pm 76.88	719.60 \pm 12.02	3808.00 \pm 3.01	75.89 \pm 0.60	17
NGC 2366	07 28 48.8	+69 12 22	2.2	12.05 \pm 0.09	66.98 \pm 1.10	12.65 \pm 1.28	52.07 \pm 0.04	179.70 \pm 0.05	5.72 \pm 0.14	5
NGC 3738	11 35 49.0	+54 31 23	6.2	2.98 \pm 0.12	11.83 \pm 0.17	7.29 \pm 0.75	7.58 \pm 0.13	91.12 \pm 0.10	1.85 \pm 0.12	7
NGC 4163	12 12 09.2	+36 10 13	0.2	0.23 \pm 0.01	0.01 \pm 0.01	0.01 \pm 0.01	0.01 \pm 0.61	0.01 \pm 0.01	0.23 \pm 0.01	4
NGC 4214	12 15 39.2	+36 19 38	2.5	23.16 \pm 0.09	117.40 \pm 0.91	32.67 \pm 3.29	140.50 \pm 0.09	943.30 \pm 0.17	12.12 \pm 0.12	6
Sag DIG	19 30 00.6	-17 40 56	1.2	0.56 \pm 0.09	0.01 \pm 0.01	0.11 \pm 0.01	0.56 \pm 0.09	4
UGC 8508	13 30 44.9	+54 54 29	4.4	0.71 \pm 0.03	0.74 \pm 0.02	...	0.08 \pm 0.13	1.66 \pm 0.01	0.64 \pm 0.03	3
VII Zw 403	11 27 58.2	+78 59 39	19.2	1.29 \pm 0.04	6.49 \pm 0.15	3.21 \pm 0.33	2.10 \pm 37.85	33.77 \pm 0.54	0.68 \pm 0.04	6
WLM	00 01 59.2	-15 27 41	0.1	0.28 \pm 0.02	0.79 \pm 0.05	0.11 \pm 0.01	0.27 \pm 0.23	0.36 \pm 0.01	0.23 \pm 0.02	2

Note. (Column 1) Name of dwarf galaxy; (Columns 2 and 3) Equatorial coordinates (J2000) of center of the galaxy defined by the optical disk; (Column 4) Fraction of the disk (see Table 3) that has significant RC emission; (Column 5) 6 cm (\sim 6 GHz) radio continuum flux density. This and the following values are presented including ambiguous sources; (Column 6) H α flux (units of 10^{-13} erg s $^{-1}$ cm $^{-2}$); (Column 7) *GALEX* FUV flux density; (Column 8) *Spitzer* 24 μm MIR flux density; (Column 9) *Spitzer* 70 μm FIR flux density; (Column 10) 6 cm (\sim 6 GHz) radio continuum nonthermal (synchrotron) flux density. All RC_{Nth} emission is assumed to be synchrotron and is inferred by subtracting the RC_{Th} component from the total RC following Deeg et al. (1997). The quantity in parentheses is the amount that was regarded as ambiguous; (Column 11) Equipartition magnetic field strength in the plane of the sky (see Equation (3) in Beck & Krause 2005).

ORCID iDs

Luke Hindson  <https://orcid.org/0000-0002-8801-8568>
 Ged Kitchener  <https://orcid.org/0000-0001-5052-8725>
 Elias Brinks  <https://orcid.org/0000-0002-7758-9699>
 Deidre Hunter  <https://orcid.org/0000-0002-3322-9798>

References

- Altschuler, D. R., Giovanardi, C., Giovanelli, R., & Haynes, M. P. 1984, *AJ*, **89**, 224
- Appleton, P. N., Fadda, D. T., Marleau, F. R., et al. 2004, *ApJS*, **154**, 147
- Baars, J. W. M., Genzel, R., Pauliny-Toth, I. I. K., & Witzel, A. 1977, *A&A*, **61**, 99
- Banerjee, A., Jog, C. J., Brinks, E., & Bagetakos, I. 2011, *MNRAS*, **415**, 687
- Basu, A., Roychowdhury, S., Heesen, V., et al. 2017, *MNRAS*, **471**, 337
- Beck, R. 2009, *ASTRA*, **5**, 43
- Beck, R., & Krause, M. 2005, *AN*, **326**, 414
- Bell, E. F. 2003, *ApJ*, **586**, 794
- Berry, D. S. 2015, *A&C*, **10**, 22
- Berry, D. S., Reinhold, K., Jenness, T., & Economou, F. 2007, in ASP Conf. Ser. 376, *Astronomical Data Analysis Software and Systems XVI*, ed. R. A. Shaw, F. Hill, & D. J. Bell (San Francisco, CA: ASP), 425
- Bigiel, F., Leroy, A., Walter, F., et al. 2008, *AJ*, **136**, 2846
- Burstein, D., & Heiles, C. 1982, *AJ*, **87**, 1165
- Calzetti, D., Kennicutt, R. C., Engelbracht, C. W., et al. 2007, *ApJ*, **666**, 870
- Calzetti, D., Wu, S.-Y., Hong, S., et al. 2010, *ApJ*, **714**, 1256
- Chomiuk, L., & Wilcots, E. M. 2009, *AJ*, **137**, 3869
- Chyży, K. T., Wezgowiec, M., Beck, R., & Bomans, D. J. 2011, *A&A*, **529**, A94
- Condon, J. J. 1992, *ARA&A*, **30**, 575
- Condon, J. J., Cotton, W. D., & Broderick, J. J. 2002, *AJ*, **124**, 675
- Condon, J. J., Cotton, W. D., Greisen, E. W., et al. 1998, *AJ*, **115**, 1693
- da Silva, R. L., Fumagalli, M., & Krumholz, M. 2012a, *ApJ*, **745**, 145
- da Silva, R. L., Fumagalli, M., & Krumholz, M. 2012, *MNRAS*, **444**, 3275b
- Dale, D. A., Cohen, S. A., Johnson, L. C., et al. 2009, *ApJ*, **703**, 517
- de Jong, T., Klein, U., Wielebinski, R., & Wunderlich, E. 1985, *A&A*, **147**, L6
- Deeg, H.-J., Duric, N., & Brinks, E. 1997, *A&A*, **323**, 323
- Dewdney, P., Turner, W., Braun, R., et al. 2015, SKA Memo Series, SKA-TEL-SKO-0000308: SKA1 System Baseline v2 Description (Macclesfield: Univ. Manchester)
- Dohm-Palmer, R. C., Skillman, E. D., Gallagher, J., et al. 1998, *AJ*, **116**, 1227
- Elmegreen, B. G., & Hunter, D. A. 2015, *ApJ*, **805**, 145
- Engelbracht, C. W., Blaylock, M., Su, K. Y. L., et al. 2007, *PASP*, **119**, 994
- Ficut-Vicas, D. 2016, PhD thesis, Univ. Hertfordshire
- Filipović, M. D., Haynes, R. F., White, G. L., & Jones, P. A. 1998, *A&AS*, **130**, 421
- Filipovic, M. D., Haynes, R. F., White, G. L., Jones, P. A., Klein, U., & Wielebinski, R. 1995, *A&AS*, **111**, 311
- Gallagher, J. S., III, & Hunter, D. A. 1984, *ARA&A*, **22**, 37
- Gil de Paz, A., Boissier, S., Madore, B. F., et al. 2007, *ApJS*, **173**, 185
- Green, D. A. 2014, *BASI*, **42**, 47
- Gregory, P. C., & Condon, J. J. 1991, *ApJS*, **75**, 1011
- Greisen, E. W. 2011, in AIPS Memo Series, 113r (<https://casa.nrao.edu/Release4.1.0/doc/UserMan/UserMansu164.html>)
- Hancock, P. J., Murphy, T., Gaensler, B. M., et al. 2012, *MNRAS*, **422**, 1812
- Heesen, V., Beck, R., Krause, M., & Dettmar, R.-J. 2009, *A&A*, **494**, 563
- Heesen, V., Brinks, E., Krause, M. G. H., et al. 2015, *MNRAS*, **447**, L1
- Heesen, V., Brinks, E., Leroy, A. K., et al. 2014, *AJ*, **147**, 103
- Heesen, V., Dettmar, R.-J., Krause, M., et al. 2016, *MNRAS*, **458**, 323
- Heesen, V., Rau, U., Rupen, M. P., Brinks, E., & Hunter, D. A. 2011, *ApJL*, **739**, L23
- Helou, G., & Bica, M. D. 1985, *ApJ*, **415**, 93
- Helou, G., Soifer, B. T., & Rowan-Robinson, M. 1985, *ApJL*, **298**, L7
- Hindson, L., Johnston-Hollitt, M., Hurley-Walker, N., et al. 2016, *PASA*, **33**, e020
- Hoeppe, G., Brinks, E., Klein, U., et al. 1994, *AJ*, **108**, 446
- Hunter, D. A., & Elmegreen, B. G. 2004, *AJ*, **128**, 2170
- Hunter, D. A., & Elmegreen, B. G. 2006, *ApJS*, **162**, 49
- Hunter, D. A., Ficut-Vicas, D., Ashley, T., et al. 2012, *AJ*, **144**, 134
- Huyh, M. T., Hopkins, A. M., Lenc, E., et al. 2012, *MNRAS*, **426**, 2342
- Israel, F. P., & de Bruyn, A. G. 1988, *A&A*, **198**, 109
- Kennicutt, R. C., Jr., Hao, C.-N., Calzetti, D., et al. 2009, *ApJ*, **703**, 1672
- Kepley, A. A., Mühle, S., Everett, J., et al. 2010, *ApJ*, **712**, 536
- Kepley, A. A., Zweibel, E. G., Wilcots, E. M., Johnson, K. E., & Robishaw, T. 2011, *ApJ*, **736**, 139
- Klein, U. 1986, *A&A*, **168**, 65
- Klein, U., Giovanardi, C., Altschuler, D. R., & Wunderlich, E. 1992, *A&A*, **255**, 49
- Klein, U., Weiland, H., & Brinks, E. 1991, *A&A*, **246**, 323
- Koda, J., Yagi, M., Boissier, S., et al. 2012, *ApJ*, **749**, 20
- Lacki, B. C., Thompson, T. A., & Quataert, E. 2010, *ApJ*, **717**, 1
- Lee, J. C., Gil de Paz, A., Tremonti, C., et al. 2009, *ApJ*, **706**, 599
- Leitherer, C., Schaerer, D., Goldader, J. D., et al. 1999, *ApJ*, **123**, 3
- Leroy, A. K., Bigiel, F., de Blok, W. J. G., et al. 2012, *AJ*, **144**, 3
- Leverenz, H., & Filipović, M. D. 2013, *Ap&SS*, **343**, 301
- Li, Y., Calzetti, D., Kennicutt, R. C., et al. 2010, *ApJ*, **725**, 677
- Lisenfeld, U., & Ferrara, A. 1998, *ApJ*, **496**, 145
- Lisenfeld, U., & Volk, H. J. 2000, *A&A*, **354**, 423
- Lisenfeld, U., Wilding, T. W., & Pooley, G. G. 2004, *MNRAS*, **349**, 1335
- Longair, M. S. 1981, *High Energy Astrophysics* (Cambridge: Cambridge Univ. Press)
- Martin, N. F., Ibata, R. A., Chapman, S. C., Irwin, M., & Lewis, G. F. 2007, *MNRAS*, **380**, 281
- Mateo, M. L. 1998, *ARA&A*, **36**, 435
- McMullin, J. P., Waters, B., Schiebel, D., Young, W., & Golap, K. 2007, in ASP Conf. Ser. 376, *Astronomical Data Analysis Software and Systems XVI*, ed. R. A. Shaw, F. Hill, & D. J. Bell (San Francisco, CA: ASP), 127
- McQuinn, K. B. W., Skillman, E. D., Cannon, J. M., et al. 2010, *ApJ*, **724**, 49
- Murphy, E. J., Condon, J. J., Schinnerer, E., et al. 2011, *ApJ*, **737**, 67
- Nicholls, D. C., Dopita, M. A., Sutherland, R. S., et al. 2014, *ApJ*, **790**, 75
- Niklas, S., & Beck, R. 1997, *A&A*, **320**, 54
- Niklas, S., Klein, U., & Wielebinski, R. 1997, *A&A*, **322**, 19
- Niklas, S., Wielebinski, R., Klein, U., & Brain, J. 1996, *IAU Symposium*, **171**, 424
- Padovani, P. 2011, *MNRAS*, **411**, 1547
- Papadopoulos, P. P. 2010, *ApJ*, **720**, 226
- Perley, R. A., & Butler, B. J. 2013, *ApJS*, **204**, 19
- Perley, R. A., & Butler, B. J. 2017, *ApJS*, **230**, 7
- Price, R., & Duric, N. 1992, *ApJ*, **401**, 81
- Rau, U., & Cornwell, T. J. 2011, *A&A*, **532**, A71
- Rau, U., & Pramesh, A. 2003, NCRA Technical Report, R00202
- Roychowdhury, S., & Chengalur, J. N. 2012, *MNRAS*, **423**, L127
- Scaife, A. M. M., & Heald, G. H. 2012, *MNRAS*, **423**, L30
- Skillman, E. D., Kennicutt, R. C., & Hodge, P. W. 1989, *ApJ*, **347**, 875
- Stil, J. M., & Israel, F. P. 2002, *A&A*, **389**, 29
- Stinson, G. S., Dalcanton, J. J., Quinn, T., Kaufmann, T., & Wadsley, J. 2007, *ApJ*, **667**, 170
- Strauss, M. A., Huchra, J. P., Davis, M., et al. 1992, *ApJS*, **83**, 29
- Tabatabaei, F. S., Schinnerer, E., Krause, M., et al. 2017, *ApJ*, **185**, 185
- Tabatabaei, F. S., Schinnerer, E., Murphy, E. J., et al. 2013, *A&A*, **552**, A19
- Tongue, T. D., & Westpfahl, D. J. 1995, *AJ*, **109**, 2462
- Völk, H. J. 1989, *A&A*, **218**, 67
- Walker, M. G., Mateo, M., Olszewski, E. W., et al. 2007, *ApJL*, **667**, L53
- Weisz, D. R., Skillman, E. D., Cannon, J. M., et al. 2008, *ApJ*, **689**, 160
- Westcott, J., Brinks, E., Hindson, L., Beswick, R., & Heesen, V. 2017, arXiv:1712.00025
- Wynn-Williams, C. G., & Becklin, E. E. 1986, *ApJ*, **308**, 620
- Xu, C. 1990, *ApJL*, **365**, L47
- Yun, M. S., Reddy, N. A., & Condon, J. J. 2001, *ApJ*, **554**, 803
- Zhang, H.-X., Hunter, D. A., Elmegreen, B. G., Gao, Y., & Schuba, A. 2012, *AJ*, **143**, 47